

PIEZOELECTRIC AND MAGNETOELASTIC STRAIN IN
THE TRANSDUCTION AND FREQUENCY CONTROL OF
NANOMECHANICAL RESONATORS

Thesis by

Sotirios K. Masmanidis

In Partial Fulfillment of the Requirements

for the Degree of

Doctor of Philosophy

CALIFORNIA INSTITUTE OF TECHNOLOGY

Pasadena, California

2006

(Defended July 24, 2006)

© 2006

Sotirios K. Masmanidis

All Rights Reserved

ACKNOWLEDGEMENTS

I would like to start by thanking my advisor, Michael Roukes, for giving me the opportunity and resources to work in his lab. I would never have gotten anywhere without the tremendous help of Hong Tang and Jan Honolka, who trained me thoroughly in the arts of nanofabrication and electronic measurement, and whose experiments provided a vital initial foothold into my own research. I also thank Jessica Arlett, Nils Asplund, Blake Axelrod, Igor Bargatin, Philip Feng, Warren Fon, Ben Gudlewski, Inna Kozinsky, Wonhee Lee, Henk Postma and Darron Young for helping me learn my way about the lab and cleanroom. I greatly benefited from daily interactions with my colleagues in the Roukes group and extend my thanks to all of them. My discussions with John Choi over spicy food played an important role in determining the final version of the D-NEMS heterostructure design. Steve Stryker meticulously machined many of the parts used in the experiments. Hong, Ed Myers and Mo Li made important contributions on the GaMnAs resonator project. I am grateful to Rassul Karabalin for his assistance on the D-NEMS experiments and for carrying on the work we started.

I have been fortunate to have collaborated with several brilliant scientists. David Awschalom from UC Santa Barbara kindly provided the GaMnAs epilayers used at the beginning of my graduate studies. I would like to thank Wim Van Roy, Kristiaan De Greve and Geert Vermeulen from IMEC, Leuven, for supplying the GaMnAs/GaAs/AlGaAs heterostructures used in the GaMnAs resonator project. I am also very grateful for their hospitality during a visit to their laboratories in 2005. Many thanks to Iwijn De Vlaminck and Gustaaf Borghs from IMEC for providing a large number of high-quality GaAs heterostructures that spawned the D-NEMS project. I am grateful to Mark Freeman who, while visiting on sabbatical from the University of Alberta, introduced me to the elegance of optical interferometric detection and provided the inspiration for studying GaAs NEMS at room temperature.

While sailing this little maelstrom of research, my family's unconditional support and Lin's smile and encouragement helped keep me afloat.

for

Ioanna

ABSTRACT

Stress and strain play a central role in semiconductors, and are strongly manifested at the nanometer-scale regime. Piezoelectricity and magnetostriction produce internal strains that are anisotropic and addressable via a remote electric or magnetic field. These properties could greatly benefit the nascent field of nanoelectromechanical systems (NEMS), which promises to impact a variety of sensor and actuator applications. The piezoelectric semiconductor GaAs is used as a platform for probing novel implementations of resonant nanomechanical actuation and frequency control. GaAs/AlGaAs heterostructures can be grown epitaxially, are easily amenable to suspended nanostructure fabrication, have a modest piezoelectric coefficient roughly twice that of quartz, and if appropriately doped with manganese, can form dilute magnetic compounds. In ordinary piezoelectric transducers there is a clear distinction between the metal electrodes and piezoelectric insulator. But this distinction is blurred in semiconductors. An integrated piezoelectric actuation mechanism is demonstrated in a series of suspended anisotype GaAs junctions, notably pin diodes. A dc bias was found to alter the resonance amplitude and frequency in such devices. The results are in good agreement with a model of strain based actuation encompassing the diode's voltage-dependent carrier depletion width and impedance. A bandstructure engineering approach is employed to control the actuation efficiency by appropriately designing the doping level and thickness of the GaAs structure. Actuation and frequency are also sensitively dependent on the device's crystallographic orientation. This combined tuning behavior represents a novel type of depletion-mediated electromechanical coupling in piezoelectric semiconductor nanostructures. All devices are actuated piezoelectrically, whereas three techniques are demonstrated for sensing: optical interferometry, piezoresistance and piezoelectricity. Finally, a nanoelectromechanical GaMnAs resonator is used to obtain the first measurement of magnetostriction in a dilute magnetic semiconductor. Resonance frequency shifts induced by field-dependent magnetoelastic stress are

used to simultaneously map the magnetostriction and magnetic anisotropy constants over a wide range of temperatures. Owing to the central role of carriers in controlling ferromagnetic interactions in this material, the results appear to provide insight into a unique form of magnetoelastic behavior mediated by holes.

TABLE OF CONTENTS

Chapter 1: Overview of gallium arsenide nanomechanical systems	1
1.1 Introduction and motivation	1
1.2 Gallium arsenide properties	2
1.3 Suspended GaAs nanostructure process flow	5
1.4 Processing considerations and challenges	7
References.....	10
Chapter 2: D-NEMS: Depletion-mediated piezoelectric actuation	11
2.1 Introduction to piezoelectric semiconductors and D-NEMS	11
2.2 Basic concepts in piezoelectricity	12
2.3 Multilayer piezoelectric actuation scheme	14
2.4 Impact of carrier depletion on piezoelectric diode actuation	15
2.5 D-NEMS device fabrication.....	18
2.6 Driving signal attenuation and diode equivalent circuit.....	21
2.7 Mechanical detection with optical interferometry.....	23
2.8 Experimental data	24
2.9 Modulation doping from the <i>p</i> -AlGaAs layer	27
2.10 D-NEMS actuation under a large forward bias	29
2.11 Piezoelectric actuation of a nanomechanical <i>npn</i> junction	30
2.12 D-NEMS frequency-doubled actuation	31
References.....	33
Chapter 3: Piezoelectric frequency control of D-NEMS resonators	35
3.1 Piezoelectric frequency tuning	35
3.2 Electrostrictive frequency tuning	37
3.3 Electrostatic frequency tuning.....	38
3.4 Experimental data	39
3.5 Photoacoustic frequency tuning and voltage annealing effects	43
3.6 Uniformity of device quality factor and frequency	46
References.....	49
Chapter 4: Noise processes in piezoelectric semiconductor NEMS	50
4.1 Thermomechanical noise spectrum.....	50
4.2 Photodetector noise	52
4.3 Laser diode shot noise	53
4.4 Electromechanical noise.....	54
4.5 Frequency stability of D-NEMS	55
4.6 Summary of noise processes	57
References.....	58

Chapter 5: Novel D-NEMS architectures	59
5.1 Introduction.....	59
5.2 Parametric amplification	60
5.3 Balanced charge detection.....	62
5.4 Prospects for measuring quantized piezoelectric strain.....	64
5.5 Nanomechanical mode-shape engineering	65
5.6 Alternative piezoelectric materials for NEMS	68
5.7 Ultimate scaling limits of semiconductors NEMS	69
References.....	73
Chapter 6: All-electrical transduction with D-NEMS	75
6.1 Motivation for all-electrical electromechanical transduction.....	75
6.2 Piezoresistive detection	76
6.3 Piezoelectric detection – theory	79
6.4 Piezoelectric detection – experiment	81
6.5 DC bias-dependent transduction efficiency.....	84
6.6 Prospects for improving piezoelectric detection.....	85
References.....	88
Chapter 7: Nanomechanical measurement of magnetostriction and magnetic anisotropy in GaMnAs	89
7.1 Background and motivation for GaMnAs experiment.....	89
7.2 Magnetoelastic NEMS resonator behavior in a magnetic field	93
7.3 Frequency and quality factor at high magnetic field	98
7.4 Temperature dependence of magnetoelastic effects.....	99
7.5 Measurement of magnetostriction and magnetic anisotropy.....	100
7.6 Discussion of results.....	105
7.7 Inverse magnetoelastic contribution to magnetic anisotropy	108
7.8 Outlook on the role of magnetostriction in GaMnAs.....	109
References.....	110
Chapter 8: The Big Picture	113
8.1 Summary and experimental conclusions	113
8.2 Outlook and challenges	116
References.....	122
Appendix: List of major measurement equipment	124

LIST OF FIGURES AND TABLES

- Fig. 1.1** (a) Normalized resonance frequency, (b) mass sensitivity, and (c) force responsivity of some common materials.
- Fig. 1.2** Basic suspended GaAs structure process flow.
- Fig. 1.3** Example of acceptable and unacceptable samples.
- Fig. 2.1** Trimorph piezoelectric actuation scheme for a cantilever.
- Fig. 2.2** (a) Potential and (b) electric field distribution in a model GaAs *pin* diode.
- Fig. 2.3** (a) SEM image of 4 μm long *pin* diode-embedded cantilever, with crystallographic axes. (b) Direction of transverse piezoelectric strains due to a positive electric field.
- Fig. 2.4** Model electric field distribution in *pin* diode, illustrating the tunable actuation concept.
- Fig. 2.5** (a) Equivalent circuit of mechanical *pin* diode resonator. (b) Measured I(V) curves and (c) the calculated driving efficiency of a 10 MHz signal.
- Fig. 2.6** (a) Illustration of principles of optical interferometric displacement detection. (b) Calculated intensity of coherent light with $\lambda=904$ nm reflecting off two surfaces as a function of gap spacing.
- Fig. 2.7** (a) Image of experimental setup. (b) Schematic of setup used to actuate and bias the NEMS resonators with a superposition of ac and dc signals.
- Fig. 2.8** (a) Resonant response of the $4 \times 0.8 \times 0.2 \mu\text{m}^3$ cantilever shown in Fig. 2.3a, under different ac driving voltages and fixed dc bias. (b) Resonant response of the same device under fixed ac and varying dc bias.
- Fig. 2.9** Measured resonance amplitude vs. dc bias of the three *pin* diodes under fixed ac drive.
- Fig. 2.10** Modulation doping effects: normalized resonance amplitude vs. dc voltage for the three *pin* diodes.
- Fig. 2.11** Normalized resonance amplitude vs. dc voltage in the large forward bias regime.
- Fig. 2.12** (a) Resonant response of an *npn* GaAs cantilever under different ac driving voltages and fixed dc bias. (b) Resonant response of the same device under fixed ac and varying dc bias. (c) Resonance amplitude vs. dc bias, with an ac drive of $10 \text{ mV}_{\text{RMS}}$.
- Fig. 2.13** Frequency-doubled actuation.
- Fig. 3.1** (a) Predicted resonance frequency shift vs. axial force of a GaAs beam calculated from the exact and linearized expression. (b) Calculated resonance frequency shift in a beam

with [110] alignment due to piezoelectric and electrostrictive effects in a *pin* diode with a 50 nm wide depletion layer.

- Fig. 3.2** (a) SEM image of 4 μm long doubly clamped beam used to investigate piezoelectric frequency tuning phenomena, and (b) coordinate axes. (c) Resonant response of the beam under different driving voltage and fixed dc bias. (d) Resonant response of the beam under different dc voltage and fixed ac drive.
- Fig. 3.3** Resonance frequency of doubly clamped beams *vs.* dc bias, measured in a phase-locked loop.
- Fig. 3.4** (a) Piezoelectrically induced frequency jumps of a $4 \times 0.8 \times 0.2 \mu\text{m}^3$ doubly clamped beam measured in a phase-locked loop. (b) Operation of phase-locked loop in the voltage-controlled mode.
- Fig. 3.5** Frequency shift *vs.* laser power for a cantilever and beam made from diode *pin-1*.
- Fig. 3.6** PLL scans of frequency shift *vs.* time under different applied dc voltages and laser intensity.
- Fig. 3.7** Quality factor *vs.* resonance frequency of identically fabricated 3 μm long cantilevers (a, c) and 5 μm long beams (b, d) from diode *pin-1*.
- Fig. 4.1** Thermomechanical noise spectrum of a 4 μm long cantilever fabricated from diode *pin-1* in the vicinity of its first mechanical resonance mode.
- Fig. 4.2** Wide band scan of the photodetector noise spectrum under different levels of IR laser illumination.
- Fig. 4.3** Phase-locked loop scans demonstrating frequency instability.
- Fig. 5.1** (a) SEM image of guitar NEMS array fabricated from diode *pin-1*. The shortest and longest devices are used to demonstrate parametric nanomechanical amplification in vacuum (b) and air (c), respectively.
- Fig. 5.2** (a) Prototype device for demonstrating balanced charge detection using orthogonal doubly clamped beams. (b) Real component and (c) magnitude of optical response of the two 7 μm long beams under different applied dc bias voltages.
- Fig. 5.3** Demonstration of mode suppression in a cross-beam resonator fabricated from diode *pin-1*.
- Fig. 5.4** (a) Schematic illustration of the nanomechanical logic gate concept employing the piezoelectric anisotropy property of GaAs and other crystals. (b) Expected truth table for such a device.

- Fig. 5.5** (a) Band energy diagram of a 50 nm thick GaAs *pn* junction with 10^{19} cm^{-3} doping on each side. (b) Schematic of *pn* junction cross-section depicting surface depletion (pale green) and junction depletion (gray).
- Fig. 5.6** Minimum thickness, given by w_{pn} of *pn* junctions fabricated from different materials under zero applied bias.
- Fig. 6.1** (a) SEM image of beam designed for piezoelectric actuation (right side)/piezoresistive detection (left side; legs). (b) Measured piezoresistive signal of device using the heterodyne downconversion (a.k.a. downmixing) scheme.
- Fig. 6.2** Setup for piezoresistive sensing of D-NEMS using the frequency downconversion technique.
- Fig. 6.3** Piezoresistive response of the device in Fig. 6.1a in the parametric amplified mode.
- Fig. 6.4** Equivalent circuit of D-NEMS with source of strain-induced current.
- Fig. 6.5** Balanced bridge setup for measuring piezoelectric response of D-NEMS.
- Fig. 6.6** Piezoelectric response of the cantilever on one arm of the balanced bridge under different driving amplitudes.
- Fig. 6.7** Mechanical resonance amplitude *vs.* dc bias voltage using piezoelectric (dots) and optical (line) detection.
- Fig. 6.8** SEM image of device footprint with close-up of a 4 μm cantilever used in the measurements.
- Fig. 6.9** Optically measured response of the same cantilever used to record data in Figs. 6.6 & 6.7.
- Fig. 7.1** The “dipper” used to conduct low-temperature experiments on (Ga,Mn)As.
- Fig. 7.2** Resistance *vs.* temperature of the suspended $\text{Ga}_{0.948}\text{Mn}_{0.052}\text{As}$ device shown in Fig. 7.3a.
- Fig. 7.3** (a) Image of the 6 μm long doubly clamped beam device. The coordinates and relevant magnetization and field angles are shown for reference in (b). (c) plots the piezoresistive downmixed response to different driving voltages, while (d) displays the resonance shifts in the presence of a 10 kOe magnetic field oriented along the three principal directions.
- Fig. 7.4** (a) Resonance frequency shifts *vs.* magnetic field along the three principal directions, measured by operating the device in a phase-locked loop. (b) Frequency shift for a field along x or [110] in the low field regime. The jumps occur near the coercive field of the material, suggesting they correspond to domain wall transitions.

- Fig. 7.5** (a) Resonance frequency shifts *vs.* magnetic field along the z axis, measured by operating the device in a phase-locked loop. (b) Quality factor *vs.* magnetic field, measured every 0.1 T. All measurements are at 4.2 K.
- Fig. 7.6** Frequency shifts *vs.* magnetic field along the y direction, *i.e.*, [-110].
- Fig. 7.7** Polar plots of frequency shifts *vs.* in-plane magnetic field angle, at a fixed field magnitude of 5 kOe.
- Fig. 7.8** Structure used to model the effect of magnetoelastic stress on the resonance frequency.
- Fig. 7.9** Plots illustrating role of magnetic anisotropy.
- Fig. 7.10** Magnetostriction (a) and magnetic anisotropy field (b) parameters of $\text{Ga}_{0.948}\text{Mn}_{0.052}\text{As}$ *vs.* temperature.
- Fig. 8.1** Some of the suspended nanomechanical GaAs structures used in the depletion-mediated NEMS (D-NEMS) experiments. Scale bars are (from top left going clockwise): 2, 2, 2, 5, 2, 10 μm , respectively.
- Fig. 8.2** SEM image of GaMnAs suspended beam used to obtain the first measurements of magnetostriction in a dilute magnetic semiconductor.
- Fig. 8.3** Nanomechanical arrays fabricated from piezoelectric D-NEMS material.
- Table 1.1** Some important chemical, thermal, electrical and elastic material parameters of GaAs.
- Table 2.1** Doping profile of the three GaAs *pin* diodes.
- Table 5.1** Piezoelectric constants of some semiconductors.
- Table 7.1** Magnetostriction constants of some common magnetoelastic materials, at room temp.

NOMENCLATURE

NEMS	nanoelectromechanical systems
D-NEMS	depletion-mediated NEMS
frequency	$\omega/2\pi$ unless stated otherwise
I	moment of inertia
ρ	mass density
m	mass
Y	Young's modulus
c_{11}, c_{12}, c_{44}	elastic constants
e_{14}, e_{11}, e_{13}	piezoelectric constants (C/m^2)
d_{14}, d_{11}, d_{13}	piezoelectric constants (m/V)
e_{ij} (j=x,y,z)	Cartesian strain
σ_{ij} (j=x,y,z)	Cartesian stress
E_j (j=x,y,z)	electric field
H_j (j=x,y,z)	magnetic field
E_g	band gap energy
V	voltage
V_{bi}	built-in voltage
ϵ	dielectric constant
K	magnetic anisotropy energy density
H_K	magnetic anisotropy field
λ	first order magnetostriction constant (strain)
h_3	second order magnetostriction constant (strain)
α	first order thermal expansion coefficient

Chapter 1

Overview of gallium arsenide nanomechanical systems

1.1 Introduction and motivation

Nanotechnology promises to radically transform virtually every sector of industry and impact society in countless ways. Momentarily tuning out the hype, it is too early to tell which approaches will eventually pan out, but ideas merging quantum mechanics, genetic manipulations, even single-atom manipulations are all fair game. Richard Feynman's speech¹ is as visionary today as it was 47 years ago, but the "room at the bottom" no longer seems so elusive, with scientists around the world calling it their playground.

The nascent class of devices known as *nanoelectromechanical systems* (NEMS) could provide sensors and actuators that are vastly superior in terms of sensitivity², power handling, density³ and cost than their bulkier macro- and micro-scale counterparts. In the long term these systems may lead to a paradigm shift in biomolecular studies, medical diagnostics and radio frequency electronics⁴. However, a number of obstacles must be overcome before these goals are met, including transduction, interconnecting the nano and macro components, and ensuring the devices are reliable and scalable to large volumes. No commercially available NEMS products exist today, although MEMS are employed in a variety of applications⁵. A primary setback (besides cost) is that despite significant progress, efficient actuation and detection of nanoscale mechanical devices remains a daunting challenge^{6,7}. This thesis provides a solution to the problem of actuation with a focus on internal strain mechanisms that rely on intrinsic material properties, namely piezoelectricity and magnetostriction. Piezoelectricity is shown to drive

resonant devices in a highly efficient manner – just a few electronic charges produce a measurable response. Furthermore, piezoelectric and magnetostrictive (a.k.a. magnetoelastic) effects provide an excellent way of tuning mechanical properties such as resonance frequency. The strains typically involved (.01 to 100 parts per million) are strongly manifested in submicron thick suspended structures. At such scales, the resulting fractional change in mechanical resonance frequency can readily exceed the strain by two or more orders of magnitude.

The remainder of this chapter provides some introductory notes on the role of GaAs in NEMS, and a brief overview of the generic nanofabrication process flow. Chapters 2 – 6 discuss various aspects of tunable, piezoelectrically actuated GaAs resonators. The three tunable properties explored here are transduction efficiency, resonance frequency and piezoelectric crystalline anisotropy. Finally, Chapter 7 reviews my work on magnetoelastic stress effects used to tune the resonance frequency of a GaMnAs resonator and extract some new information about this material. I give my concluding remarks and outlook in Chapter 8.

1.2 Gallium arsenide properties

Table 1.1 lists some important chemical, mechanical and electronic properties of GaAs. I will omit a discussion of GaMnAs in this section but describe it briefly at the beginning of Chapter 7. The primary commercial application of GaAs is in radio frequency electronics, where its higher band gap and higher electron mobility provide better performance and power handling than silicon. GaAs/AlGaAs heterostructures are also used in infrared laser diodes. Despite these applications, the niche occupied by GaAs is a tiny fraction of the solid state device market, which is dominated by silicon. Therefore the most interesting GaAs structures may only ever exist in a laboratory. NEMS is one of many research fields using this material. The selling points are that GaAs is piezoelectric, piezoresistive, can be monolithically integrated with other electronics, has low built-in stress and high mobility. The disadvantages are that it is expensive, toxic,

mechanically soft and dense relative to silicon and other materials. The low Young's modulus and high density implies lower operating resonance frequencies and more mass on the device, which will diminish its ability to detect mass loading events. The minimum mass sensitivity of a resonator depends on the ratio $\delta m \propto \rho^{3/2} / Y^{1/2}$. Figure 1.1 plots this value for some popular materials; clearly if all other device parameters are equal, then GaAs is not among the best materials to use as a mass detector. However, in calculating this ratio it is important to realize that many NEMS devices require metal films in order to operate⁷.

crystal structure	zinc blende	direct/indirect band gap	direct
lattice constant	5.653 Å	band gap @ 300 K	1.424 eV
n-n distance	2.448 Å	dielectric constant	13.1
density	5317 kg/m ³	refractive index @ 1.4 eV	3.6
molecular density	2.214x10 ²² cm ⁻³	intrinsic carrier density	1.8x10 ⁶ cm ⁻³
melting point	1238 °C	breakdown field	~400 kV/cm
thermal conductivity	55 W/m-K	electron mobility	8500 cm ² /V-s
specific heat	327 J/kg-K	hole mobility	400 cm ² /V-s

preferred cleavage planes	{110}	ionicity	0.32
Young's modulus [110]	101 GPa	pressure coefficient of E _g	2x10 ⁻²³ cm ⁻³
c ₁₁	119 GPa	piezoelectric constant e ₁₄	-0.16 C/m ²
c ₁₂	53.8 GPa	piezoelectric constant d ₁₄	-2.69 pm/V
c ₄₄	59.5 GPa	piezoresistive gauge factor	~11
Poisson's ratio	0.31	linear thermal expansion	6 ppm/K

Table 1.1 Some important chemical, thermal, electrical and elastic material parameters of GaAs [Refs: Blakemore (8) and Adachi (9)]. All values are at room temperature.

Metals increase the effective density and reduce stiffness, leading to a significant deterioration of mass sensitivity. On the other hand, as I will show, GaAs devices have no need for any metal directly on the nanomechanical element, so their sensitivity is actually comparable to metal-semiconductor NEMS devices. This suggests that the game is not over for GaAs NEMS as mass detectors. There are also other applications in which this material could serve an important role. For instance, in force or stress sensing, mechanically compliant materials offer a distinct advantage over stiff materials. Another advantage is that electronic components such as transistors, diodes, capacitors and lasers can be monolithically integrated with nanomechanical devices, which cannot easily be achieved with other material systems such as silicon-on-oxide. Finally, it remains the most easily accessible piezoelectric semiconductor. Thus I believe that until molecular beam epitaxy (MBE) technology for other materials like aluminum nitride can catch up, GaAs will be a viable alternative to silicon for NEMS applications.

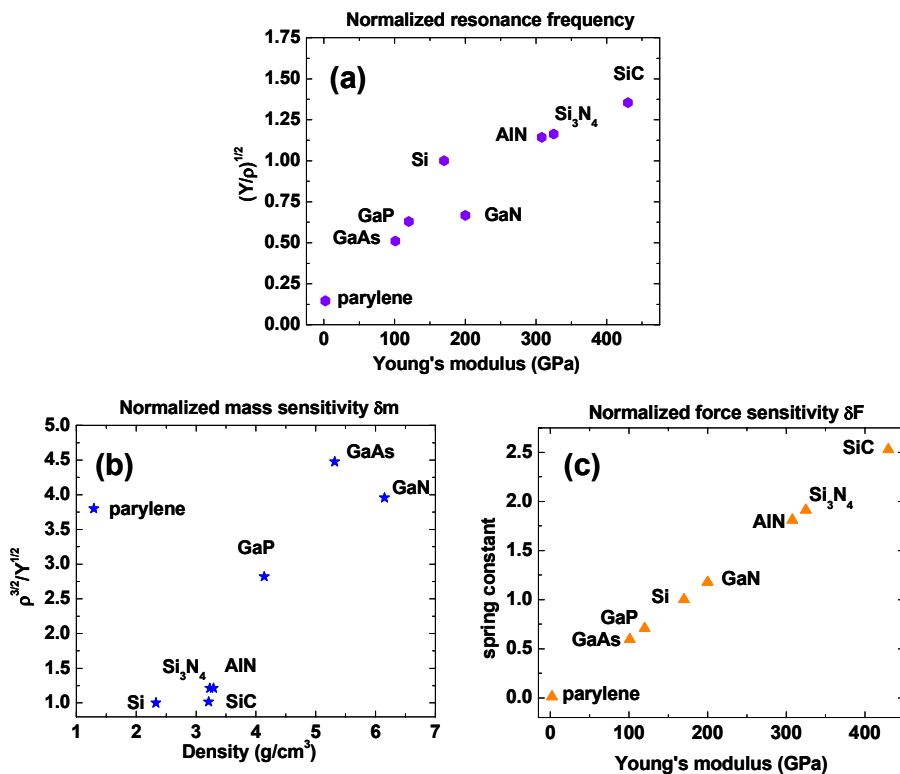


Figure 1.1 (a) Normalized resonance frequency, (b) mass sensitivity, and (c) force responsivity of some common materials. For clarity, the parameters are normalized to those of silicon. All devices are assumed to have the same dimensions and frequency resolution δf .

1.3 Suspended GaAs nanostructure process flow

The process flow is the nanotechie's coveted recipe for making his or her little devices. Fabrication is widely perceived as the least glamorous part of nanotechnology and I can understand why. Nothing frustrated me more during research than the barrage of problems encountered in the cleanroom. But I also remember the joy I felt when I viewed my first sample under high magnification in a scanning electron microscope.

All our material was grown by our collaborators at IMEC, using MBE to deposit selectively doped layers with atomic scale precision. The doping was always on the high side – between 10^{18} and 10^{21} impurities per cm^3 . We can therefore assume that all impurities remain ionized in the experimental range of temperatures, 4.2 to 300 K. The layers specified as “intrinsic” actually have an unintentional background p-type doping level of $\sim 10^{15} \text{ cm}^{-3}$ due to acceptor impurities in the MBE evaporation chamber. This resulted in a finite resistivity of $\sim 450 \text{ } \Omega \cdot \text{cm}$ at room temperature, which was still about $10^5 - 10^6$ times higher than the resistivity of the intentionally doped layers.

The substrate always consisted of a 500 μm (001) GaAs wafer, buffer layers to improve smoothness and a sheet of $\text{Al}_{0.8}\text{Ga}_{0.2}\text{As}$, which served as a sacrificial layer in the suspended structure process. The epitaxial deposition of material needed to fabricate all-semiconductor NEMS devices is only possible with a limited number of compound semiconductors, and GaAs/AlGaAs growth technology is the best within this category. The benefits of this approach are that doping, lattice strain and thickness can be tuned to precise specifications. Therefore some nanotechnology can be built into the vertical (z) direction of the structure before any of the elaborate nanofabrication processes are even begun. Fabrication miniaturizes the x and y dimensions, but never with the fidelity of MBE. It therefore makes sense to take advantage of the vertical direction.

The generic process flow, illustrated in Figure 1.2, used to make suspended GaAs structures consists of four main steps: (i) electrode deposition, (ii) device mask deposition, (iii) anisotropic etch, and (iv) wet etch. Large electrode pads with dimensions ranging from 150x150 to 300x300 μm^2 were defined lithographically in a resist layer. This was followed by evaporation of Ohmic contacts consisting of Ti/Au/Ti with thickness of 20/50/70 nm. The bottom Ti helped with adhesion and the top Ti layer provided a protective mask for gold, which is readily removed by ion milling. Next a mask of the device was defined using standard electron-beam lithography techniques. About 70 nm of Ti filled the mask impression. We then used a 200 eV to 750 eV argon ion beam source to anisotropically remove the unprotected material vertically down to the depth of the sacrificial layer. While using the 750 eV recipe we found evidence for ion-induced damage in the form of increased layer resistance. This convinced us to switch to 200 eV, after which damage effects were ameliorated. We also reduced the beam flux and etched in spans of 3 or 4 minutes to avoid overheating the sample. The nominal etch rate with the low energy beam was measured by atomic force microscopy at 14 ± 1 nm/min. The optimal solution would be to use an even less energetic process, such as reactive ion or inductively coupled plasma etching, but at the time of writing these tools were not readily available to our group. The final step in the fabrication process involves removal of the sacrificial layer with hydrofluoric acid. HF has excellent etch selectivity to $\text{Al}_{0.8}\text{Ga}_{0.2}\text{As}$ and Ti over GaAs, thereby quickly removing the sacrificial and masking layers without damaging the device.

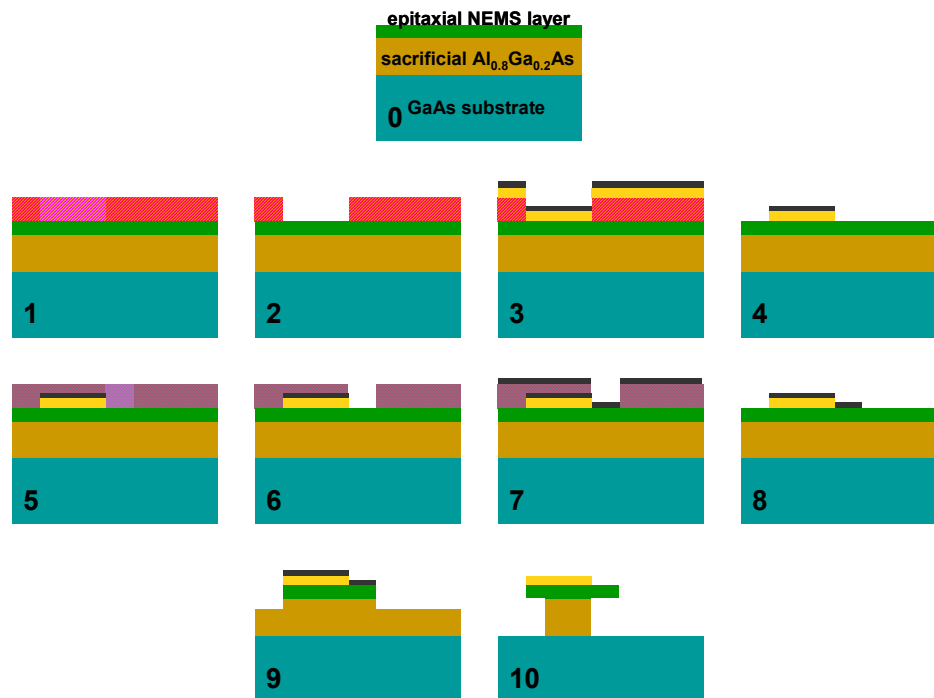


Figure 1.2 Basic suspended GaAs nanostructure process flow. The thickness of the top two layers is exaggerated for clarity. The steps are: (1) photoresist+photolithography, (2) resist develop, (3) metal electrode deposition, (4) lift-off, (5) PMMA+e-beam lithography, (6) resist develop, (7) Ti mask deposition, (8) lift-off, (9) Ar ion beam etch, (10) HF undercut. The actual process flow usually involves either two metal electrode depositions and/or two Ar ion beam etch steps.

1.4 Processing considerations and challenges

Several challenges were encountered during processing. Sample cleanliness was one concern, but atmospheric contamination from dust, hair, *etc.* did not pose a big problem. Most of the contaminants were GaAs dust and chemical by-products of the fabrication process. GaAs dust mainly arose during wafer cleaving and could be reduced by ultrasonic cleaning or coating the wafer with a resist layer that captured the stray particles and could be dissolved after cutting. I also found it invaluable to handle the chips with flat graphite tweezers, which greatly reduces wafer cracking or chipping. Chemical by-products appeared in the final step after the device was

suspended, precluding the use of ultrasonic cleaning as that would break the suspended structures. With some trial and error I found that a very brief dip in a dilute alkaline solution (*e.g.*, 0.5 s in 1% NaOH) removed the majority of contaminants; however, a prolonged exposure to this solution resulted in etching of GaAs, so a trade-off had to be established between picture-perfect devices and amount of damage. I chose to sacrifice perfect cleanliness in favor of no damage. While I do not show images of all the devices used in our experiments, we excluded samples that were covered with a lot of debris that were deemed to significantly impact mechanical or electrical properties. In practice this was not a big concern. With the exception of the GaMnAs experiment, which was only performed once thoroughly, all our devices (even ones with debris) exhibited reproducible behavior. Figure 1.3 shows examples of devices that would be accepted or excluded based on our selection criteria.

Stiction or device collapse is another common problem with NEMS, which often necessitates the use of critical point drying methods. I found that my 200 nm thick doubly clamped devices *never* collapse as long as they are less than ~ 12 μm long. This still leaves ample parameter space to play with, considering all the devices presented here are between 3 and 8 μm long. Moreover I found no improvement after using the critical point dryer. It was sufficient to dry devices with nitrogen directly after rinsing them with methanol. It was challenging to fabricate devices with effective lengths smaller than ~ 2 μm . The reason is that the sacrificial AlGaAs layer is etched nearly isotropically by HF, resulting in ledges that are comparable to the AlGaAs thickness. The ledges increase the effective length of the devices by 0.5 to 1 μm and correspondingly reduce the device's resonance frequency. In next-generation projects with GaAs, it may be important to curb this problem by growing a thinner AlGaAs layer or discovering a more anisotropic etching method.

Determining the device orientation in the (001) plane was important for our experiments. GaAs and its ferromagnetic cousin GaMnAs both possess anisotropic properties along the preferred cleavage directions [110] and [1-10]. In particular, the piezoelectric effect and

magnetic free energy – which we use extensively – are anisotropic. Other properties such as Young’s modulus and the propensity for cleavage are isotropic along these directions. Thus while alignment errors of a few degrees did not greatly concern us, an uncertainty of 90 degrees could lead to an incorrect understanding of our system. There are two simple ways of distinguishing the [110] and [1-10] directions. The easiest is to rely on the major and minor grooves on the wafers, which are cut along prescribed directions. However, it is easy to forget or lose track of orientation after a wafer has been cut. The second way is to use the chemical etch test developed by Shaw¹⁰. The orientation of all our devices has been determined in one or both of these manners.

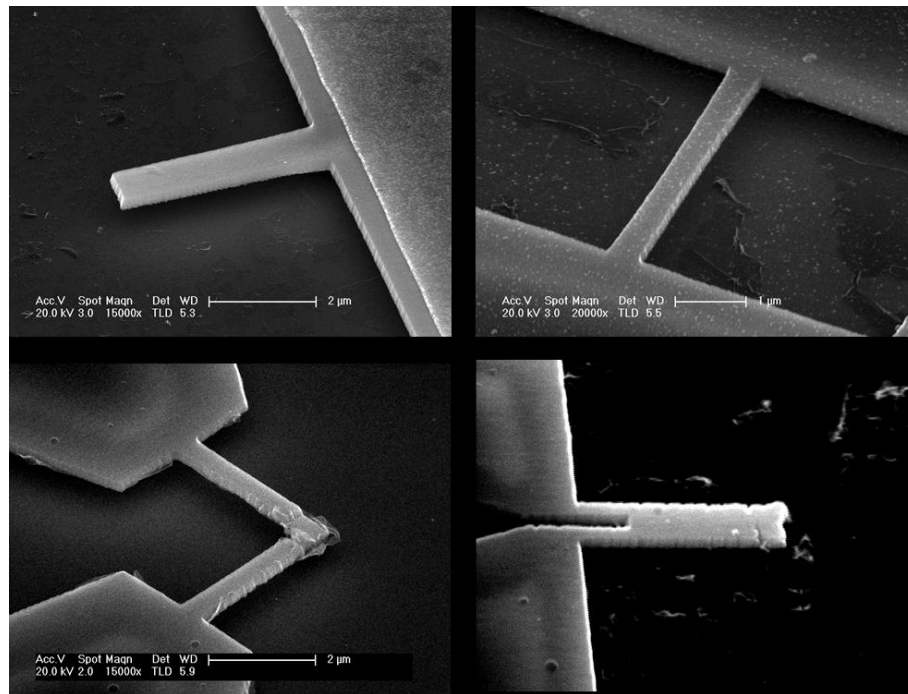


Figure 1.3 Example of acceptable and unacceptable samples. Top left: acceptable device with virtually no debris and excellent side-wall resolution. Top right: acceptable device despite small amount of fine debris. Bottom left: unacceptable device because of large debris at tip. Bottom right: unacceptable device because of poor line resolution that occurred during e-beam lithography.

References

1. R. P. Feynman, Plenty of room at the bottom (1959)
transcript of speech available at <http://www.its.caltech.edu/~feynman/plenty.html>
2. K. L. Ekinici, X. M. H. Huang & M. L. Roukes, Ultrasensitive nanoelectromechanical mass detection, *Appl. Phys. Lett.* **84**, 4469 (2004)
3. P. Vettiger *et al.*, The millipede—more than one thousand tips for future AFM data storage, *IBM J. Res. Develop.* **44**, 323 (2000)
4. X. M. H. Huang, X. L. Feng, C. A. Zorman, M. Mehregany & M. L. Roukes, VHF, UHF and microwave frequency nanomechanical resonators, *New J. Phys.* **7**, 247 (2005)
5. D. J. Nagul & M. E. Zaghoul, MEMS: Micro technology, mega impact, *IEEE Circuits & Devices*, **14** (2001)
6. M. L. Roukes, Nanoelectromechanical systems, *Technical digest of the 2000 solid-state sensor and actuator workshop Hilton Head Island SC*
7. K. L. Ekinici & M. L. Roukes, Nanoelectromechanical systems, *Rev. Sci. Instr.* **76**, 061101 (2005)
8. J. S. Blakemore, Semiconducting and other major properties of gallium arsenide, *J. Appl. Phys.* **53**, 123 (1982)
9. S. Adachi, GaAs, AlAs, and $\text{Al}_x\text{Ga}_{1-x}\text{As}$: material parameters for use in research and device applications, *J. Appl. Phys.* **58**, 1 (1985)
10. D. W. Shaw, Localized GaAs etching with acidic hydrogen-peroxide solutions, *J. Electrochem. Soc.* **128**, 874 (1981)

Chapter 2

D-NEMS: Depletion-mediated piezoelectric actuation

2.1 Introduction to piezoelectric semiconductors and D-NEMS

Since its initial discovery by the Curie brothers¹ in the 1880's, piezoelectricity – the polarization generated by an applied mechanical stress in certain materials and conversely, the strain produced by an applied electric field – has been extensively employed in electromechanical transducers, from crystal oscillators in sonar and wrist watches, to biosensors^{2,3}. Recently, it has attracted interest in the micro- and nanoelectromechanical systems (MEMS and NEMS) communities as a promising means of transducing small scale, radio-frequency (RF) devices^{4,5}. Only certain compound semiconductors such as GaAs possess both piezoelectric and piezoresistive properties, and can be monolithically integrated with other electronic components, such as amplifiers⁶, single-electron transistors^{7,8} and laser diodes^{9,10}, making them attractive candidates for device applications. Another unique feature of these compounds is the electromechanical coupling between their electronic bandstructure and piezoelectric strain distribution¹¹. The coupling arises from the fact that piezoelectric strain concentrates in regions most devoid of carrier charges, where strong electric fields are built up. Carriers can be depleted either passively by suitably doping a semiconductor junction, or actively with an applied voltage. As nanostructures approach depletion width dimensions, it is increasingly important to characterize the interplay between piezoelectric and electronic phenomena and, as we demonstrate here, harness it to obtain functionally useful mechanical behavior. We report on a bandstructure engineering approach to controlling the amplitude of resonantly excited, free-standing GaAs *pin* diodes.

This project was motivated by the need for an integrated NEMS actuation scheme. In the course of exploring suspended GaAs diodes as part of an unsuccessful effort to integrate lasers on cantilevers, we discovered that these devices can be efficiently excited with an ac voltage across the junction. The origin of this actuation is piezoelectric strain. The discovery that the depletion region in diodes, and later transistors, can be used for nanomechanical actuation and a host of other interesting phenomena led us to nickname our devices “Diode-NEMS” or “Depletion-NEMS,” which we usually abbreviate as D-NEMS. We frequently use the term D-NEMS throughout this manuscript.

2.2 Basic concepts in piezoelectricity

Piezoelectric phenomena arise in crystals lacking a center of inversion symmetry. A quantitative analysis is quite rigorous, and beyond the scope of this manuscript². The strength of piezoelectricity is measured by d_{ij} ($i, j=1 - 4$), which is the tensor representing the fractional length change (*i.e.*, strain) in the j^{th} direction per unit electric field pointing along the i^{th} direction. In the literature it is also common to encounter the parameter e_{ij} which is the polarization charge per unit area, though I find d_{ij} to be more intuitive. It has been determined that for GaAs, only a shear component of polarization, *i.e.*, e_{14} is present, which is related to the fact that it possesses a relatively simple crystal structure. Experimentally it was found¹² that $e_{14}=-0.16\pm 0.02$ C/m². The magnitude of this value can be estimated from the surface charge density on a face of the crystal $|e_{14}| \approx f_i q / a^2 = 0.16$ C/m², where $f_i=0.32$ is the ionicity of the compound¹³, q is the electronic charge and a is the lattice constant. This expression provides insight into why purely covalent crystals like silicon and germanium do not exhibit piezoelectric effects. To convert to the more intuitive parameter \mathbf{d} we must multiply \mathbf{e} by the elastic stiffness tensor for cubic crystals, $d_{ij} = c_{ik} e_{jk}$. Thus the piezoelectric strain constant is given by $d_{14}=c_{44}e_{14}=-2.72\pm 0.32$ pm/V.

From this parameter it is not immediately apparent how a shear strain can induce nonshear modes of motion. All our devices are designed to be flexurally excited out of the (001) plane. Fricke¹⁴ has shown that the shear strain translates into a longitudinal deformation by the symmetry transformation

$$d_{3j} = (d_{14} / 2) \sin 2\phi_j \quad (2.1)$$

and the corresponding *transverse* piezoelectric strain is $e_j = d_{3j}E_3$. This expression describes the strain at an angle ϕ_j from [100] due to an orthogonal electric field along the [001] axis, *i.e.*, out of the wafer plane. The largest strains occur along [110] and [1-10]. Note the sign difference between these directions, which signifies that a GaAs beam subjected to an electric field along [001] will contract, expand and remain unstrained along [110], [1-10] and [100], respectively. For convenience, the transverse piezoelectric constant along [110] is referred to as $d_{31} = -1.36 \pm 0.16$ pm/V. It is also worth emphasizing that $d_{ii} = 0$ in GaAs (though not in other compounds, such as quartz), meaning that there is no strain parallel to the electric field. This places additional constraints on permissible electrode configurations that are suitable for piezoelectric actuation. Problems pertaining to low actuation efficiency associated with the low d_{31} constant of GaAs relative to other materials such as lead zirconium titanate (PZT), can be countered by increasing the electric field strength or growing ultrathin films. The breakdown field of GaAs is ~ 40 mV/nm, so for a 50 nm insulating layer in our *pin* diodes we can apply about 2 volts (slightly more because of carrier depletion) before encountering problems. Interestingly, the strains generated per unit volt in a 50 nm GaAs junction are actually larger than those from 100 μm thick PZT stacks. Finally, stress-induced piezoelectric voltages arise from currents and cannot be calculated by taking the reciprocal of $e_x = d_{zx}E_z$, as might be naively expected. The correct approach is outlined in Chapter 6.

2.3 Multilayer piezoelectric actuation scheme

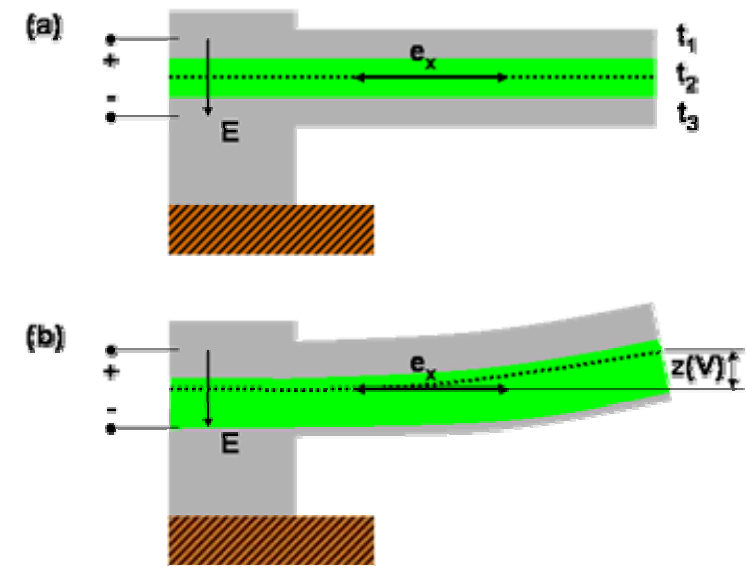


Figure 2.1 Trimorph piezoelectric actuation scheme for a cantilever. The gray and green represent the electrodes (t_1 & t_3) and piezoelectric (t_2) layers, respectively. The neutral axis is shown as a dotted line. The axial strain e_x is caused by a vertically oriented electric field. In case (a) there is no vertical actuation because $t_1=t_3$, so the bending moment is zero. In case (b) there is a net bending moment because of the asymmetry between the top and bottom halves of the cantilever.

The multilayer scheme (sometimes referred to as multimorph actuation) is commonly used for exciting ferroelectric MEMS and larger devices, and recently it has been employed in $3.5\ \mu\text{m}$ thick III-V heterostructures⁵. We are the first to employ this in submicron thick semiconducting devices, and we will demonstrate that this size reduction gives rise to some new electromechanical behavior. This actuation scheme involves sandwiching a highly resistive GaAs layer between two highly doped metal-like layers that serve as electrodes. Application of a voltage across the electrodes induces a piezoelectric strain that is concentrated within the middle highly resistive layer, where the electric field is strongest. Flexural motion occurs when an asymmetric longitudinal strain develops across the neutral axis; the more distant the strain from

that axis, the stronger the bending moment. The longitudinal strain induced by a transverse electric field is given by

$$e_j = d_{3j}E_3 = d_{3j}V / t_{piezo} \quad (2.2)$$

The static vertical deflection as a function of voltage in a cantilever of length L is given by¹⁵

$$z(V) = (3L^2 d_{3j} V / t_{tot}^4) [t_1(t_1 + t_2) - t_3(t_3 + t_2)] \quad (2.3)$$

If the driving signal is modulated at the mechanical resonance frequency, the vibrational amplitude will be enhanced in proportion to its quality factor. Thus the resonance amplitude for a specified dc bias V_0 and ac bias v_{AC} is

$$A(V_0, v_{AC}, t) = (Q/2) [z(V_0 + v_{AC} \sin \omega_{res} t) - z(V_0 - v_{AC} \sin \omega_{res} t)] \quad (2.4)$$

2.4 Impact of carrier depletion on piezoelectric diode actuation

Under most circumstances, the addition of a dc bias has no effect on the amplitude of vibration, because $z(V)$ is a linearly varying function of voltage. But semiconductors are different from insulators in a key respect: charge carriers can be controlled in semiconductors by selective doping or biasing methods. The depletion of carriers effectively blurs the distinction between the outer electrode and inner insulating piezoelectric layers, giving rise to a nonlinear $z(V)$ response.

We must therefore modify the static deflection to include bias-dependent thicknesses:

$$z(V) \rightarrow z_S(V) = [3\xi(V)L^2 d_{3j} V / t_{tot}^4] \{t_1(V)[t_1(V) + t_2(V)] - t_3(V)[t_3(V) + t_2(V)]\} \quad (2.5)$$

where the subscript ‘‘S’’ denotes the presence of semiconductor effects. The additional parameter $\xi(V)$ is the fractional voltage contributing to piezoelectric strain and is assumed to equal unity, although in practice it is a little lower than that and depends on the semiconductor structure. In the structures we shall use we expect ξ to vary slowly relative to other parameters, and can therefore reasonably assume it to be a constant. The primary insight gained from Eqn. 2.5 is that

the individual layer thicknesses are no longer fixed, and the nonlinearity should give rise to a dc bias-dependent mechanical resonance amplitude. The precise value of $z_s(V)$ is crucially dependent on the bandstructure. In our experiments we will employ a *pin* diode (a more general form of the *pn* diode with an intrinsically doped or insulating layer in the middle) because diodes are the simplest solid state devices to model. This scheme can certainly be extended to other semiconductor layer configurations, such as bipolar junction transistors. However, an important constraint worth remembering is to keep the piezoelectric region highly resistive relative to other regions, otherwise the actuation efficiency will be degraded. This is not always an intuitive process and some care should go into properly designing the structure before it is grown. For instance, we have found that *nin* or *pip* junctions with 50 nm thick intrinsic layers perform very poorly in this regard. On the other hand *pin* and *npn* junctions have much higher resistances. We will say more on impedance-related attenuation effects in the next section.

In the abrupt junction approximation¹⁶, the carrier depletion width of a *pin* diode can be expressed as

$$\begin{aligned}
 d_{tot}(V) &= d_p(V) + t_{m,0} + d_n(V) = \sqrt{t_{m,0}^2 + 2\varepsilon N_{tot}(V_{bi} - V)/(eN_A N_D)} \\
 d_p(V) &= (N_D / N_{tot})[d_{tot}(V) - t_{m,0}] \\
 d_n(V) &= (N_A / N_{tot})[d_{tot}(V) - t_{m,0}]
 \end{aligned} \tag{2.6}$$

N_A and N_D represent the *p*- and *n*-type doping concentrations, respectively; ε is the dielectric constant of GaAs; and $t_{m,0}$ is the as-grown intrinsic layer thickness. V_{bi} is the built-in potential and is given by $(k_B T / e) \ln(N_{D,A} N_m / n_i^2)$ where $n_i \approx 2 \times 10^6 \text{ cm}^{-3}$ is the intrinsic GaAs carrier concentration. Based on the doping level of the diode we shall use a value of $V_{bi} = 1.2 \text{ V}$. The depletion region expands under reverse bias and contracts under forward bias. Our simple model breaks down in the vicinity of $V = V_{bi}$ because of additional carrier diffusion effects; thus we will focus on the region where $V \leq V_{bi}$. We assume that all dopants are fully ionized at room temperature. The molecular beam epitaxy method used to grow our diodes is very nearly, but not

quite, perfectly clean. As a result our collaborators report an unintentional background doping that is p -type and has a concentration of $N_m \sim 10^{15} \text{ cm}^{-3}$. Thus strictly speaking we should modify our depletion width expression to account for the finite carrier concentration in the middle layer, but in practice the intentional impurities are added at much higher levels (N_D and N_A are 10^{18} to 10^{19} cm^{-3}) so the middle layer carriers can be ignored.

The depletion width expressions (Eqns. 2.6) provide insight into the dual role of p - and n -doped layers as electrodes and insulators. Forward biasing the diode confines the piezoelectric strain to a narrower region, while a reverse bias extends the strain's spatial distribution. Figure 2.2 shows the electric field distribution in the diode based on the abrupt junction approximation. The E-field is maximum in the as-grown middle layer, and decays linearly to zero at a distance $d_p(V)$ and $d_n(V)$ in the p and n layers, respectively. Note that d_p and d_n need not be equal and in fact, they will deliberately be made different. Piezoelectric strain is directly proportional to the electric field, so it is evident that the average strain in the sidebands of the depletion region is located halfway to the edge of the sidebands. Thus the discrete layer thicknesses can be approximated as follows:

$$\begin{aligned} t_p(V) &= t_{p,0} - d_p(V)/2 \\ t_m(V) &= t_{m,0} + d_{tot}(V)/2 \\ t_n(V) &= t_{n,0} - d_n(V)/2 \end{aligned} \tag{2.7}$$

In this representation $t_p(V)$ and $t_n(V)$ are the electrode layers and $t_m(V)$ is the piezoelectrically active layer. These expressions can be substituted into the three-layer actuation model for $z_s(V)$ and $A(V_0, V_{AC}, t)$ to obtain the amplitude of deflection on and off the mechanical resonance.

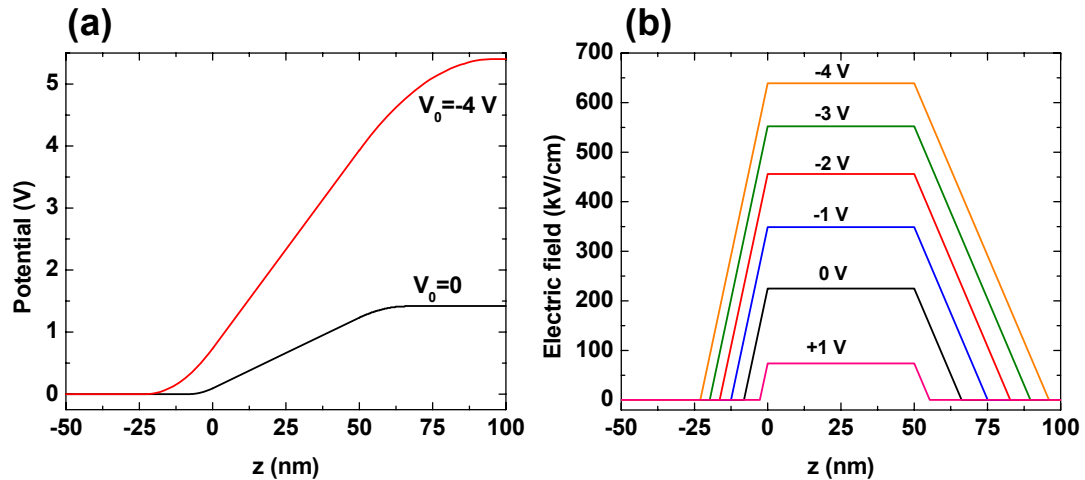


Figure 2.2 (a) Potential and (b) electric field distribution in a model GaAs *pin* diode under different applied bias V_0 . The doping profile is $n=2 \times 10^{18} \text{ cm}^{-3}$ (left), $p=1 \times 10^{18} \text{ cm}^{-3}$ (right). The intrinsic layer lies between $z=0$ to 50 nm . The built-in potential is 1.4 V . From (b) it is evident that the electric field spreads out more readily in the lower doped side.

2.5 D-NEMS device fabrication

Armed with a model of piezoelectric semiconductor actuation, the next step is to test it on some devices. In order to demonstrate doping and bias dependence separately, we construct resonators from three epitaxially grown *pin* diodes having different doping profiles. The epilayers were provided by our collaborators at the Inter-university microelectronics center (IMEC) in Belgium. The doping level and thickness of the individual *pin* epilayers, listed in Table 2.1, are preceded by a 550 nm thick $p\text{-Al}_{0.8}\text{Ga}_{0.2}\text{As}$ layer for suspended structure processing, buffer layers and a highly doped (001) $p\text{-GaAs}$ substrate. The acceptor and donor ions are beryllium and silicon, respectively. The concept of doping the substrate was adopted from the laser diode industry, and provides a very robust way of creating a low-resistance (Ohmic) contact to the bottom electrode. The finite carrier mobility is not expected to cause any signal delay problems until we push well into the gigahertz regime¹⁶ – safely above our operating limit. Future devices could be pushed to even higher operating frequencies, by using an *n*-type substrate, which has higher mobility, or lapping it to reduce its thickness and carrier transit time.

	Diode name		
Layer	<i>pin-1</i>	<i>pin-2</i>	<i>pin-3</i>
n	100 nm, 10^{19} cm^{-3}	100 nm, 10^{19} cm^{-3}	50 nm, 10^{19} cm^{-3}
i	50 nm, 10^{15} cm^{-3}	50 nm, 10^{15} cm^{-3}	50 nm, 10^{15} cm^{-3}
p	50 nm, 10^{18} cm^{-3}	50 nm, 10^{19} cm^{-3}	100 nm, 10^{18} cm^{-3}
sacrificial	550 nm, 10^{18} cm^{-3}	550 nm, 10^{18} cm^{-3}	550 nm, 10^{18} cm^{-3}
substrate	$1 \times 10^{19} \text{ cm}^{-3}$	$1 \times 10^{19} \text{ cm}^{-3}$	$1 \times 10^{19} \text{ cm}^{-3}$

Table 2.1 Doping profile of the three GaAs *pin* diodes. The n-type layer is always grown on top. The sacrificial layer consists of p-Al_{0.8}Ga_{0.2}As, and the substrate is (001) p-GaAs.

Fabrication proceeds as follows: In each diode a sequence of electrode depositions, electron beam lithography, 70 nm thick Ti mask evaporation and ion beam etching techniques is carried out to fabricate identical cantilevers with dimensions $(L, w, t)=(4, 0.8, 0.2) \mu\text{m}$, and alignment along the [110] and [1-10] directions with an accuracy of ~ 5 degrees. The devices are finally released from the substrate by selectively removing the exposed p-Al_{0.8}Ga_{0.2}As layer in dilute hydrofluoric acid, which also serves to remove the Ti mask. The reader is referred to the suspended structure process flow in Chapter 1 for more detailed information. The top electrical contact is made via a $150 \times 150 \mu\text{m}^2$ Au electrode placed adjacent to the devices. Prior to Au deposition, a thin film of Ti is added to assist adhesion. A ground electrode is placed on the back side of the wafer using the same process. The diode terminals are biased with an ac voltage for mechanical actuation (see Fig. 2.1) and a dc voltage for modifying the mechanical resonance. We shall refer to an electric field along [001] as a positive, or forward, diode bias. Note that electrostatic interactions between the substrate and diode surfaces can be neglected for the

applied range of voltages, as we will see in the next chapter. The completed devices are shown in Fig. 2.3, and their predicted behavior is depicted in Fig. 2.4.

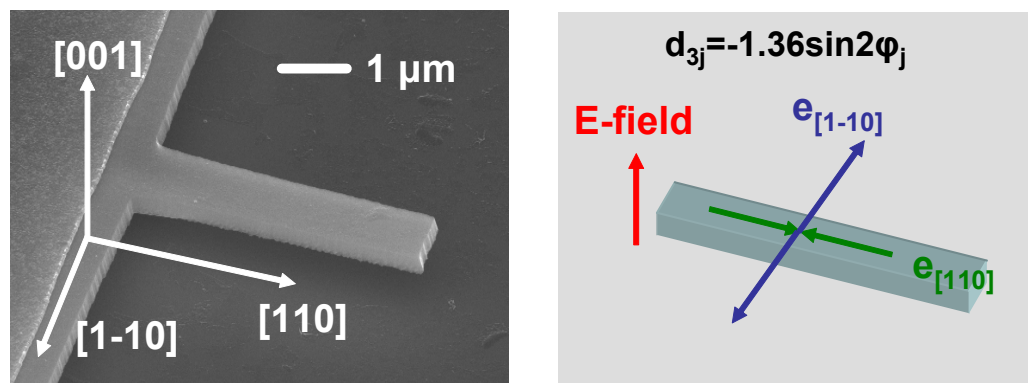


Figure 2.3 (a) SEM image of 4 μm long *pin* diode-embedded cantilever, with crystallographic axes. (b) Direction of transverse piezoelectric strains due to a positive electric field.

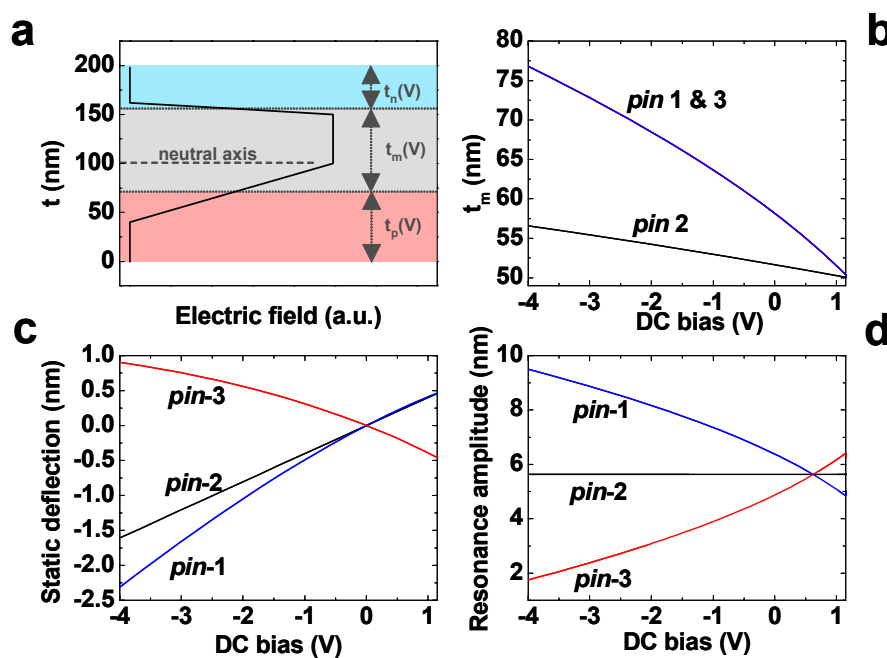


Figure 2.4 (a) Model electric field distribution in *pin* diode, illustrating the tunable actuation concept. If the *p* and *n* layers are doped differently, then the piezoelectric strain distribution with respect to the neutral axis will vary with voltage. (b) Calculated thickness of piezoelectric middle layer vs. dc bias. (c) Calculated bias dependence of static and (d) resonant displacement of a device with $L=4 \mu\text{m}$, $Q=1,000$ and $V_{AC}=10 \text{ mV}_{RMS}$.

2.6 Driving signal attenuation and diode equivalent circuit

So far the finite impedance of the piezoelectrically active middle layer has been ignored. However, both the diode's resistance R_d and junction capacitance C_j will depend on applied voltage, so we cannot necessarily neglect the possibility that part of the radio-frequency driving signal will be attenuated. The model for signal attenuation effects is based on the equivalent circuit of D-NEMS resonators, depicted in Fig. 2.5a. A *pin* diode can be treated as a variable resistance and junction capacitance in parallel, and in series with the resistance of the contacts and intrinsic layer. We also add motional LCR components after the Butterworth-Van Dyke model of crystal resonators. The parameter C_m is related to the stored electromechanical energy and is given by $C_m = \eta^2 / k$, where η is the electromechanical coupling factor defined as the force-voltage proportionality ratio, *i.e.* $F = \eta V$, and $k = 3YI / L^3$ is the cantilever spring constant. The bending force $F(V) = kz(V)$ is supplied by the transverse piezoelectric effect. Therefore the motional LCR components of the diode-NEMS can be found from the relations

$$\begin{aligned} C_m &= k (dz / dV)^2 \\ L_m C_m &= 1 / \omega_0^2 \\ R_m / L_m &= \omega_0 / Q \end{aligned} \quad (2.8)$$

For our $4 \times 0.8 \times 0.2 \text{ } \mu\text{m}^3$ cantilevers, we calculate $k = 2.8 \text{ N/m}$, and from Fig. 2.4c, $dz / dV \approx 0.5 \text{ nm/volt}$. The corresponding motional capacitance is $C_m \approx 5 \times 10^{-18} \text{ F}$, giving an impedance of $30 \text{ G}\Omega$ at 10 MHz . This is at least 100 times greater than the resistance of the diode, so henceforth motional impedance effects shall be ignored. The entire circuit is in series with a contact electrode and other external impedances, which are on the order of $50 \text{ }\Omega$. As long as the total diode impedance greatly exceeds the contact's resistance, most of the driving voltage will contribute toward piezoelectric actuation. From the circuit, we obtain the actuation efficiency as a function of dc bias:

$$v_{AC}/v_{AC,0} \approx R_d / \sqrt{(R_0 + R_d)^2 + (\omega R_0 R_d C_j)^2} \quad (2.9)$$

The diode resistance and capacitance are respectively given by $R_d(V)=dV/dI$ and $C_j(V)=\epsilon A/d_{tot}(V)$, where A is the contact electrode plus mechanical device area, and equal to $150 \times 150 \mu\text{m}^2$ in this set of devices. The $I(V)$ curves of the three *pin* diodes are displayed in Fig. 2.5b, and the corresponding ac driving efficiencies calculated from the above expression are plotted in Fig. 2.5c.

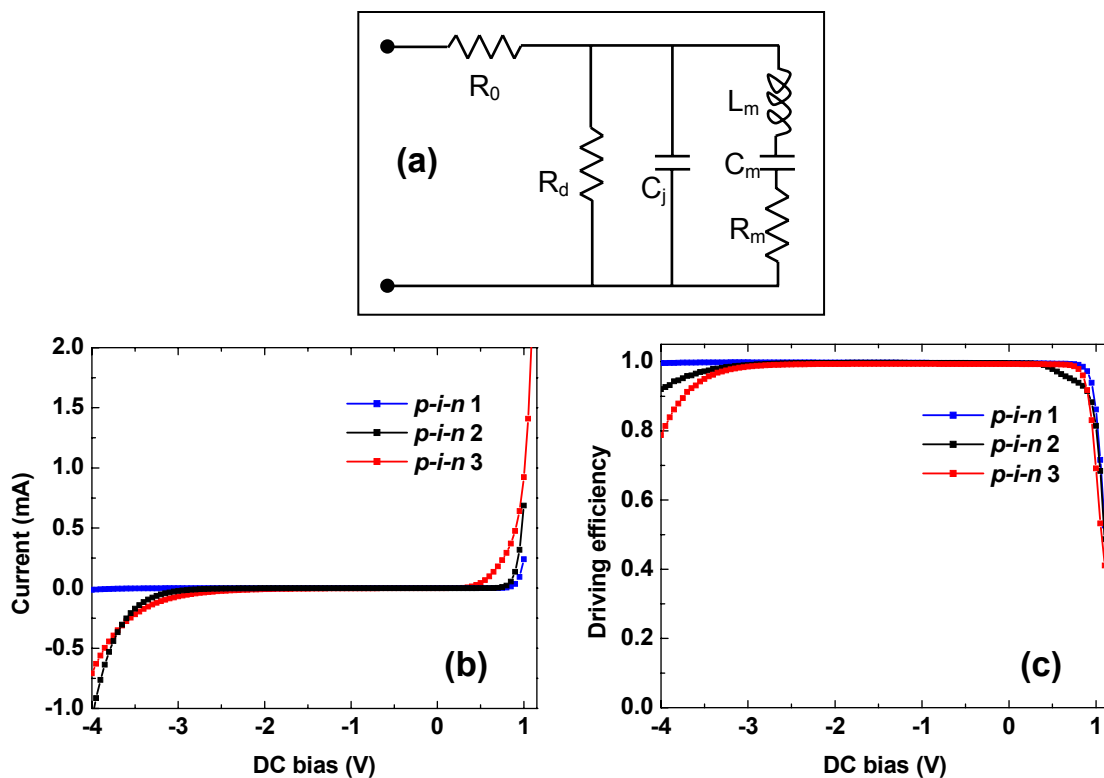


Figure 2.5 (a) Equivalent circuit of mechanical *pin* diode resonator. R_0 , $R_d(V)$, $C_j(V)$ are the contact resistance, diode resistance and junction capacitance, respectively. The estimated motional circuit components have ~ 100 times higher impedance than other components, and can thus be neglected in the analysis. (b) Measured $I(V)$ curves of the three *pin* diodes and (c) the calculated driving efficiency of a 10 MHz signal. The efficiency from -3 to 0.8 V is very close to 100%; elsewhere it drops quickly because of the diode's bias-dependent resistance.

2.7 Mechanical detection with optical interferometry

The primary motivating factors for employing optical detection are: (i) it is simple to implement and (ii) we wished to investigate new actuation techniques and had no need to prove elaborate read-out schemes. Nonetheless, we recognize the importance of all-electrical transduction and discuss it further in the sixth chapter. This section briefly outlines the optical interferometry technique¹⁷ used to measure the rf displacement of our devices. GaAs heterostructures have the attractive feature of being epitaxially grown on a nearly perfectly lattice-matched sacrificial layer, $\text{Al}_{0.8}\text{Ga}_{0.2}\text{As}$, which can be removed with a high degree of selectivity to reveal a highly smooth substrate that can form a mirror. The other mirror is formed at the top surface of the NEMS device. Coupled together, the mirrors produce a primitive Fabry-Perot interference cavity, as illustrated in Fig. 2.6a. The reflection coefficient for light that is normally incident to a vacuum-GaAs interface is about 33%, and because of the relatively low light intensity, it is sufficient to consider a single reflection from each surface. The change in total intensity of the reflected light can be shown to be $\Delta A_{\text{tot}} \propto |2 \cos 2ka|$, where $k=2\pi/\lambda$ and a is sum of cantilever and sacrificial layer thickness. This expression is plotted in Fig. 2.6b as a function of gap spacing. Note that we deliberately choose an infrared laser diode (904 nm) whose energy is below the band gap of GaAs (830 nm), in order to minimize heating and photocurrent generation. The laser is biased with 35 to 45 mA, which corresponds to a power output of ~ 3 to 4 mW. Unless otherwise stated, we also employ a neutral density filter to block 90% of the light. Figure 2.7 shows the experimental setup. The driving amplitude is always kept sufficiently low to ensure a linear correspondence between device motion and detector signal. The focusing lens has a numerical aperture of 0.15, giving a minimum resolvable beam spot size of 4 μm . Although this is almost an order of magnitude wider than our beams, it is not found to be a hindrance in detection nanomechanical displacements. The spot size at the device is estimated to be 20 to 40 μm in diameter.

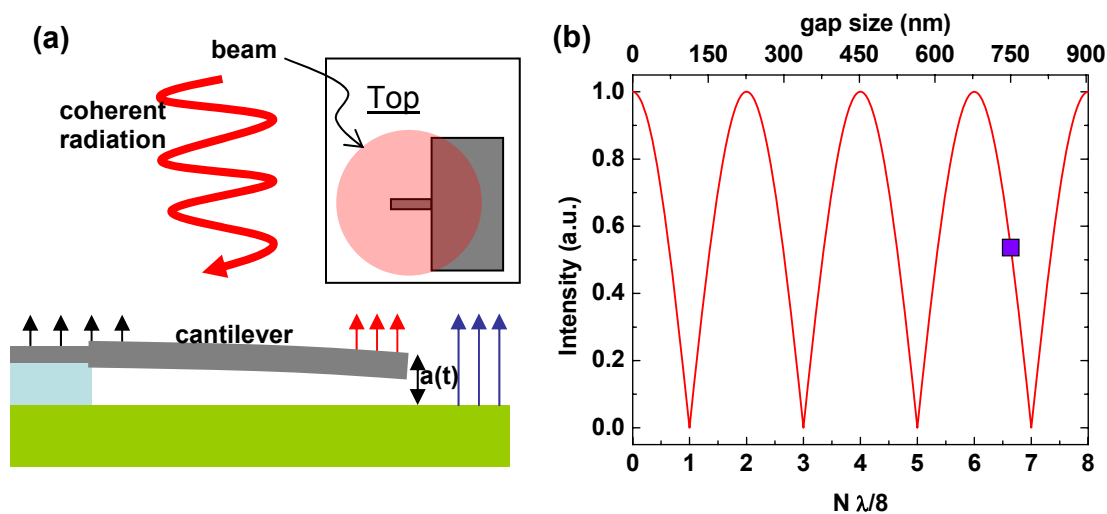


Figure 2.6 (a) Illustration of principles of optical interferometric displacement detection. The interfering signals are from the GaAs substrate and top of the nanomechanical device. The width of the cantilever is deliberately kept above $\lambda/2$ to strongly avoid diffraction effects. The inset shows a top view of the device in roughly the actual size ratio with respect to the focused laser spot. (b) Calculated intensity of coherent light with $\lambda=904$ nm reflecting off two surfaces as a function of gap spacing. The purple square shows the nominal operating point of the D-NEMS devices (750 nm = 550 nm sacrificial + 200 nm device thickness).

2.8 Experimental data

All measurements are carried out at room temperature and 10 mTorr pressure. The first out-of-plane resonance mode of a cantilever made from diode *pin-1* is plotted under different driving amplitudes in Fig. 2.8a. As expected, the resonance amplitude increases linearly with drive. Interestingly, the multilayer piezoelectric actuation mechanism is strong enough to produce a measurable response from a $10 \mu\text{V}_{\text{RMS}}$ drive, which corresponds to a modulation of just ± 1 electronic charges on the device. It is intriguing to think about an experiment in which piezoelectric strains from single electrons are measured – this possibility is discussed more in Chapter 5. Thus we have successfully shown that D-NEMS provide highly efficient piezoelectric

actuation. The other two *pin* diodes exhibit similar behavior and have frequencies between 7.5 to 9 MHz, with quality factors ranging between 1,000 and 2,000.

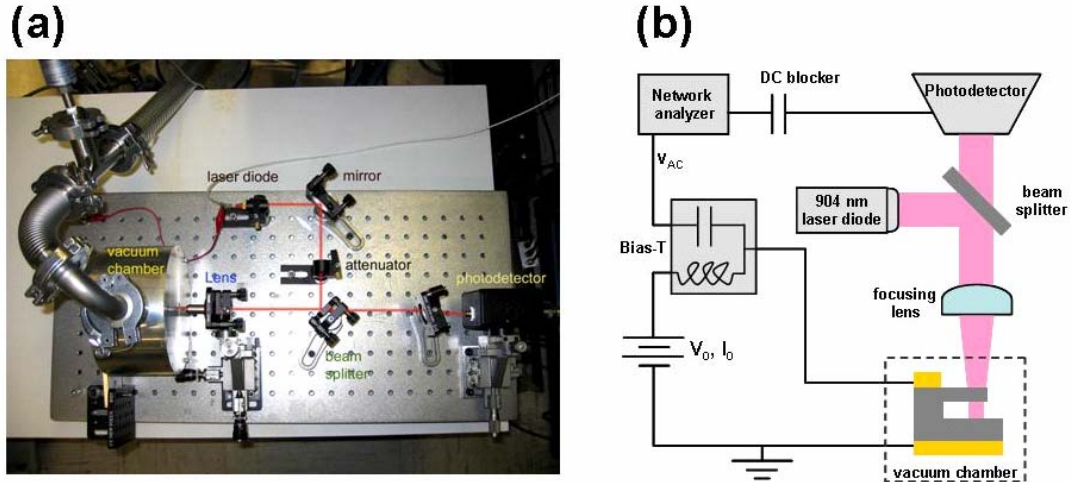


Figure 2.7 (a) Image of experimental setup. The mirror and beam splitter are mounted on tiltable supports and the lens and photodetector are mounted on movable xyz positioning stages. (b) Schematic of setup used to actuate and bias the NEMS resonators with a superposition of ac and dc signals.

Next we try to modify the actuation by dc-biasing the diodes. Figure 2.8b shows the resonance of the same device under constant ac drive and different dc potentials. The amplitude increases by $\sim 10\%$ in reverse bias and appears to sharply decay near 1 volt forward bias. We attribute these dc bias-dependent changes in rf actuation to the tunable electromechanical coupling between piezoelectric strain and carrier depletion, as well as signal attenuation due to nonlinear diode $I(V)$ performance, as predicted in previous sections of this chapter.

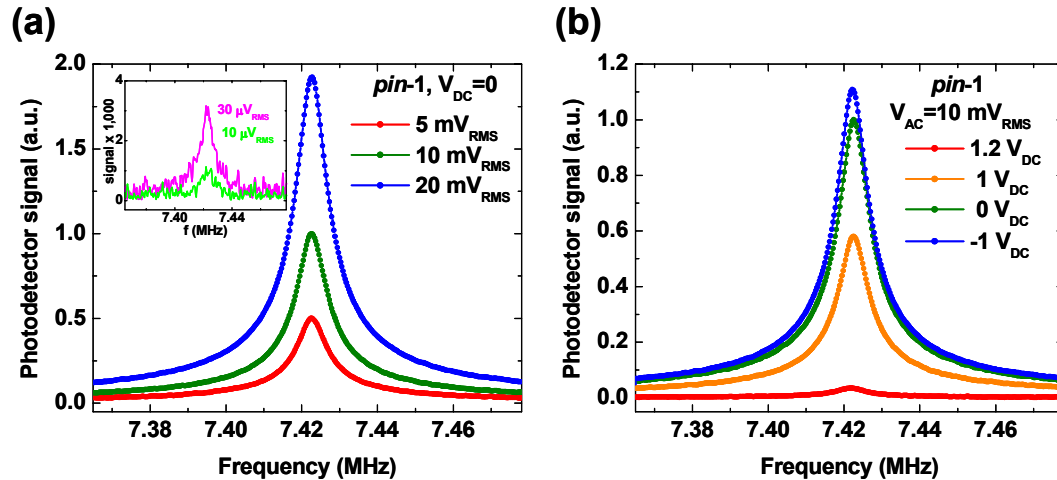


Figure 2.8 (a) Resonant response of the $4 \times 0.8 \times 0.2 \mu\text{m}^3$ cantilever shown in Fig. 2.3a, under different ac driving voltages and fixed dc bias. The inset shows the response to 30 and $10 \mu\text{V}_{\text{RMS}}$ signals, which correspond to about ± 3 and ± 1 electronic charges on the device, respectively. The quality factor is 1,200. (b) Resonant response of the same device under fixed ac and varying dc bias. Variations in resonance amplitude with dc bias are attributed to tunable electromechanical coupling due to a combination of carrier depletion and variable diode impedance.

The peak resonance amplitude of the cantilevers is now measured as a function of dc bias. The results, which are presented in Figure 2.9, qualitatively agree with our theoretical predictions developed in Sections 2.3 – 2.6. The predictions are shown as an inset to the figure. We attribute the nanomechanical resonance amplitude modulation effect observed between -3 and 0.5 volts to piezoelectric strain redistribution by carrier depletion, and the remainder to ac signal attenuation. As predicted, under moderate reverse bias, diodes *pin-1*, *pin-2* and *pin-3* exhibit positive, nearly zero and negative change in their respective resonance amplitudes, indicating that electronic bandstructure can be tailored to tune mechanical behavior. Similar results, which are not displayed, are found for cantilevers aligned along [1-10] and also for doubly clamped beams as well as shorter, higher frequency devices. Therefore this appears to be a reproducible effect, which may represent the first demonstration of a bandstructure engineering level of control of nanoscale mechanical behavior.

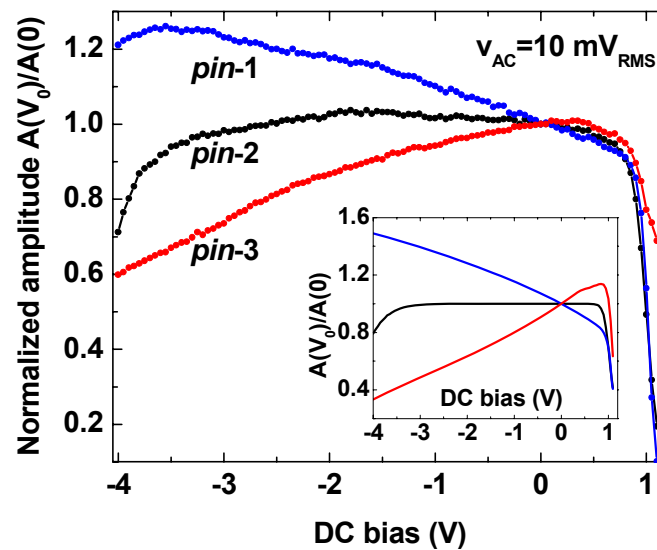


Figure 2.9 Measured resonance amplitude vs. dc bias of the three *pin* diodes under fixed ac drive. The inset shows the predicted behavior derived from the model of piezoelectric actuation that incorporates both carrier depletion and signal attenuation effects. For clarity, results are normalized to the zero bias amplitude of each device. The qualitative agreement between experiment and theory appears to confirm that piezoelectric actuation in suspended semiconductor nanostructures can be tuned by controlling the electronic bandstructure.

2.9 Modulation doping from the *p*-AlGaAs layer

Several overlooked factors could help account for the discrepancies between the experimental data and theory in Fig. 2.9, including nonuniform piezoelectric strain distribution in the depletion region, trapped *p* and *n* layer surface charges, and finite device geometry. Surface depletion from trapped charges could lead to additional bending moments that offset the bias dependence of amplitude. The thin cross-section is also a concern, particularly when exacerbated by surface depletion. So far the sacrificial *p*-AlGaAs layer has been assumed not to influence the electromechanical coupling efficiency in the *pin* diodes. But strictly speaking this is not true; charges can be transported across the GaAs/AlGaAs heterojunction. In particular, *p*-AlGaAs may modulation-dope the *p*-GaAs layer that serves as the bottom D-NEMS “electrode,” leading to an increased carrier concentration in that layer and subsequently, a modified electromechanical

coupling efficiency. At most the hole contribution from modulation doping is equal to the doping level of the $p\text{-Al}_{0.8}\text{Ga}_{0.2}\text{As}$ layer, or 10^{18} cm^{-3} . Figure 2.10 plots the resonance amplitude data superimposed with the model using the modified carrier concentration parameters, revealing a substantially improved fit. Thus, it appears that modulation doping could be the most important previously overlooked factor in determining piezoelectric actuation. It is worth noting that since the valence and conduction band offset at the GaAs/AlGaAs heterojunction is greater than kT/q but less than the energy of the laser beam used for detection, it is likely that the concentration of modulation-doped carriers can vary slightly with both applied bias and illumination level. A possible manifestation of such charge transport is discussed in Section 3.6.

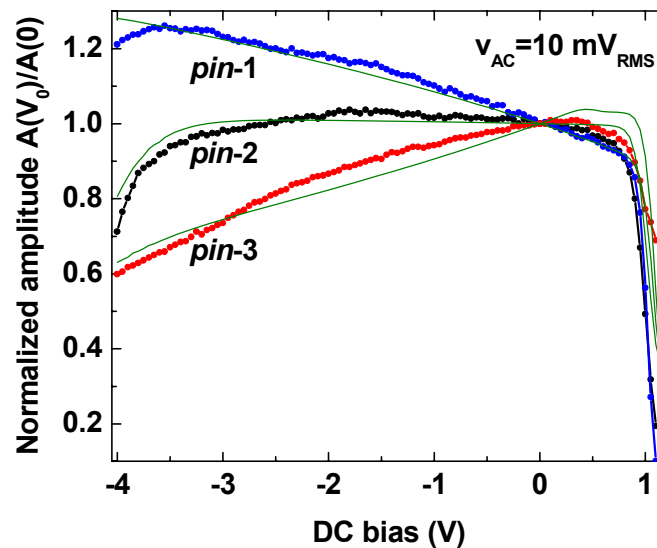


Figure 2.10 Normalized resonance amplitude vs. dc voltage for the three *pin* diodes. The superimposed lines represent the predicted actuation assuming the sacrificial AlGaAs layer modulation-dopes the $p\text{-GaAs}$ “electrode” with a uniform, 10^{18} cm^{-3} concentration of holes. The total $p\text{-GaAs}$ hole density is therefore assumed to be the as-grown $p\text{-GaAs}$ + $p\text{-AlGaAs}$ doping level.

2.10 D-NEMS actuation under a large forward bias

The regime of high forward bias associated with the “on” state of regular diodes represents a highly unfavorable operating point for Diode-NEMS because of the large signal attenuation effects. This is shown in Fig. 2.11, where it is evident that the signal is almost fully attenuated at the built-in potential of 1.2 V. Above this value, only one of the diodes (*pin-3*) has any kind of measurable response. For the other diodes, we have effectively turned off their electromechanical coupling to piezoelectric strain.

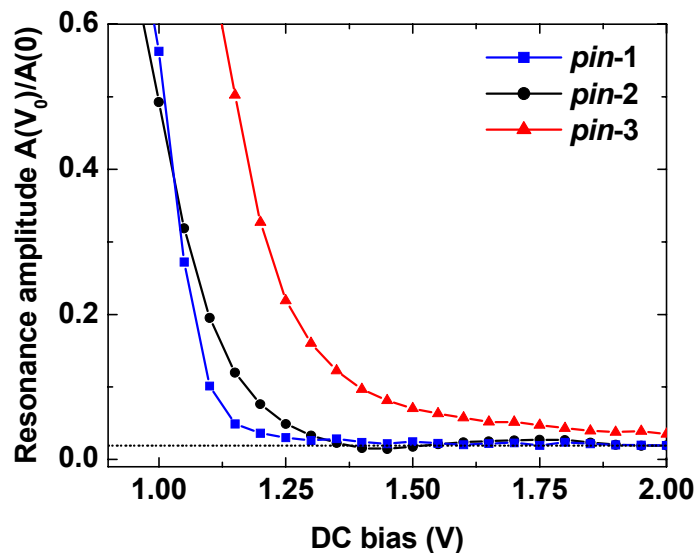


Figure 2.11 Normalized resonance amplitude vs. dc voltage in the large forward bias regime. The nominal driving signal is 10 mV_{RMS}. The dashed line denotes the noise floor. After 1.2 V the actuation is severely attenuated; only one of the three diodes still has a measurable response at 2 V.

Due to the large power requirements of this operating regime, it is preferable to design a semiconductor whose bandstructure enables on/off operation at moderate reverse bias fields. We believe this could be achieved with improvements to a structure similar to diode *pin-3*. There are a host of tricks one could try to enhance electromechanical coupling effects, such as using a graded doping profile. The ability to turn a resonator “off” using a modulating signal that is independent of its driving signal may offer new capabilities in NEMS design. For instance, it

enables the responsivity of selected components in a D-NEMS array to be fine-tuned. This could be particularly useful in telecommunications filter applications. It may also result in signal processing devices that rely on nanomechanical amplitude modulation instead of ordinary electrical AM.

2.11 Piezoelectric actuation of a nanomechanical *npn* junction

To demonstrate the generality of this actuation scheme to other semiconductor structures, we fabricate identical cantilevers out of a GaAs *npn* bipolar transistor. From top to bottom, the doping profile is: 100 nm n-GaAs (10^{19} cm^{-3}) / 50 nm p-GaAs ($2 \times 10^{18} \text{ cm}^{-3}$) / 50 nm n-GaAs ($2 \times 10^{18} \text{ cm}^{-3}$) / 550 nm n-Al_{0.8}Ga_{0.2}As / n⁺-GaAs substrate. Figure 2.12 shows the measured mechanical properties of these devices. We find that GaAs bipolar transistors can be actuated with a comparable efficiency to *pin* diodes. Thus bandstructure engineering of piezoelectric semiconductor NEMS appears to be a robust technique that enables actuation of devices without any as-grown insulating layers, which is impossible to do with most other materials. The actuation model for bipolar transistors would involve five bias-dependent layers, two of which are piezoelectric, and owing to its complexity a detailed analysis has not been carried out. Instead we can qualitatively understand the observed bias dependence of the resonance amplitude by treating the transistor as two *pn* diodes sandwiched back-to-back. A negative voltage corresponds to a downward electric field vector, so most of the potential drop will occur at the upper *pn* junction. This places the piezoelectric strain closer to the neutral axis, so the bending moment, hence resonance amplitude, should decrease. Conversely, a positive voltage will bias the lowermost *pn* junction, shifting strain away from the neutral axis, so the bending moment should increase.

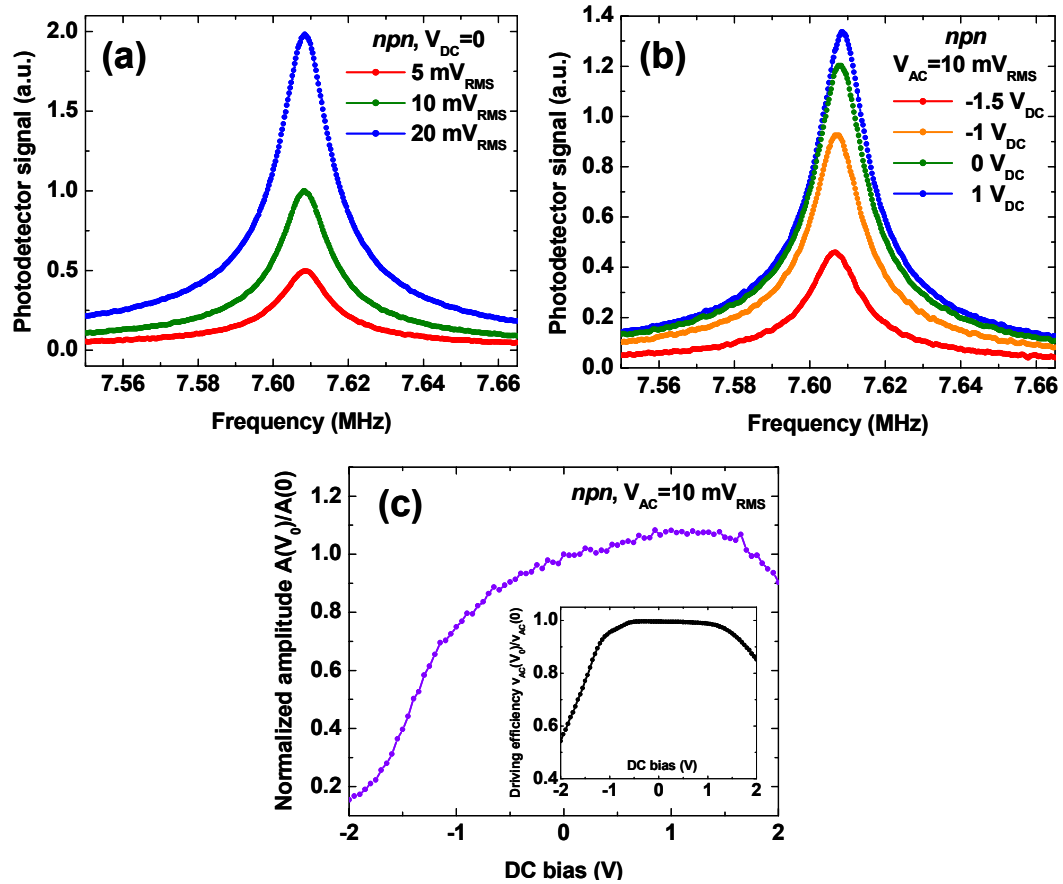


Figure 2.12 (a) Resonant response of an *npn* GaAs cantilever under different ac driving voltages and fixed dc bias. The quality factor of this device is 700. (b) Resonant response of the same device under fixed ac and varying dc bias. (c) Resonance amplitude vs. dc bias, with an ac drive of 10 mV_{RMS}. For clarity, results are normalized to the zero bias amplitude. The inset shows the corresponding signal attenuation at 8 MHz.

2.12 D-NEMS frequency-doubled actuation

The intrinsic nonlinearity of the diode's capacitance and resistance, as well as the bias-dependent actuation efficiency should give rise to some interesting modulation effects such as mixing and frequency multiplication. Here we demonstrate frequency doubling in cantilevers made from the three *pin* diode wafers. We excite the devices piezoelectrically in the usual manner with zero dc bias, but sweep the drive in the region of $f_{\text{res}}/2$ as well as f_{res} . The motion is detected optically and recorded with a digital lock-in, which is referenced to f during normal operation and $2f$ during

$f_{\text{res}}/2$ operation. This technique allows us to record the resonant response of a device while driving it at half its normal frequency. If no nonlinearity is present, there should be no response from an $f/2$ drive. Figure 2.13 shows the measured resonance amplitude as a function of driving voltage for the three diodes in both modes of operation. We find that all diodes exhibit some degree of frequency doubling, but diodes *pin-1* and *pin-3* show the strongest response. This is believed to be due to the fact that these diodes have larger depletion widths than diode *pin-2*, and should therefore have more nonlinear voltage-dependent effects.

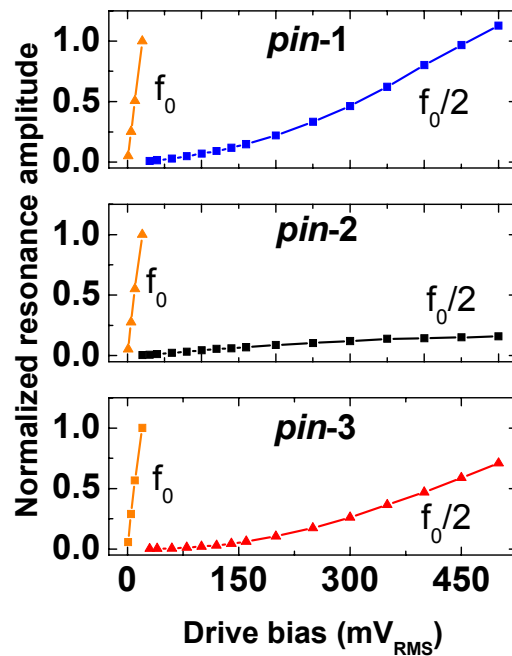


Figure 2.13 Measured resonance amplitude vs. ac voltage under linear drive (f_0) and frequency-doubled drive ($f_0/2$). The frequency-doubled coupling in devices made from diodes *pin-1* and *pin-3* demonstrate that these diodes exhibit stronger nonlinear voltage-dependent effects.

References

1. P. Curie & J. Curie, *C. R. Acad. Sci.* **91**, 294 (1880)
2. For a review see: W. G. Cady, *Piezoelectricity*, vol. 1, Dover, New York (1964)
3. M. D. Ward & D. A. Buttry, In situ interfacial mass detection with piezoelectric transducers, *Science* **249**, 1000-1007 (1990)
4. H. X. Tang, X. M. H. Huang, M. L. Roukes, M. Bichler, W. Wegscheider, Two-dimensional electron gas actuation and transduction for GaAs nanoelectromechanical systems, *Appl. Phys. Lett.* **81**, 3879-3881 (2002)
5. P. Kumar, L. Li, L. Calhoun, P. Boudreaux, D. Devoe, Fabrication of piezoelectric Al_{0.3}Ga_{0.7}As microstructures, *Sens. Actuat. A* **115**, 96-103 (2004)
6. R. G. Beck, M. A. Eriksson, R. M. Westervelt, K. L. Campman, A. C. Gossard, Strain-sensing cryogenic field-effect transistor for integrated strain detection in GaAs/AlGaAs microelectromechanical systems, *Appl. Phys. Lett.* **68**, 3763-3765 (1996)
7. R. Knobel & A. N. Cleland, Piezoelectric displacement sensing with a single-electron transistor, *Appl. Phys. Lett.* **81**, 2258-2260 (2002)
8. Y. Zhang & M. P. Blencowe, Sensitivity of a piezoelectric micromechanical displacement detector based on the radio-frequency single-electron transistor, *J. Appl. Phys.* **92**, 7550-7555 (2002)
9. H. Ukita, Y. Uenishi, & H. Tanaka, A photomicrodynamic system with a mechanical resonator monolithically integrated with laser diodes on gallium arsenide, *Science* **260**, 786-789 (1993)
10. G. Piazza, K. Castelino, A. P. Pisano, C. J. Chang-Hasnain, Design of a monolithic piezoelectrically actuated microelectromechanical tunable vertical-cavity surface-emitting laser, *Optics Letters* **30**, 896-898 (2005)
11. K. W. Goossen, E. A. Caridi, T. Y. Chang, J. B. Stark, D. A. B. Miller, R. A. Morgan, Observation of room-temperature blue shift and bistability in a strained InGaAs-GaAs <111> self electro-optic effect device, *Appl. Phys. Lett.* **56**, 715-717 (1990)
12. G. Arlt, & P. Quadflieg, Piezoelectricity in 3-V compounds with a phenomenological analysis of piezoelectric effect, *Phys. Status Solidi* **25**, 323 (1968)
13. J. C. Philips & J. A. Van Vechten, Dielectric classification of crystal structures, ionization potentials, and bandstructures, *Phys. Rev. Lett.* **22**, 705 (1969)
14. K. Fricke, Piezoelectric properties of GaAs for application in stress transducers, *J. Appl. Phys.* **70**, 914-918 (1991)

15. J. Soderkvist, Similarities between piezoelectric, thermal and other internal means of exciting vibrations, *J. Micromech. Microeng.* **3**, 24-31 (1993)
16. S. M. Sze, *Physics of Semiconductor Devices*, 2nd ed., (John Wiley, 1981)
17. D. W. Carr, & H. G. Craighead, Fabrication of nanoelectromechanical systems in single crystal silicon using silicon on insulator substrates and electron beam lithography, *J. Vac. Sci. Technol. B* **15**, 2760-2763 (1997)

Chapter 3

Piezoelectric frequency control of D-NEMS resonators

3.1 Piezoelectric frequency tuning

In Chapter 2 it was found that GaAs diodes embedded in nanomechanical resonators contain an efficient piezoelectric actuation mechanism. In addition to inducing flexural vibrations, piezoelectric strain leads to an axial tensile or compressive stress that should induce changes in the resonance frequency doubly clamped beams. The same principle of tensile/compressive loading is applied in tuning guitar strings. The aim of this chapter is to describe how piezoelectricity can be used to implement frequency control in D-NEMS. The general expression of the frequency of a beam of length L under an axial force F_x was solved by Timoshenko¹ and equals

$$f' = f_0 \left(1 - \frac{F_x L^2}{22.4 Y I} \right)^{1/2} = \frac{22.4}{2\pi L^2} \left(\frac{Y I}{\rho A} \right)^{1/2} \left(1 - \frac{F_x L^2}{22.4 Y I} \right)^{1/2} \quad (3.1)$$

where A is the cross-sectional area and I is the moment of inertia. Note that cantilevers should also experience frequency shifts because of lattice dilation, but this is a substantially weaker effect than that due to stress in doubly clamped beams. Under forces that satisfy the condition $f' / f_0 \approx 1$, this expression can be linearly expanded into the form

$$\Delta f \approx -\sqrt{3 / \rho Y} F_x / (2\pi A t) \quad (3.2)$$

Piezoelectric axial forces in GaAs, given by $F_{PZL} = Y w d_{31} V$ are sufficiently small in our devices (on the order of 120 nN/volt) that this approximation remains valid under the range of applied

voltages. However, care must be taken to ensure that other axial forces, *e.g.*, due to thermal expansion, lattice mismatch, *etc.* are also kept in check. The thermal expansion coefficient of GaAs is $\alpha=6$ ppm/K, giving rise to a force of $F_{therm} = wt_{tot}Y\alpha\Delta T = 110 \text{ nN} / K$. We shall show later in this chapter that light-induced heating is negligible. The constant force from the 0.11% lattice mismatch² at the GaAs/Al_{0.8}Ga_{0.2}As interface is $F_{lattice} = wt_{tot}Y\Delta a / a$ which is equal to an appreciable 20,000 nN. From Fig. 3.1a it appears that the linear approximation holds within this range of forces. Thus the frequency change induced by a transverse piezoelectric strain in doubly clamped beams is given by

$$\Delta f_{PZL}(V) = -\sqrt{3Y/\rho} d_{3j}V / (2\pi t_{tot}^2) \quad (3.3)$$

The above expression provides several valuable insights. First, unlike the electromechanical coupling that sets the dc bias-dependent actuation efficiency, frequency tuning should be independent of carrier depletion width. Thus it is not surprising that it has been reported in a few other piezoelectric resonators³. Nonetheless, bandstructure engineering is needed to optimize the device for high voltage, low current operation. In addition, frequency tuning depends quadratically on total sample thickness, implying that nanoscale devices are ideal systems for studying these effects. Second, the tuning should be linear and bidirectional with voltage. Lastly, the frequency tuning magnitude and directionality can be controlled by exploiting the piezoelectric crystalline anisotropy of GaAs. Recall that the piezoelectric constant⁴ is $d_{3j} = (d_{14}/2)\sin 2\phi_j$, so the largest frequency tuning should occur along [110] and [1-10] and should equal ± 39 kHz/volt for 200 nm thick devices. The frequency of a cantilever should vary much more slowly and on the order of the strain, *i.e.*, $\Delta f / f_0 \approx d_{31}V / t_m(V)$.

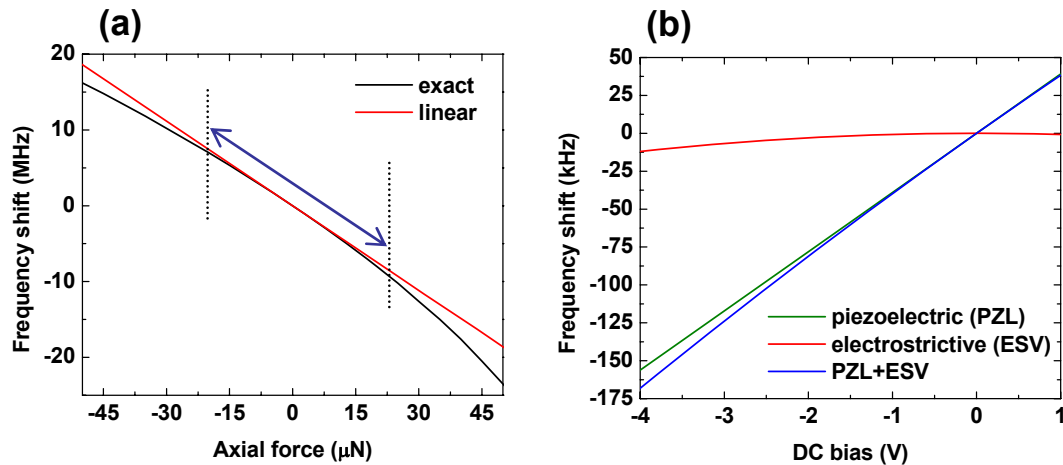


Figure 3.1 (a) Predicted resonance frequency shift vs. axial force of a GaAs beam calculated from the exact and linearized expression. We find close agreement between the two models in the range between -20 and 20 μN . The device is assumed to be a doubly clamped beam with dimensions $(L, w, t) = (4, 0.8, 0.2)$ μm and nominal resonance frequency of 61 MHz. (b) Calculated resonance frequency shift in a beam with $[110]$ alignment due to piezoelectric and electrostrictive effects in a *pin* diode with a 50 nm wide depletion layer. Piezoelectric effects are predicted to vary linearly with voltage, but the presence of electrostriction will add a small but observable quadratic bias dependence.

3.2 Electrostrictive frequency tuning

It is important to identify all sources of bias-dependent frequency tuning effects. First, electrostriction is often confused with piezoelectricity but the two effects are different. Piezoelectric stresses vary linearly with electric field, are reversible, and are only found in a limited class of materials. On the other hand, electrostriction is the term used to describe electrostatically induced squeezing that occurs in all dielectrics, which varies quadratically with field and is irreversible. If a dielectric such as our *pin* depletion layer is squeezed in the vertical direction due to electrostatic forces between the electrodes, it will also expand longitudinally, thereby giving rise to an additional frequency dependence on voltage. Two important features distinguish electrostrictive tuning from the piezoelectric case: First, because the dielectric

expands frequency will always be reduced; second, the tuning is a quadratically varying function of voltage. The amount of electrostrictive tuning in a doubly clamped beam is estimated to be

$$\Delta f_{ESV}(V) = -1.9\epsilon_d V^2 / [2\pi\sqrt{Y\rho}t_m(V)t_{tot}^2] \quad (3.4)$$

For typical device dimensions this gives a value of about -800 Hz/volt², implying that electrostriction is substantially weaker than piezoelectricity. Nonetheless, owing to its quadratic V dependence it should reach within about 10% of the piezoelectric tuning effect at the limit of our applied bias, near -4 V. Another important distinction apparent from the above formula is that electrostrictive phenomena are strongest in soft (*i.e.*, low Young's modulus) materials, suggesting that this actuation mechanism may be preferred over piezoelectricity in polymer nanostructures. Figure 3.1b shows the predicted frequency shift as a function of voltage due to piezoelectric (PZL), electrostrictive (ESV) and combined effects.

3.3 Electrostatic frequency tuning

The second obvious source of frequency tuning besides piezoelectric coupling is electrostatic interactions between the suspended devices and substrate. This should be negligible in our case because the *pin* diode is quite far from the substrate, and we would like to verify that here. Instead of calculating the entire frequency tuning expression it should suffice to show that the force due to electrostatic pull-down is negligible. The force is obtained by differentiating the electrostatic energy stored between the beam and substrate located a distance z away. Assuming a simple parallel plate capacitor geometry this leads to the result

$$F_z(z = d_g) = \epsilon_0 wLV^2 / (2d_g)^2 \approx 60 \text{ pN/V}^2 \quad (3.5)$$

where we have used a gap size of 550 nm and typical device dimensions. The force is about three orders of magnitude smaller than piezoelectric effects, so we can safely ignore external electrostatic interactions. The analysis of this and the previous section confirms that piezoelectric

stress should provide the largest coupling strength out of all possible electromechanical interactions.

3.4 Experimental data

Doubly clamped beams of various lengths were fabricated from diode *pin-1* by the method described in Chapter 2 and aligned along the [110] and [1-10] directions. They are actuated with 70 mV_{RMS} and read out with optical interferometry. Figure 3.2 shows an SEM image of the device as well as representative resonance curves from one beam under different applied voltages. We find that both resonance amplitude and frequency are altered by an applied bias. In order to compare the frequency shift of several devices, we track their frequency as they are operated in a phase-locked loop (PLL). The frequency shift of a 4 μm long cantilever is included in the plot, showing that cantilevers are tuned about 100 times slower than beams. The PLL allows us to accurately track small changes in frequency in near real time without the need for taking resonance scans. Results are shown in Fig. 3.3 for the case of different beam alignment directions, length and bandstructure. The measured frequency shifts appear to be in excellent agreement with our predictions of linear voltage dependence, bidirectionality and piezoelectric crystalline anisotropy. We attribute the slight curvature of the data seen below -3 V in some devices to nonlinear $I(V)$ behavior that coincides with the onset of electrical breakdown, and also to the presence of weak electrostrictive effects, which were predicted to produce $\sim 10\%$ of the total tuning at -4 V. The next two sections discuss another possible mechanism, bias-dependent photoacoustic stress. The deviation in the slope of different devices is attributed to inadvertent beam misalignments or defects in the beam structure. Presently we do not understand the origin or exact role of these defects, but it appears likely that both electronic and mechanical defects would reduce piezoelectric stress. From the differences in slope seen throughout Fig. 3.3, it appears that this reduction can be as high as 30%. Given the angular dependence of both

piezoelectric and elastic constants, it is difficult to precisely determine the beam orientations, but by fitting the average slope (39 kHz/volt) from Fig. 3.3c to the $\Delta f(V)$ relation we deduce the highest value of d_{3j} to be 1.3 ± 0.1 pm/V, which is in very good agreement with the previously reported result⁵.

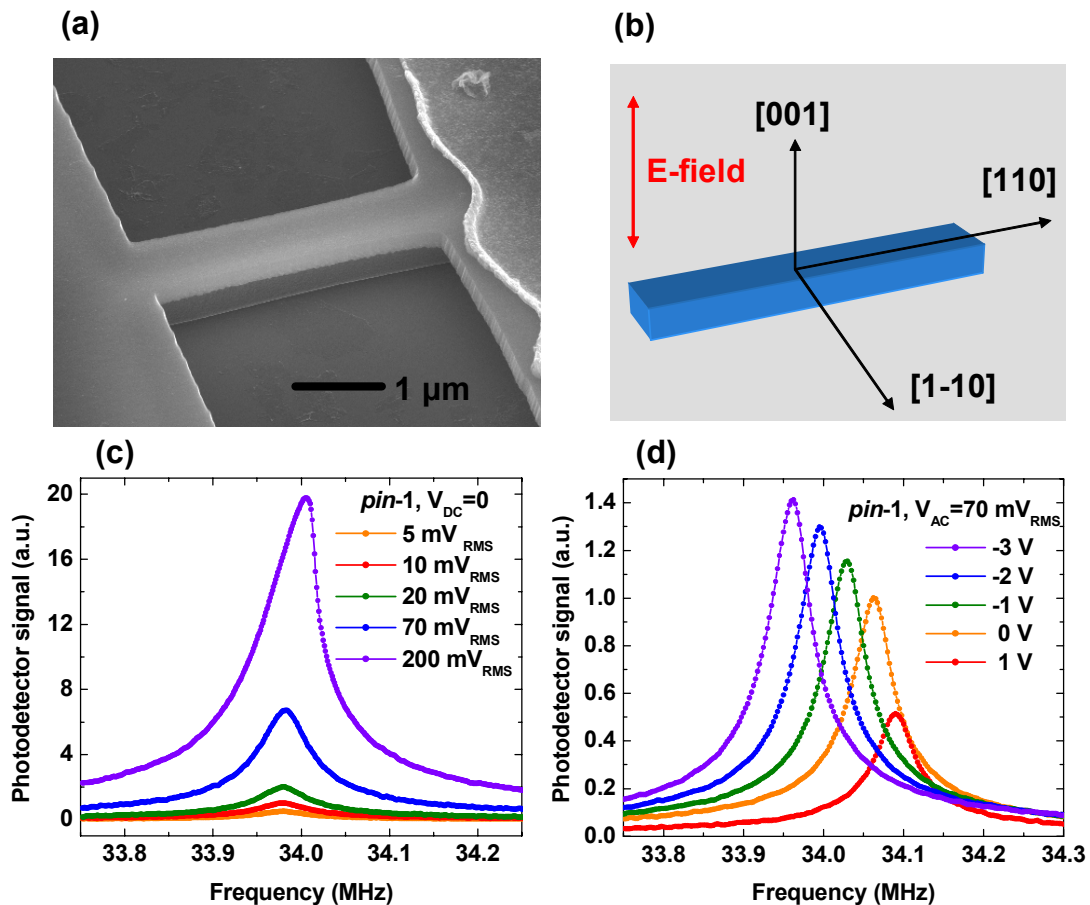


Figure 3.2 (a) SEM image of 4 μm long doubly clamped beam used to investigate piezoelectric frequency tuning phenomena, and (b) coordinate axes. Identical devices are fabricated from every *pin* diode and the *npn* structure. (c) Resonant response of the beam under different driving voltage and fixed dc bias. The quality factor is 700. The onset of nonlinear bistability occurs near a drive of 200 mV_{RMS}. (d) Resonant response of the beam under different dc voltage and fixed ac drive. The resonant frequency shifts up (down) for a positive (negative) bias, which is consistent with an axial tensile (compressive) force on the beam from piezoelectricity. Note that the resonance amplitudes also vary with dc bias, for the reasons outlined in Chapter 2.

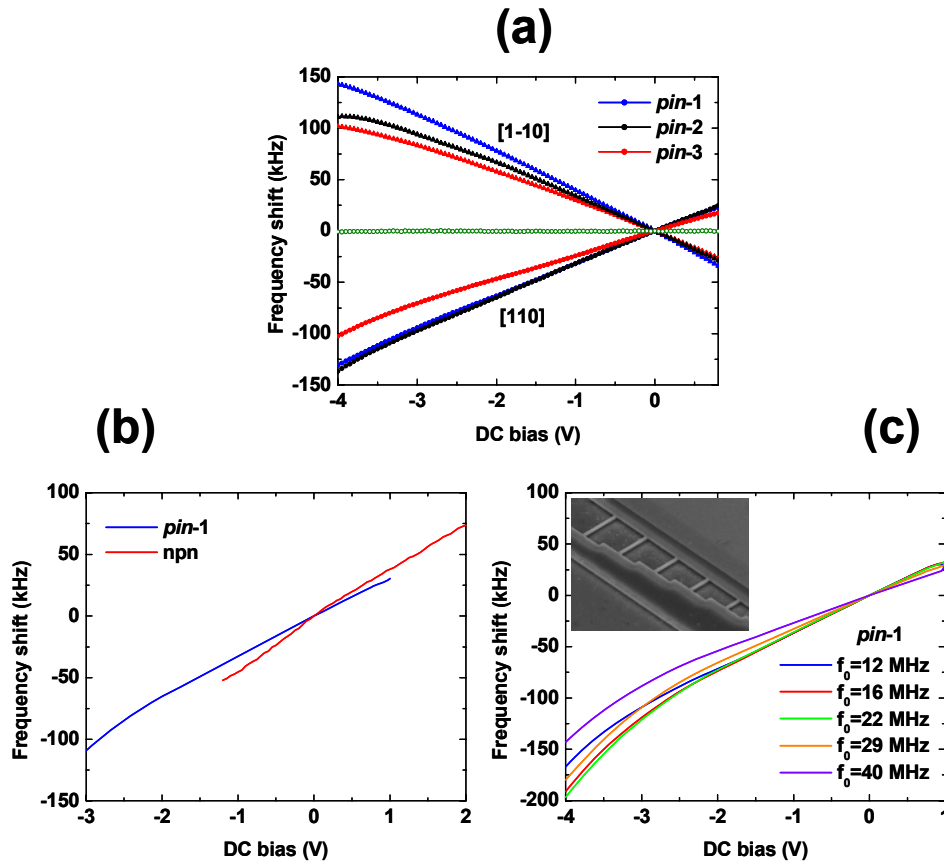


Figure 3.3 Resonance frequency of doubly clamped beams vs. dc bias, measured in a phase-locked loop. The beam structure is displayed in Fig. 3.2a. (a) All three *pin* diodes show similar tuning magnitudes and the direction of tuning is reversed by altering the beam alignment from [110] to [1-10]. The open green circles show the tuning of a 4 μm long cantilever – it is about 100 times weaker than a beam of the same dimensions. (b) The magnitude of tuning remains fairly constant in radically different bandstructure designs, such as *pin* and *npn* structures. All 4 μm long beams have resonance frequency around 34 MHz, so a 100 kHz shift corresponds to a fractional frequency change of 0.3%. (c) The magnitude of tuning is also virtually independent of the beam's length. The inset shows the guitar-like device with beam lengths from 7 to 3 μm corresponding to frequencies from 12 to 40 MHz.

In Fig. 3.4a we observe jumps in PLL tracking frequency corresponding to the addition of charge on the beam. The minimum resolvable change occurs with 2 mV dc bias, which is equivalent to around 100 electronic charges on the device. An interesting consequence of the linearity of piezoelectric frequency tuning is that there is a predictable 1:1 correspondence between each bias voltage and frequency value. This allows us to modify the conventional PLL

operation such that instead of tracking the phase by adjusting driving frequency, it adjusts the bias voltage. The modified PLL's scans are shown in Figure 3.4b. The advantage of operating in the voltage-controlled oscillator (VCO) mode is that a device can be powered with a fixed frequency, stable, high Q quartz crystal oscillator, and all information concerning changes in frequency would be directly translated to the electrical domain, thereby greatly simplifying the measurement protocol.

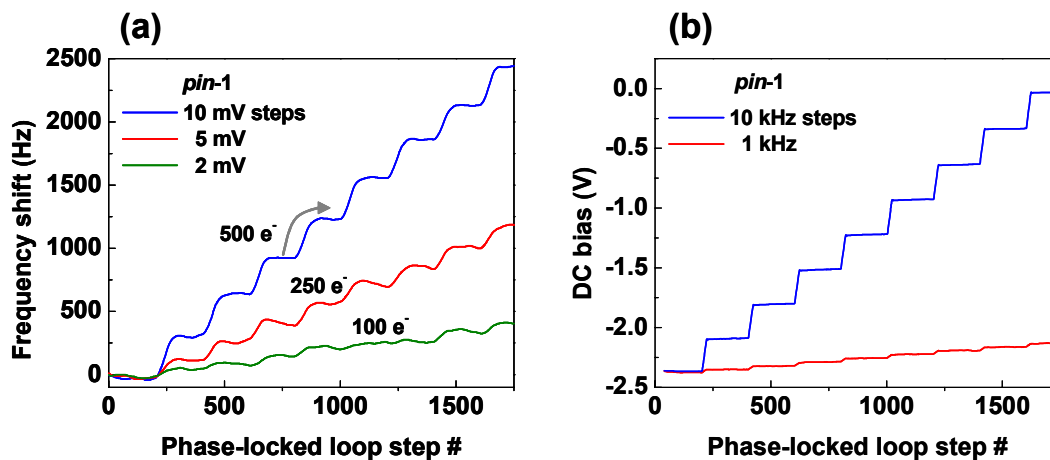


Figure 3.4 (a) Piezoelectrically induced frequency jumps of a $4 \times 0.8 \times 0.2 \mu\text{m}^3$ doubly clamped beam measured in a phase-locked loop. Each jump corresponds to the addition of 10 (blue), 5 (red) and 2 (green) mV of dc bias across the *pin* junction. The short-term stability of the loop is ± 15 Hz, whereas the long-term drift is ± 50 Hz and limits the ultimate charge sensitivity to ~ 100 electrons on the device. (b) Operation of phase-locked loop in the voltage-controlled mode, *i.e.*, the reference driving frequency, is fixed, and dc bias on the beam is the PLL's variable parameter. Each jump corresponds to the dc bias correction following a 10 kHz (blue) and 1 kHz (red) change in reference frequency.

3.5 Photoacoustic frequency tuning and voltage annealing effects

In this section we investigate all the possible contributions of light to resonance frequency shifts. We are aware of three types of photoacoustic processes: optical heating, photovoltaic-piezoelectric strain and electronic deformations. Heating alters frequency via thermal expansion and material stiffness changes. Using the linearized Timoshenko formula we predict that thermal

expansion will tune the frequency of a 200 nm thick GaAs beam by an amount $\Delta f_{th,\alpha} / \Delta T = -36 \text{ kHz/K}$, assuming a uniform heating distribution. An additional frequency shift of $\Delta f_{th,Y} / \Delta T = -2.2 \text{ kHz/K}$ is attributed to the temperature dependence of Young's modulus, thus the total $\Delta f / \Delta T$ is -38.2 kHz/K . A cantilever will experience much smaller frequency shifts, totaling about -0.4 kHz/K . From these values we can estimate the amount of light-induced heating by monitoring the frequency as a function of laser intensity, which is plotted in Figure 3.5. Under typical infrared illumination levels used in our measurements ($\sim 0.3 \text{ mW}$), the beam and cantilever are heated by 0.1 and 1.3 degrees, respectively. The difference in temperature can be at least partly attributed to the improved heat sinking characteristics of a doubly clamped structure, and may also be due to deviations in laser spot size that invariably occur while refocusing the light onto another device.

Photovoltaic effects have the ability to alter piezoelectric strain. However, in all our measurements the bias voltage is regulated with an external power supply, so this effect is not expected to play a role, except by providing an additional source of shot noise (see Chapter 4). The third mechanism, electronic deformation, is the least well understood. The isotropic strain due to excess carriers has been shown to be⁶ $e = (\Delta n / 3)(dE_g / dP)$, where Δn is the excess carrier density, and dE_g/dP is the pressure dependence of the band gap energy of GaAs², which is equal to $2 \times 10^{-23} \text{ cm}^3$. Assuming that the doping level ($\sim 10^{19} \text{ cm}^{-3}$) sets Δn_{max} , we obtain a maximum axial strain of 67 ppm, which is comparable to the largest piezoelectric strain that can be produced across the *pin* diodes. In practice such a large photogenerated carrier concentration is not expected, but nonetheless it is worth acknowledging that electronic deformation may cause some shift in resonance frequency.

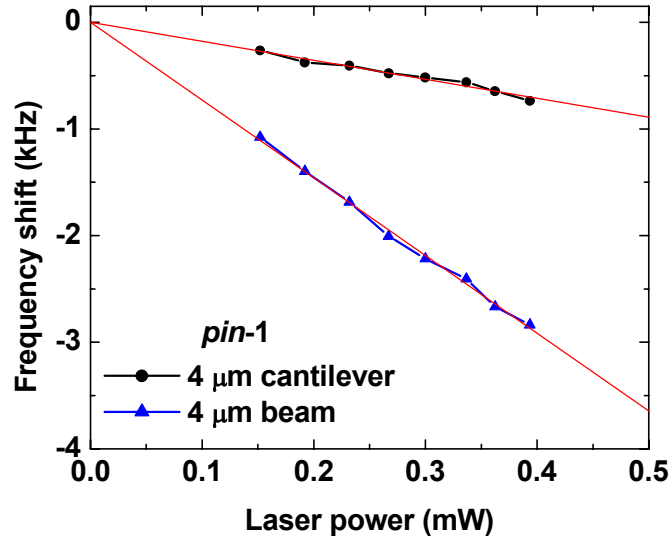


Figure 3.5 Frequency shift vs. laser power for a cantilever and beam made from diode *pin-1*. The shifts can be calibrated to the extrapolated value corresponding to no illumination, from which the amount of heating can be estimated. The results suggest that under typical illumination levels, devices are heated between 0.1 and 1.3 degrees. The difference could arise from changes in device geometry (*i.e.*, beam vs. cantilever) and deviations in laser beam spot size.

We now address the question of what causes the nonlinear bias dependence on frequency in some of the data in Figure 3.3. Recall that piezoelectric stress should give rise to a linear dependence. On the other hand, electrostriction is believed to produce nonlinear behavior, but a comparison of Figures 3.1b and 3.3c suggests it is not the secondary strain mechanism after piezoelectricity. During our measurements we have seen some evidence that a substantial time-varying shift arises in our device, which depends on both voltage and light intensity. This seems to imply that the nonlinearity is a result of a bias-dependent photoacoustic process. Figure 3.6 shows long PLL scans of the resonance frequency of a cantilever and beam under different dc bias and infrared illumination levels. The illumination was increased tenfold by removing a neutral density filter from the laser beam path, thus ruling out any possible laser diode intensity transients. Several qualitative changes in frequency are observed, namely: (i) a permanent downward time-dependent drift occurs starting near -3 V, (ii) the drift does not disappear following the removal of the reverse bias, (iii) the drift disappears after the diode is forward

biased before restoring it to zero bias, (iv) the drift leads to a permanent frequency shift and (v) both the drift and permanent shift increase markedly under higher reverse bias and illumination. It is worth emphasizing that the drift occurs over a much slower timescale than the PLL period, so it cannot be an artifact of the PLL. Heating also cannot be held responsible, as it would not lead to a substantial bias dependence of the drift rate. Having ruled out heating and photovoltaic-piezoelectric mechanisms, the only plausible remaining explanation for this bias-dependent photoacoustic behavior is electronic deformation. In the previous chapter it was proposed that the sacrificial $p\text{-Al}_{0.8}\text{Ga}_{0.2}\text{As}$ layer could modulation-dope the adjacent $p\text{-GaAs}$ layer that forms the lower “electrode” of the D-NEMS device. The modified doping level was found to produce a much better fit to the resonance amplitude dependence on dc voltage. However, it was suggested that the modulation doping effect is not constant, but rather may change slightly under different illumination and bias conditions. Since the valence and conduction band offset at the $\text{GaAs}/\text{Al}_{0.8}\text{Ga}_{0.2}\text{As}$ heterojunction exceeds kT/q by more than an order of magnitude, this charge transport mechanism may explain the very slow rate of resonance frequency drift. The permanent frequency shift may be a result of an optically assisted voltage annealing effect, which was hypothesized to lead to permanent charge transport in metal-oxide-metal tunnel junctions⁷. It should be noted that at present, no means of reversing the frequency shift following annealing has been found, suggesting that defect charges have been permanently removed from the D-NEMS devices. This effect may be a cause for concern in practical device applications where a high level of frequency stability and consistency is required. Nonetheless there are ways around this problem. First, it is an extremely slow effect so it may not influence certain applications. Second, the onset of constant frequency drift appears to occur at around -2 V, and devices could be restricted to operate below that value. Third, one could try to anneal out all defects by applying a large bias or raising the device temperature over a long period of time.

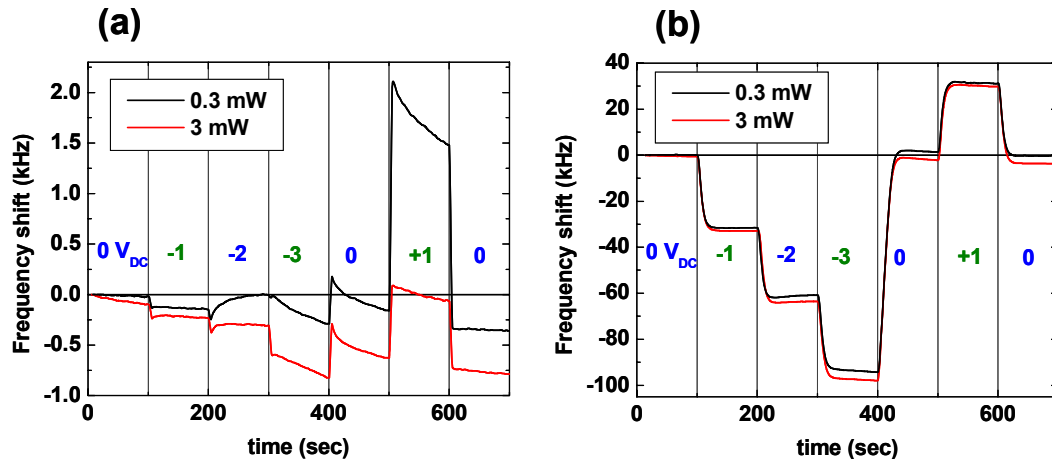


Figure 3.6 PLL scans of frequency shift vs. time under different applied dc voltages and laser intensity. The devices are a 4 μm long (a) cantilever and (b) beam fabricated from diode *pin-1*. The dc bias is altered every 100 s, and the PLL takes ≤ 10 s to lock onto the new frequency.

3.6 Uniformity of device quality factor and frequency

We have shown that the built-in piezoelectric effect in D-NEMS can be used to tune their resonance frequency with an applied voltage, thereby providing an additional level of control in our system. One of the potential uses of frequency tuning is to address the issue of inhomogeneity in large scale arrays. Despite numerous preventative measures, two devices that are designed to look and behave exactly the same invariably turn out to have different resonant frequency and quality factor. It has been suggested that an external frequency control mechanism could result in perfectly matched arrays. Here we test the feasibility of this approach using D-NEMS, by comparing the performance of several identical devices. We fabricate arrays of 3 μm long cantilevers and 5 μm long doubly clamped beams from diode *pin-1* and measure their response optically. The devices are aligned along both the [110] and [1-10] directions. The spatial separation of identically oriented devices is kept low (3 μm) to minimize any possible inhomogeneity in the as-grown wafer thickness. The results of measured quality factor and resonance frequency are plotted in Figure 3.7. The consistently lower frequency of devices along

[1-10] are believed to be due to the fact that the chemical undercut appears to etch ~10% faster along that direction. The standard deviation of resonance frequency is 1.4% for cantilevers and 1.8% for beams. Thus with some design improvement it may be just barely possible to correct for the frequency irregularities of beam arrays, but it will not be possible to use the same approach on cantilevers. The quality factors are even more spread out: 12% for cantilevers and 22% for beams, suggesting that at least one mechanical dissipation mechanism is highly sensitive to device imperfections created during epitaxial growth and/or fabrication. Ion beam etching appears to be the most damaging fabrication step and should particularly affect surfaces, which is consistent with other studies showing that surface dissipation is a dominant process in nanomechanical resonators^{8,9}. This defect-dominated picture of mechanical damping appears to corroborate the suggestion in Section 3.4 that randomly distributed defects have up to a 30% deleterious effect on piezoelectric frequency tuning. The same defects may also be responsible for the observed spread in natural frequencies. Thus, in the future it is certainly worth exploring the origin of defects and techniques to prevent them. For instance, it is hoped that replacing the Ar ion milling step with a less energetic ICP/RIE process will reduce electronic and perhaps also mechanical defects.

References

1. S. Timoshenko, D. H. Young, W. Weaver, *Vibration Problems in Engineering*, 4th ed., (John Wiley, 1974)
2. S. Adachi, GaAs, AlAs, and Al_xGa_{1-x}As: material parameters for use in research and device applications, *J. Appl. Phys.* **58**, 1 (1985)
3. B. Piekarski, D. Devoe, M. Dubey, R. Kaul, J. Conrad, Surface micromachined piezoelectric resonant beam filters. *Sens. Actuat. A* **91**, 313-320 (2001)
4. K. Fricke, Piezoelectric properties of GaAs for application in stress transducers. *J. Appl. Phys.* **70**, 914-918 (1991)
5. G. Arlt, & P. Quadflieg, Piezoelectricity in 3-V compounds with a phenomenological analysis of piezoelectric effect. *Phys. Status Solidi* **25**, 323 (1968)
6. R. G. Stearns & G. S. Kino, Effect of electronic strain on photoacoustic generation in silicon, *Appl. Phys. Lett.* **47**, 1048 (1985)
7. M. K. Konkin and J. G. Adler, Annealing effects in tunnel junctions (voltage annealing), *J. Appl. Phys.* **51**, 5450 (1980)
8. K. Y. Yasumura *et al.*, Quality factors in micron- and submicron thick cantilevers, *J. Microelectromech. Syst.* **9**, 117 (2000)
9. J. Yang, T. Ono, M. Esashi, Surface effects and high quality factors in ultrathin single-crystal silicon cantilevers, *Appl. Phys. Lett.* **77**, 3860 (2000)

Chapter 4

Noise processes in piezoelectric semiconductor NEMS

4.1 Thermomechanical noise spectrum

The purpose of this chapter is to review the noise processes that are most relevant to piezoelectric semiconductor NEMS. We also discuss the limitations set by the photodetector and accompanying laser. It shall be shown that despite some additional sources of noise, D-NEMS (and piezoelectric semiconductor NEMS in general) can offer excellent sensitivity, and that the biggest limitation in our setup is the optical detector's shot noise. This is by no means a comprehensive discussion of noise in NEMS, but rather a look at some subtle mechanisms that are particular to these types of devices. Our experimental setup has three possible sources of noise: first, the D-NEMS device undergoes electrical¹ and thermal fluctuations that couple to its mechanical behavior. Second, the laser diode and photodetector noise can reduce the ability to resolve displacements or frequency shifts. Third, the laser diode can also heat the NEMS or generate photocurrents that contribute to noise. The spectral sum of all these sources in the vicinity of an undriven resonance mode of a 4 μm long cantilever made from diode *pin-1* is shown in Figure 4.1. The optical detection scheme is sensitive enough to pick up the resonance with no external means of actuation. The measured voltage noise is $\delta V = 660 \text{ nV} / \sqrt{\text{Hz}}$ and $620 \text{ nV} / \sqrt{\text{Hz}}$ on and off resonance, respectively. From a crude calibration we estimate the photodetector signal γ corresponds to a cantilever deflection of $\approx 5 \mu\text{m} / \text{V}$. This value was obtained by measuring the peak output signal and Q at a drive of 10 mV_{RMS} and 0 V_{DC} and

calculating the amplitude with the multilayer actuation model developed in Chapter 2. The calibration parameter γ will of course depend on laser intensity and alignment; in this particular case we used high intensity (2.6 mW), with no neutral density filter. The photodetector signal translates to a displacement noise of $\delta z = \gamma \delta V$, which equals $3.2 \text{ pm}/\sqrt{\text{Hz}}$ on the resonance peak and $3.1 \text{ pm}/\sqrt{\text{Hz}}$ in the nearby background. The background-subtracted amplitude noise is therefore estimated to be

$$\delta z_{res} = 0.8 \text{ pm}/\sqrt{\text{Hz}} \quad (4.1)$$

This last value is attributed to intrinsic thermomechanical fluctuations of the cantilever, whereas the background is attributed to the photodetector. From the large relative background we infer that the detector is the largest source of noise in our system. Due to our uncertainty in calibrating γ , actual values may vary by up to a factor of two. The corresponding thermomechanical fluctuations on resonance are calculated to be²

$$\delta z_T = \sqrt{4k_B T B Q / k \omega_0} = 0.4 \text{ pm}/\sqrt{\text{Hz}} \quad (4.2)$$

which agrees with Eqn. 4.1 within the accuracy of our measurements.

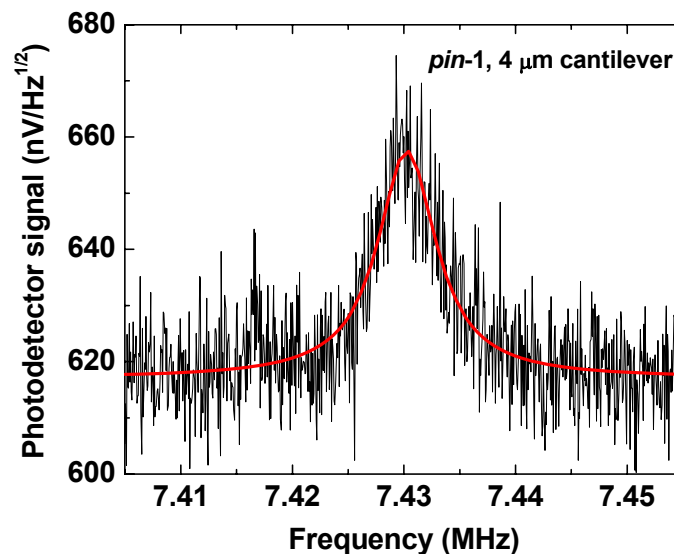


Figure 4.1 Thermomechanical noise spectrum of a $4 \mu\text{m}$ long cantilever fabricated from diode *pin-1* in the vicinity of its first mechanical resonance mode. The device has a quality factor of 1,200.

We can also convert the displacement noise into force noise using the spring constant of a cantilever, $k = Ywt^3 / 4L^3 = 2.9 \text{ N/m}$. This gives an experimental minimum resolvable resonant frequency force of $9.3 \text{ pN} / \sqrt{\text{Hz}}$. Note that we were not able to detect an undriven resonance in any doubly clamped beams, which are at least 50 times stiffer than the $4 \text{ }\mu\text{m}$ cantilever used here. We will now explore all the possible sources of noise.

4.2 Photodetector noise

The photodetector (PD) is a New Focus Instruments model 1801, with 125 MHz bandwidth and a wavelength range from 320 to 1000 nm. The manufacturer's specifications quote a peak conversion gain of 20 kV/W and a minimum noise equivalent power of $3.3 \text{ pW} / \sqrt{\text{Hz}}$, from which we can obtain a noise equivalent voltage of $66 \text{ nV} / \sqrt{\text{Hz}}$. In practice, the PD's shot noise significantly increases with light intensity, and we cannot rely on the optimal specified value. Figure 4.2 shows the measured voltage noise as a function of frequency for three IR laser diode power output levels. The light is first reflected off the sample and passes through a beam splitter. Thus only about 5% of the power radiated from the laser reaches the detector. There is good agreement between the manufacturer's noise specifications and the measured noise under no illumination, while the noise sharply increases with laser brightness. The measurements shown in Fig. 4.1 are carried out at the maximum light intensity level; in contrast recall that previous measurements included a 10X neutral density filter, *i.e.*, only $\sim 0.05\%$ of the radiated light reached the detector. As expected, the PD noise in the frequency range of our cantilever is $\sim 600 \text{ nV} / \sqrt{\text{Hz}}$. Attempts to reduce noise by reducing the laser brightness resulted in a further deteriorated signal to noise ratio (SNR). However, there is a trade-off between better SNR and reduced photoacoustic effects. In Chapters 2 and 3 we tried to minimize photoacoustic effects and voltage annealing by using the neutral density filter, but here the preference is a better SNR.

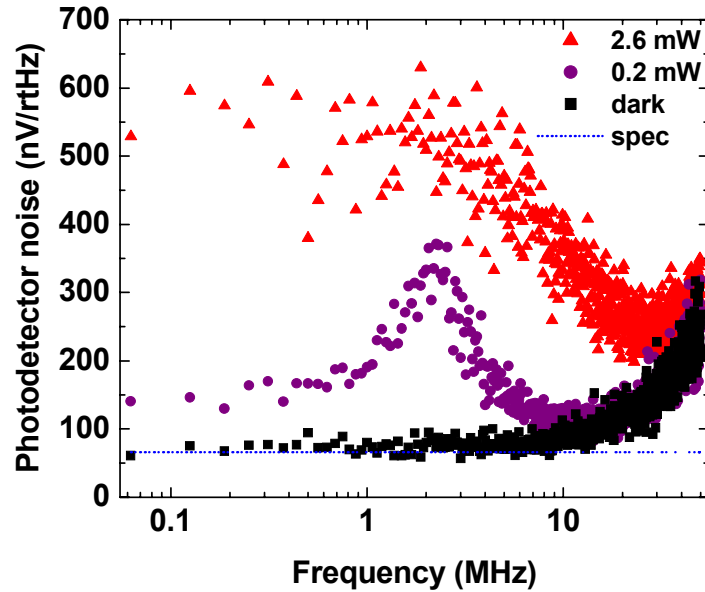


Figure 4.2 Wide band scan of the photodetector noise spectrum under different levels of IR laser illumination. The dashed line indicates the manufacturer's specified noise level.

4.3 Laser diode shot noise

Fluctuations in laser intensity can either directly translate to extra noise at the detector, or perturb the NEMS resonator through photoacoustic strain. A large source of fluctuations in most solid state devices is shot noise, whose root-mean-square value is given by $\delta I_{LD} = \sqrt{2qBI_{LD}}$, where q is the electronic charge, B is the measurement bandwidth and I_{LD} is the current. With $I_{LD}=45$ mA, δI_{LD} is calculated to be $120 \text{ pA}/\sqrt{\text{Hz}}$. The dc output voltage of the photodetector is around 3.3 V, so laser diode (LD) shot noise should translate to a PD signal of $\delta V_{LD \rightarrow PD} \approx 3.3 \delta I_{LD} / I_{LD} = 8.8 \text{ nV}/\sqrt{\text{Hz}}$, which is about 70 times lower than the PD's internal fluctuations and can thus be neglected. On the other hand, photoacoustic effects have the potential to increase noise in the mechanical resonator.

4.4 Electromechanical noise

In nonpiezoelectric devices operating under optimal conditions, thermomechanical fluctuations set their ultimate sensitivity. But when dealing with piezoelectrics one must also contend with electromechanical contributions to noise. In particular D-NEMS, like other piezoelectric devices¹, should have a piezoelectric-electromechanical coupling to Johnson and shot noise. The infrared laser was intentionally used in order to minimize photogenerated current (which leads to shot noise) by operating below the band gap of GaAs, but in practice shallow impurities always lead to some current. The laser produces a current that is measured to be about 1 μA , which gives rise to an rms shot noise of $\delta I_s = \sqrt{2qBI} = 0.57 \text{ pA}/\sqrt{\text{Hz}}$. In addition, the Johnson noise is given by $\delta V_J = \sqrt{4k_B TBR_d} = 0.7 \text{ } \mu\text{V}/\sqrt{\text{Hz}}$, where we have used $R_d = 30 \text{ M}\Omega$ as the diode resistance. It is evident that the electromechanical coupling in D-NEMS places additional restrictions on their ultimate sensitivity (see next section) compared to nonpiezoelectric devices, particularly if the Johnson noise is large. For instance it could wreak havoc in experiments aimed at observing quantum mechanical phenomena in NEMS^{3,4}. In such cases it may be necessary to avoid piezoelectric materials altogether, but in less extreme experiments there may be some simple ways to curb electromechanical noise while retaining the useful features of piezoelectrics. First, one might reduce the temperature, although this would not always be a practical solution. Second, the D-NEMS could be engineered to deflect very little mechanically with voltage by placing the active layer close to the neutral axis of strain. Third, given the highly nonlinear I(V) behavior of diodes it may be possible to bias the diode partially into its low resistance regime. This would attenuate both Johnson noise and driving efficiency; however, the shot noise would increase exponentially so an intermediate optimal bias point would have to be established.

4.5 Frequency stability of D-NEMS

So far in this chapter we have discussed noise in the context of displacement sensitivity, which is useful in force detection applications. However, resonance frequency stability is typically a more useful quantity for mass or charge detection. Figure 4.3 shows phase-locked loop scans of two devices, measured via infrared optical read-out. To minimize photoacoustic effects we used a neutral density filter (10x attenuation) and a laser bias current of 35 mA. The diode *pin-1* was biased with 0 DCV and 10 mV_{RMS} for the cantilever; 70 mV_{RMS} for the beam. The standard deviation of frequency measured from the figure is ± 5 Hz for the cantilever and ± 56 Hz for the beam. The corresponding Allan deviations with a 0.1 second PLL time constant are found to be 3.7×10^{-9} and 1.8×10^{-8} for the cantilever and beam, respectively. Numerous PLL trials confirmed the consistency of the above results, which were all carried out at room temperature and 10 mTorr pressure. The corresponding mass loading sensitivity can be determined from the expression $\delta m = 2m_{\text{eff}} \delta f / f_0$, where m_{eff} is equal to 0.74 or 0.24 times the total mass for a beam or cantilever, respectively. This gives values of 1.2×10^{-18} g (1.2 attogram) for the cantilever and 9.3 attogram for the beam, although we do not claim to have directly observed mass loading. One would expect that, if internal stresses were the primary cause of frequency fluctuations, then cantilevers would be ~ 100 times more stable in frequency than beams. Since this is not borne out by measurement we deduce that photodetector phase noise rather than device-intrinsic behavior is responsible for most of the observed frequency fluctuations. To check this hypothesis we estimate the contribution of electromechanical noise to δf . The shot noise, which does not affect rf displacements, should influence stresses that are measured on the scale of the PLL cycling rate. The shot noise voltage with a 30 M Ω resistor is $\delta V_s = 17.1 \mu\text{V}/\sqrt{\text{Hz}}$, while the Johnson noise was estimated to be $0.7 \mu\text{V}/\sqrt{\text{Hz}}$ in the previous section. The primary source of electromechanical frequency fluctuations is piezoelectric stress, whose frequency-voltage

dependence (~ 39 kHz/volt) was obtained in Chapter 3. The total electromechanical frequency fluctuations are predicted to be equal to $(39 \text{ kHz/V})\sqrt{B}\sqrt{\delta V_s^2 + \delta V_j^2} = 0.7 \text{ Hz}/\sqrt{\text{Hz}}$ and $0.007 \text{ Hz}/\sqrt{\text{Hz}}$ for the beam and cantilever, respectively. Clearly if stability is a requirement, cantilevers are better candidates; if stress-dependent tunability is desired, then beams must be used despite their increased noise. These fluctuations account for only a small fraction of the total measured noise, which appears to arise in the photodetector. This limitation suggests there is still some scope for improving the frequency stability of these devices, particularly cantilevers, which appear to have the potential for zeptogram (10^{-21} g) scale mass sensitivity⁵. Another possibility is that minute temperature fluctuations on the devices may vary over time due to movement of the optical components or random blocking of light by dust particles. A variation of just 1 mK on the beam would account for most of the observed frequency fluctuations.

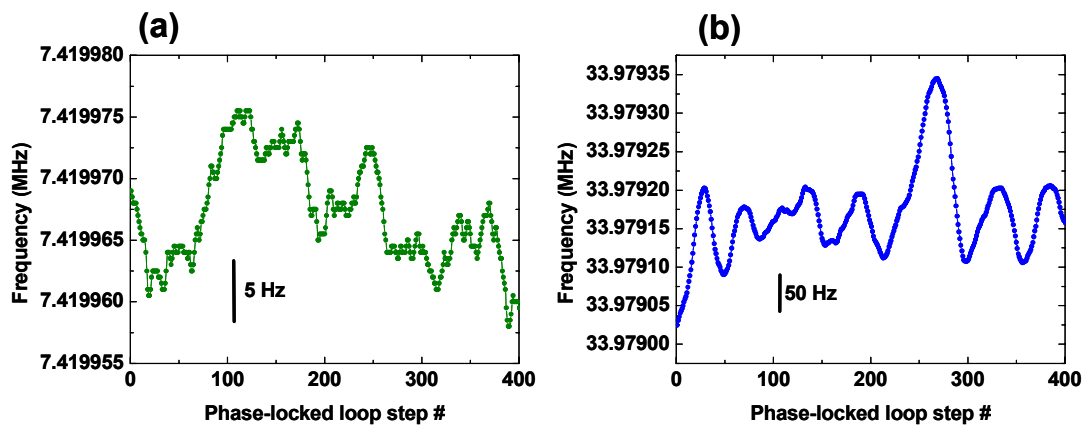


Figure 4.3 Phase-locked loop scan. (a) $4 \mu\text{m}$ long cantilever made from diode *pin-1*; $V_{\text{DC}}=0$, $V_{\text{AC}}=10 \text{ mV}_{\text{RMS}}$; $Q=1,200$. (b) $4 \mu\text{m}$ long doubly clamped beam made from diode *pin-1*; $V_{\text{DC}}=0$, $V_{\text{AC}}=70 \text{ mV}_{\text{RMS}}$; $Q=700$. Each time step is 0.1 seconds.

4.6 Summary of Noise Processes

Piezoelectric semiconductors have additional sources of noise because of their intrinsic electromechanical coupling. This could potentially reduce the ultimate sensitivity of D-NEMS relative to thermomechanically limited devices, but careful design should ameliorate electromechanical coupling effects. It has become apparent that the most limiting factor to better sensitivity in our current setup is photodetector shot noise. Given higher-quality lenses we could readily improve sensitivity by an order of magnitude by focusing more of the light on the NEMS device, thereby pushing up the SNR. For more drastic improvements we could use lower noise photodetectors. Eventually, it would be beneficial to switch to all-electrical transduction of D-NEMS, and in this regard it has been shown by others that piezoelectric-based detection offers excellent sensitivity⁶⁻⁸, although overcoming the size problem remains a challenge.

References

1. T. Itoh & T. Suga, Minimum detectable force gradients of piezoelectric microcantilevers, *J. Micromech. Microeng.* **5**, 231 (1995)
2. A. N. Cleland & M. L. Roukes, Noise processes in nanomechanical resonators, *J. Appl. Phys.* **92**, 2758 (2002)
3. M. D. LaHaye, O. Buu, B. Camarota, K. C. Schwab, Approaching the quantum limit of a nanomechanical resonator, *Science* **304**, 74 (2004)
4. R. G. Knobel & A. N. Cleland, Nanometre-scale displacement sensing using a single electron transistor, *Nature* **424**, 291 (2003)
5. Y. T. Yang, C. Callegari, X. L. Feng, K. L. Ekinici, M. L. Roukes, Zeptogram-scale nanomechanical mass sensing, *Nano Letters* (2006)
6. R. G. Beck, M. A. Eriksson, R. M. Westervelt, K. L. Campman, A. C. Gossard, Strain-sensing cryogenic field-effect transistor for integrated detection in GaAs/AlGaAs microelectromechanical systems, *Appl. Phys. Lett.* **68**, 3763 (1996)
7. Y. Zhang & M. P. Blencowe, Sensitivity of a piezoelectric micromechanical displacement detector based on the radio-frequency single-electron transistor, *J. Appl. Phys.* **92**, 7550 (2002)
8. R. Knobel & A. N. Cleland, Piezoelectric displacement sensing with a single electron transistor, *Appl. Phys. Lett.* **81**, 2258 (2002)

Chapter 5

Novel D-NEMS architectures

5.1 Introduction

D-NEMS present a promising solution to the long-standing problem of integrated nanomechanical actuation. After characterizing the basic operating principles of actuation and frequency tuning of piezoelectric semiconductors, the next step is figuring out what to do with this unprecedented level of mechanical control of nanostructures. In this chapter we discuss a few of the D-NEMS concepts to have come out of the lab, and their potential role in practical applications. We end with an overview of alternative materials to GaAs for improved electrical and mechanical performance, and an analysis of how much further semiconductor NEMS can be miniaturized before running into serious problems.

5.2 Parametric amplification

In Chapter 3 it was shown that a transverse voltage tunes the resonance frequency of a doubly clamped beam. Up to now the frequency was tuned slowly with respect to the timescale of the resonators, but in principle the process can be sped up, since piezoelectric stress can be modulated at extremely fast rates. A special case, known as parametric amplification, corresponds to modulating frequency at twice the rate of resonant vibration. The result is a pumping of additional energy into the resonator, which can either increase or decrease its effective quality factor depending on the signal phase. Mechanical parametric amplification was demonstrated by Rugar and Grütter¹, who used electrostatic interactions to tune the resonance of

a micromechanical cantilever. Recently Michael Roukes' group has extended this work to radio-frequency NEMS devices, using Lorentz forces to tune the resonance². However, both electrostatic and magnetomotive techniques have substantial limitations. Electrostatic tuning usually requires either small gap sizes, which are difficult to consistently fabricate, or large biases on the order of tens of volts. Magnetomotive methods require large magnetic fields which usually involve superconducting solenoids, thereby precluding room temperature operation. In addition the magnetomotive frequency tuning mechanism is current-dependent, so it is prone to heating effects. On the other hand, the piezoelectric frequency tuning method is not susceptible to current-heating, works at room temperature and requires only a few volts to operate. These features have motivated us to implement parametric amplification with D-NEMS.

We study parametric amplification in doubly clamped beams made from diode *pin-1*, having lengths between 3 and 3 μm . Their measured widths are 0.6 μm ; wide enough to provide a reasonably high SNR with optical detection. The devices are connected in a parallel, guitar-like configuration shown in Figure 5.1a. All devices are actuated simultaneously, but we can select which beam to resonate and observe by appropriately tuning the laser beam position and signal bandwidth. The beams are resonantly excited and monitored with a network analyzer. The junction is biased with a parametric pumping signal of 1 to 2 V_{RMS} at a fixed frequency corresponding to $2f_{\text{res}}$. A reverse dc bias of -1.3 V is added in order to avoid the low diode resistance regime. Figure 5.1b plots the response of the 3 μm beam with the parametric pumping signal on or off, in room temperature and vacuum. By turning on the pumping effect the effective quality factor is amplified 37 times, from 1,800 to 66,500. Moreover, Figure 5.1c demonstrates that this technique can be extended to ambient pressure, where aerodynamic drag typically reduces Q to the low 100's. With sufficient parametric pumping, we have shown gains exceeding 20 in air in the 8 μm long beam. If the pumping amplitude is further increased we run into two possible issues. First, the beam is driven into self-oscillation and we can no longer treat it as a resonator. Second, the voltage enters the diode's nonlinear $I(V)$ regime and makes the device

prone to heating. The largest voltage that can be safely applied is about $\pm 3 V_{\text{RMS}}$ with a dc bias of -1.3 V. Parametric amplifier NEMS may give rise to better frequency resolution in mass and force sensors. Their high quality factor also makes them excellent candidates for extremely narrow width bandpass filters. Finally, we anticipate this effect will eventually play a role in mediating interactions between coupled nanomechanical devices, or enabling synchronization of NEMS oscillators³.

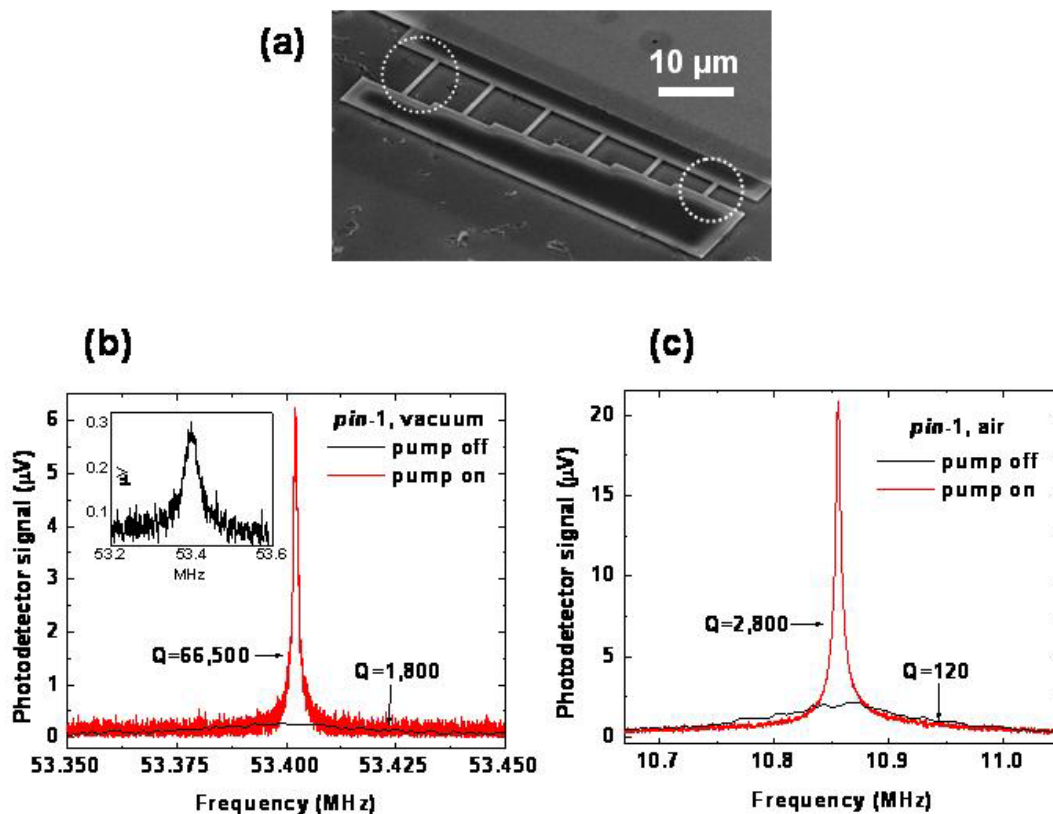


Figure 5.1 (a) SEM image of guitar NEMS array fabricated from diode *pin-1*. The lengths range from 3 to 8 μm and fundamental frequencies from 53 to 11 MHz. Detection is carried out optically. The shortest and longest devices are used to demonstrate parametric nanomechanical amplification in vacuum (b) and air (c), respectively. The parametric gain is 37 in vacuum and 23 in air. The RMS driving/pumping amplitudes, $V(f_0)$ and $V(2f_0)$, are 50 mV drive/500 mV pump in vacuum and 50 mV drive/3 V pump in air.

5.3 Balanced charge detection

The piezoelectric crystalline anisotropy has no analog in electrostatics, so it may be possible to devise new applications with it. One idea, combining charge sensing with piezo-crystalline anisotropy, is the balanced charge detection scheme. An electron microscope image of the prototype device is shown in Figure 5.2a. The two 7 μm long beams were designed to be orthogonal to each other, such that their piezoelectric constants have equal magnitude but opposite sign. This will impact their operation in two important ways: First, an applied bias will tune the frequency of one device up as it tunes the other device the same amount down. This allows us to tune two devices toward each other. Second, based on our understanding of D-NEMS actuation we predict that the devices will always move out of phase with each other if their driving signals are synchronized. We now measure the mechanical response of the two beams as a function of applied voltage. The close proximity of the beams allows us to observe them simultaneously with optical interferometry. Careful adjustments were made to the optical alignment to closely match their peak resonance amplitudes. In the future one could alternatively employ piezoresistive read-out techniques.

The magnitude and real component of the photodetector signal is shown in Figures 5.2b, c under different biasing conditions. The data confirm that the resonance frequencies can be tuned toward each other, and from Figure 5.2b it is evident that the beams move out of phase. It is important to emphasize that all the actuation and tuning is occurring via a single shared contact electrode. As expected, the total magnitude decreases as the peaks merge, reaching a minimum at a forward bias of about 0.1 V. Our goal was to see the peaks disappear completely, but only achieved about 90% cancellation. In the ideal case both devices would have the same quality factor and their detected response would exactly cancel. In that scenario the resonators would effectively be in a locked state, and the only parameter that could pull them out of that state would be charge. For instance, any temperature fluctuations experienced by both devices would

lead to a frequency shift down, but their resonances would remain locked. On the other hand, the addition of charge would break the symmetry and appear as a nonzero signal. The devices would still be subject to uncorrelated noise processes between the two beams, but any correlated fluctuations, *e.g.*, drift in temperature or pressure, would be effectively removed. Even if this scheme does not prove useful in charge detection, it may lead toward other devices that harness the unique mechanical coupling provided by piezoelectric crystalline anisotropy.

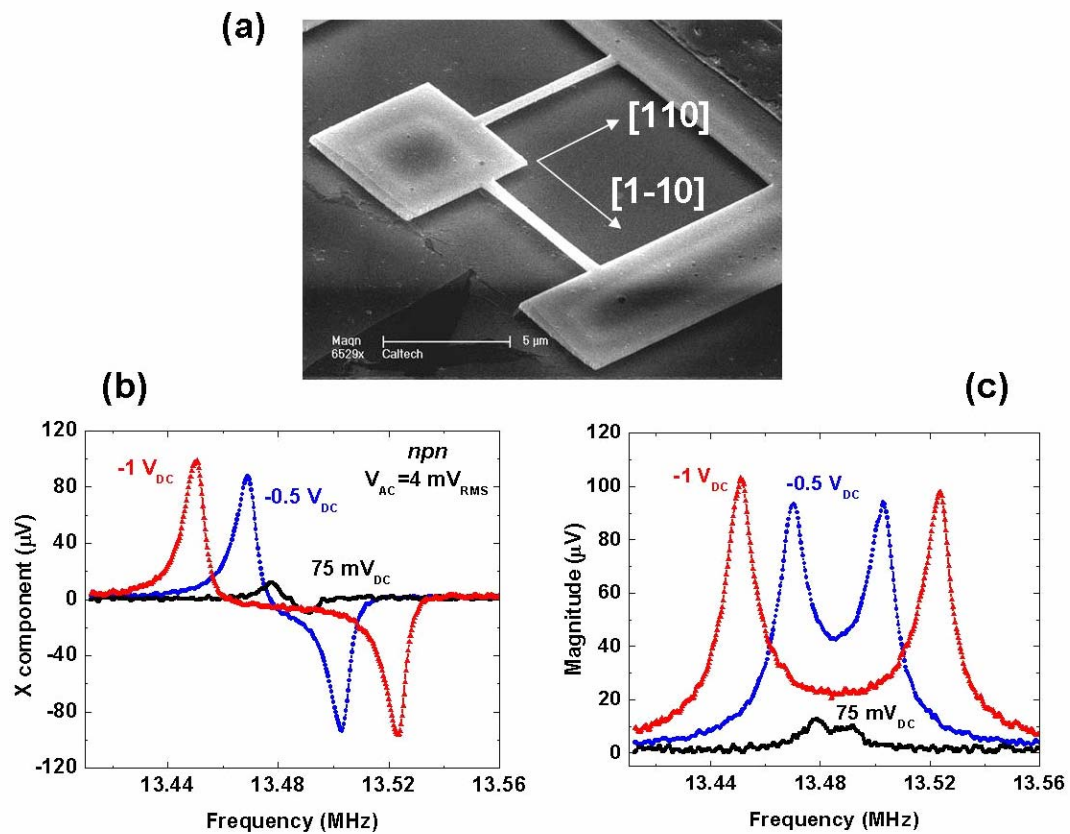


Figure 5.2 (a) Prototype device for demonstrating balanced charge detection using orthogonal doubly clamped beams. The device was fabricated from the *npn* structure used in Chapter 2. (b) Real component and (c) magnitude of optical response of the two 7 μm long beams under different applied dc bias voltages. The resonant vibrations are antisymmetric because of the anisotropy of d_{3j} . Their frequencies be made to converge or diverge depending on the sign of the applied bias voltage. The signal nearly cancels when the frequencies are matched.

5.4 Prospects for measuring quantized piezoelectric strain

In Chapter 3 it was found that the smallest resonance frequency shift that can be resolved on a $4 \times 0.8 \times 0.2 \text{ }\mu\text{m}^3$ doubly clamped piezoelectric beam corresponds to just over 100 electronic charges. With sufficient reduction of noise, it may be possible to access the regime of single-electron sensing. This would not only have obvious benefits for charge detection, but would also provide insight into the microscopic picture of piezoelectricity. The bulk piezoelectric constants quantify the dependence of polarization on strain; however, it is not clear if this macroscopic description can be extended to the case of small occupation numbers where the charge wavefunctions are not distributed uniformly across the device. This leads me to propose a new nanomechanical experiment aimed at measuring quantized piezoelectric strain. Though such measurements have not been carried out, they appear feasible in principle and this section outlines some important experimental design considerations. An experiment of this kind would present several challenges, including devising a means of gating single charges onto a resonator. This could be achieved with a single-electron transistor operating at mK temperatures in a dilution refrigerator. That much has already been achieved in the search of quantized nanomechanical displacement⁴. Another challenge would be transducing the device. For instance, the use of optical interferometry would be prohibited to prevent heating and shot noise, so we would have to rely on piezoresistive, piezoelectric, or capacitive techniques. Piezoresistive measurements are susceptible to heating and are therefore probably not a good option, while both piezoelectric and capacitive methods involve charge exchange, so care would be needed to prevent back-action from the detector to the resonator, which would perturb its frequency. The actuation mechanism must not involve charge transfer. It will be essential to be able to count the absolute number of electrons on the device, perhaps by employing quantum dot coupling techniques similar to those used by Peta *et al.*⁵ The heterostructure would probably need to be optimized for 2DEG operation, so that the electric field can be confined to a precisely specified

geometry. The device should be made as thin as possible in order to maximize the coupling between piezoelectric strain and frequency. If all these hurdles could be overcome then the actual measurements would consist of monitoring the resonance frequency as a function of charge. Changing the occupation number by 1 should appear as a jump corresponding to the quantized piezoelectric strain. We could then ask whether the step size remains constant as the limit $n \rightarrow 1$ is approached. If the electrons are confined within the beam as particles in a box, then their wavefunction's nonuniform spatial distribution may lead to a nonuniform frequency step size.

5.5 Nanomechanical mode-shape engineering

The balanced charge detection scheme investigated earlier made use of the piezoelectric crystalline anisotropy to produce antisymmetrically vibrating beams. Another exciting prospect is to combine this motional asymmetry onto a single nanomechanical device. This scheme is referred to as mode-shape engineering because in principle it should be possible to control which resonance modes to excite. The basic concept is demonstrated with the 8 μm wide cross-beam structure shown in Figure 5.3. The first few modes of this device without including any piezoelectric effects were obtained from finite element simulations and are illustrated as insets on the left side of the figure. For comparison, the right side of the figure shows the corresponding mode for a simple doubly clamped beam of the same length. The fundamental mode involves the entire structure moving vertically in phase, but piezoelectric anisotropy should strongly oppose this mode from being exciting. Besides actuating this device via the internal piezoelectric effect, we also shake it using a PZT crystal mounted underneath the GaAs chip. Since the capacitance of the PZT crystal is similar to that across the *pin* junction, we can directly compare the driving efficiency of the two schemes. It was found that in contrast to all other observed modes, the first cross-beam could be actuated with comparable efficiency by internal and external means. This suggests the fundamental mode is indeed suppressed during internal piezoelectric excitation.

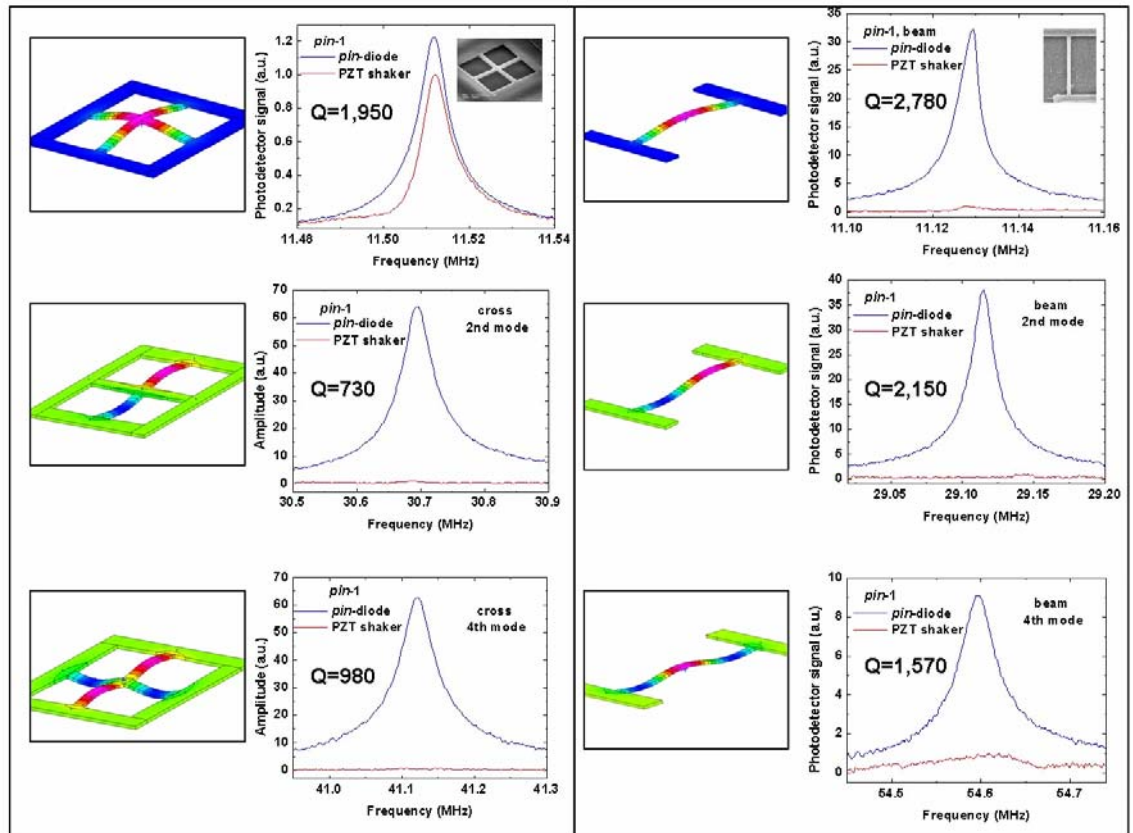


Figure 5.3 Demonstration of mode suppression in a cross-beam resonator fabricated from diode *pin-1*. The renderings are from finite-element simulations of the 1st, 2nd and 4th mode shapes. Resonance curves represent the response to an internal piezoelectric (blue curves) or external PZT shaking (red curves) actuation mechanism. The left set of data are from the 8 μm cross-beam and the right set from a simple beam of the same length. Due to piezo-crystalline anisotropy, the first cross-beam mode should be suppressed by internal excitation. The actuation of the 1st cross-beam mode is excited nearly as efficiently by the PZT shaker as by internal means (top left). In contrast, internal excitation of the 1st beam mode is 30 times more efficient than by external means (top right). A comparison of the top left and right curves suggests that the 1st cross mode is suppressed by a factor of ~ 30 .

Improvements in device symmetry could lead to even stronger mode-shape suppression. In contrast to the 1st mode, the 2nd, 3rd (not shown but similar to 2nd) and 4th cross modes are excited ~ 70 times more efficiently by internal piezoelectric means rather than by shaking. This further suggests that the internal piezoelectric actuation mechanisms can efficiently access higher order modes that are otherwise challenging to activate. Also note that the quality factor of higher

order modes usually decreases more slowly than the corresponding increase in frequency, suggesting that higher order modes may be well suited to mass sensing applications. Mode suppression represents a unique level of control that does not appear possible with other actuation mechanisms.

Mode-shape engineering opens up entirely new opportunities for studying NEMS, and a number of applications could arise from this effort. One potential application is in nanoelectromechanical logic devices. The first computing machine as envisioned by Charles Babbage⁶ was based not on semiconductor electronics, but steam-powered mechanical contraptions. Babbage's "difference engine" never worked and today there is little incentive to replace silicon logic. On the other hand, signs that the miniaturization of silicon CMOS devices will reach a limit sometime in the next few decades have once again led to bold thinking about alternative computing paradigms. Are NEMS the answer to our future computing needs? Probably not, but it's conceivable that they will occupy a niche in the nanotechnology market. Eventually it may become important to carry out simple computations to coordinate the operation of large scale NEMS arrays. Moreover, it may be more efficient to conduct the computation in the electromechanical domain without transducing the information back and forth from the electrical to the mechanical domain multiple times. Figure 5.4 illustrates how piezoelectric NEMS devices might operate as logic gates, together with their predicted truth table. If two identical signals are applied to the inputs shown in blue, the output shown in red will remain stationary and register as a "0". But if a signal is applied to only one input, the output will move and register as "1" or "-1" depending on the phase relationship. Note that, owing to piezoelectric anisotropy, there are three possible input and output states, where we have assigned 0° phase a value of "1" and 180° phase a value of "-1". Another way of thinking about this is that "1" is up, "-1" is down and "0" is flat. A more practical application exploiting this technology could be differential mechanical amplifiers, which may improve NEMS sensor performance.

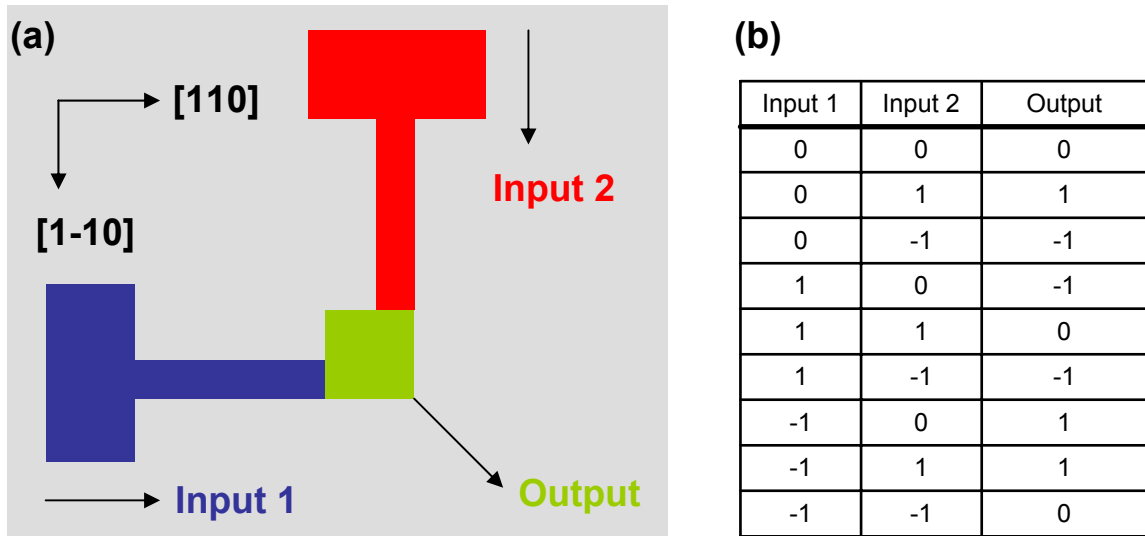


Figure 5.4 (a) Schematic illustration of the nanomechanical logic gate concept employing the piezoelectric anisotropy property of GaAs and other crystals. (b) Expected truth table for such a device. Zeros correspond to no signal; 1's are symmetric oscillations and -1's are antisymmetric. If the input signals are both 0 or ± 1 , then the output will not register any motion.

5.6 Alternative piezoelectric materials for NEMS

Table 5.1 lists the piezoelectric constants of some materials that either already are or could be used in nanomechanical systems. One particularly promising semiconductor is AlN, which is stiffer, less dense, and has stronger piezoelectric coupling than GaAs⁷. SiC is another compound semiconductor that has comparably favorable mechanical properties⁸, except its piezoelectric constants are ~ 3 times weaker than GaAs. Apart from their superior mechanical performance, these materials have a higher band gap than GaAs and thus offer correspondingly higher electrical breakdown fields. They are also chemically inert and thus do not pose any cytotoxicity issues. While it is possible to grow submicron films of monocrystalline AlN and SiC with MBE or metal-organic chemical vapor deposition (MOCVD), the reliable growth of selectively doped layers is not yet possible. Thus we cannot presently grow *pin* or similar D-NEMS structures with such materials. The choice of a good lattice-matched sacrificial layer and substrate also remains a

challenge⁹, with Si (111) a likely candidate^{10,11}. There is an ongoing research effort into improving the growth capabilities for these materials¹². Besides single compounds, it may be beneficial to use SiC-AlN heterostructures¹³. Highly doped SiC would make excellent semiconductor electrodes, while insulating AlN can form the middle piezoelectric layer. Another possibility is using Al_{0.7}Ga_{0.3}N, as the electrodes, and undoped AlN as the middle layer. Al_{0.7}Ga_{0.3}N has poorer mechanical and piezoelectric properties than AlN or SiC, but it can be selectively doped to some extent¹⁴.

Material <i>reference</i>	Piezoelectric constant (pm/V)
Si	0
SiC (6H) <i>Karmann</i>	0.36 (d_{33})
AlN <i>Bernardini</i>	-5.86 (d_{31}) 3.98 (d_{33})
GaP <i>Adachi</i>	-0.71 (d_{31})
GaAs <i>Adachi</i>	-1.34 (d_{31})

Table 5.1 Piezoelectric constants of some semiconductors. Refs: 15 – 17.

5.7 Ultimate scaling limits of semiconductor NEMS

There are a number of benefits to shrinking the dimensions of NEMS devices. Smaller devices provide greater mass and force responsivity, and thinner piezoelectric beams have better charge sensitivity and should have less internal dissipation¹⁸. All the D-NEMS devices presented up to now have been 200 nm thick, between 0.6 and 0.8 μm wide, and 3 to 8 μm long. The structures that offer the most scope for miniaturization in the vertical direction are simple *pn* diodes or metal-semiconductor contacts, commonly known as Schottky contacts. It should be possible to piezoelectrically actuate both of these structures as well as tune their resonance frequency, as long as their depletion widths do not approach within a few nm of their total thickness. In this

section we estimate how thin and narrow semiconductor structures can be made before encountering fundamental size limitations from carrier depletion effects. Such a situation is illustrated in Figure 5.5a, which depicts the bandstructure of a 50 nm thick pn junction under two different biasing conditions. At sufficient reverse bias, the diode is fully depleted and would not be able to operate properly. In Figure 5.5b we identify two regions where depletion takes place; in the interior at the junction, and at surfaces.

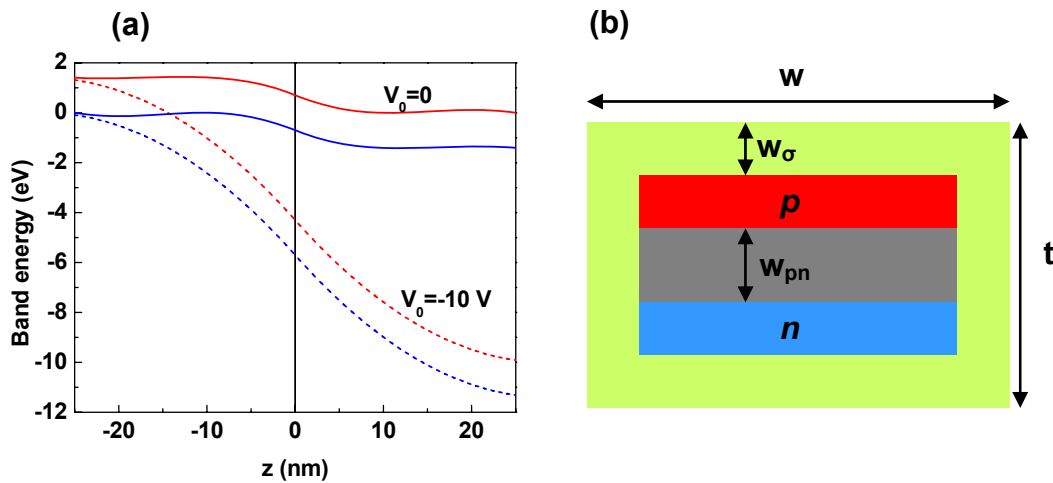


Figure 5.5 (a) Band energy diagram of a 50 nm thick GaAs pn junction with 10^{19} cm^{-3} doping on each side. The solid lines correspond to zero applied bias, and the dashed lines correspond to -10 V applied bias. In the latter case the band bending is not complete, *i.e.*, the diode is fully depleted, rendering it inoperable. Surface depletion is ignored, though it can significantly contribute to band bending. (b) Schematic of pn junction cross-section depicting surface depletion (pale green) and junction depletion (gray). In order for the device to function properly, its total thickness and width must be greater than the size of the depletion regions.

In the abrupt junction approximation the depletion width of a pn junction and Schottky contact are, respectively¹⁹:

$$\begin{aligned} w_{pn} &= \sqrt{2\epsilon_d N_{tot} (V_{bi} - V) / (eN_A N_D)} \\ w_{ms} &= \sqrt{2\epsilon_d (V_{bi} - V) / (eN_S)} \end{aligned} \quad (5.1)$$

From these expressions it is evident that high p and n doping levels are required to provide narrow widths. The maximum allowed doping concentration in GaAs is around 10^{19} cm^{-3} , but we

would probably need to use around 100 times fewer dopants in the Schottky barrier to avoid forming an Ohmic contact, thus pn junctions are preferred for nanodevice applications. The built-in potential V_{bi} is close to the material band gap for large doping concentrations. The pn junction depletion width for a highly doped diode is plotted in Figure 5.6 for different semiconductor materials. While silicon offers the most scope for miniaturization, it is not piezoelectric. Figure 5.6 assumes only internal depletion, but carriers will also be depleted at all the surfaces (including the sides of the device). GaAs is particularly susceptible to this problem because of the vast number of dangling bonds formed after surface reconstruction. While it is difficult to precisely predict the surface charge concentration, we can reasonably assume it is sufficient to keep the Fermi level pinned at mid-gap, *i.e.*, $V_{bi}(\text{surface})=V_g/2$. The corresponding surface depletion width is

$$w_\sigma = \sqrt{\epsilon_d V_g / e N_s} \quad (5.2)$$

Since Fermi level pinning can affect all surfaces, the minimum dimensions of a D-NEMS device are given by

$$\begin{aligned} \text{thickness} &\gtrsim (w_{pn} + 2w_\sigma) \\ \text{width} &\gtrsim 2w_\sigma \\ \text{length} &\gtrsim w_\sigma \end{aligned} \quad (5.3)$$

For a suspended GaAs pn junction with $E_g=1.4$ eV and $N_A=N_D=10^{19}$ cm⁻³, the minimum thickness and width are estimated to be 40 and 20 nm, respectively. In practice these values should be increased to allow some room for biasing the diode with an externally applied voltage. Note that the greater built-in potential of higher band gap semiconductors such as SiC or AlN will place tighter restrictions on their dimensions, although it may be possible to circumvent this problem by doping at higher concentrations²⁰. Moreover, the amount of surface depletion in these materials may be less than that of GaAs.

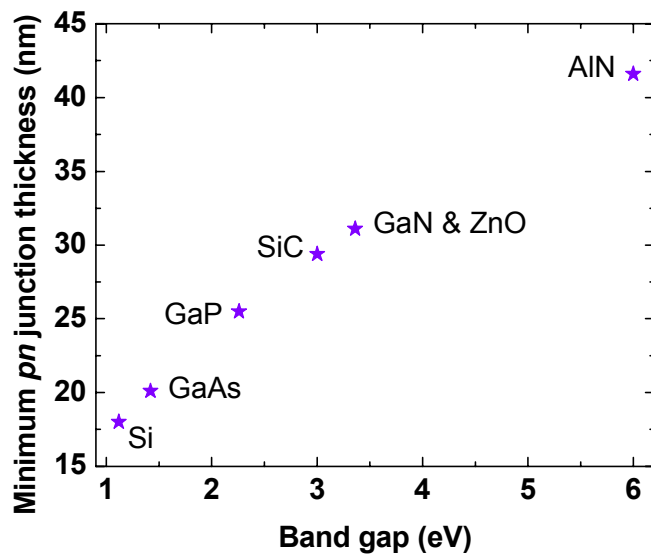


Figure 5.6 Minimum thickness, given by w_{pn} of pn junctions fabricated from different materials under zero applied bias. This figure of merit provides a measure of the smallest allowed thickness of semiconductor diodes made from different materials. We assume no surface depletion and a doping level of 10^{19} cm^{-3} on both sides of the junction. Higher band gap materials are more difficult to scale down and may require greater doping concentrations to be applicable to piezoelectric D-NEMS devices. Note the presence of surface depletion can increase the minimum dimensions by a factor of 2 or more. Further revisions are needed in order to allow a substantial bias to be applied to the junction. Thus a factor of three should be applied to the above results to get a useful device thickness.

References

1. D. Rugar & P. Grütter, Mechanical parametric amplification and thermomechanical noise squeezing. *Phys. Rev. Lett.* **67**, 699 (1991)
2. R. Karabalin, X. L. Feng, and M. L. Roukes, unpublished results
3. M. C. Cross *et al.*, Synchronization by nonlinear frequency pulling, *Phys. Rev. Lett.* **93**, 224101 (2004)
4. M. D. LaHaye, O. Buu, B. Camarota, K. C. Schwab, Approaching the quantum limit of a nanomechanical resonator, *Science* **304**, 74 (2004)
5. J. R. Petta *et al.*, Coherent manipulation of coupled electron spins in semiconductor quantum dots, *Science* **309**, 2180 (2005)
6. D. D. Swade, The construction of Charles Babbage's difference engine no. 2, *IEEE Annals of the history of computing* **5**, 70 (2005)
7. A. N. Cleland, M. Pophristic, I. Ferguson, Single-crystal aluminum nitride nanomechanical resonators. *Appl. Phys. Lett.* **79**, 2070-2072 (2001)
8. Y. T. Yang *et al.*, Monocrystalline SiC nanoelectromechanical systems, *Appl. Phys. Lett.* **78**, 162 (2001)
9. L. Liu & J. H. Edgar, Substrates for gallium nitride epitaxy, *Mat. Sci. & Engineering* **R37**, 61 (2002)
10. E. Calleja *et al.*, MBE growth and doping of III-nitrides on Si(111): layer morphology and doping efficiency, *Mat. Sci. & Engineering* **B82**, 2 (2001)
11. P. Kung *et al.*, High quality AlN and GaN epilayers grown on (001) sapphire, (100) and (111) Si substrates, *Appl. Phys. Lett.* **66**, 2958 (1995)
12. O. Ambacher, Growth and applications of III-nitrides. *J. Phys. D: Appl. Phys.* **31**, 2653-2710 (1998)
13. J. Choi *et al.*, Bandstructure and alignment of the AlN/SiC heterostructure, *Appl. Phys. Lett.* **86**, 192101 (2005)
14. B. Yang *et al.*, 32x32 Ultraviolet Al_{0.1}Ga_{0.9}N/GaN pin photodetector array, *IEEE J. Quantum Elect.* **36**, 1229 (2000)
15. S. Karmann, R. Helbig, R. A. Stein, Piezoelectric properties and elastic constant of 4H and 6H SiC at temperatures 4-320 K, *J. Appl. Phys.* **66**, 3922 (1989)
16. F. Bernardini, V. Fiorentini, D. Vanderbilt, Spontaneous polarization and piezoelectric constants of III-V nitrides, *Phys. Rev. B.* **56** R10024 (1997)

17. S. Adachi, GaAs, AlAs, and $\text{Al}_x\text{Ga}_{1-x}\text{As}$: material parameters for use in research and device applications, *J. Appl. Phys.* **58**, 1 (1985)
18. K. Y. Yasumura *et al.*, Quality factors in micron- and submicron thick cantilevers, *J. Microelectromech. Syst.* **9**, 117 (2000)
19. S. M. Sze, *Physics of Semiconductor Devices*, 2nd ed., (John Wiley, 1981)
20. M. Hermann *et al.*, Highly Si-doped AlN grown by plasma-assisted MBE, *Appl. Phys. Lett.* **86** 192108 (2005)

Chapter 6

All-electrical transduction with D-NEMS

6.1 Motivation for all-electrical electromechanical transduction

All our measurements up till now have relied on optical interferometry, which has proven to be a very powerful tool. However, it suffers one major setback: It is difficult to integrate all the parts of the interferometer on a chip-scale device. Although there has been significant progress in microlens fabrication, and while laser diodes and photodiodes are now routinely coupled to electromechanical systems^{1,2}, electrical transduction remains the detection mode of choice for most NEMS devices. We greatly benefited from the uncoupled nature of piezoelectric actuation and optical detection; this has allowed us to rapidly investigate new types of tunable electromechanical coupling in piezoelectric semiconductors (Chapter 2), mechanical resonance frequency tuning (Chapter 3), thermomechanical noise-limited motion (Chapter 4) and unconventional device geometries (Chapter 5). Some of those experiments would either have been severely obfuscated by implementing an all-electrical transduction scheme, or at least delayed because of the additional wiring that would be required. That is why we have been using optical interferometry all this time, but we recognize that if they are to succeed, D-NEMS must prove they can be fully electrical machines. Besides the aforementioned problem of integration, optics require a light source, which requires abundant current – and that goes against the mantra of NEMS as being highly efficient devices. In this chapter I discuss the progress we have made with piezoresistive and piezoelectric measurements on D-NEMS resonators. The actuation mechanism is piezoelectric as always. For convenience we only perform measurements on the

diode *pin*-1. Our initial findings demonstrate that electrical detection is quite feasible, but the SNR is severely limited by the large capacitance of the contact electrodes and vacuum chamber feed-through wires.

6.2 Piezoresistive detection

Piezoresistive sensing is demonstrated with the device displayed in Figure 6.1. Processing is carried out with the usual sequence of steps plus a few additional steps: First the legs on the left and cantilever on the right are defined with a mask. We then ion mill the top conducting layer. Next we carefully align the connecting beam support, place a second mask layer, and perform another ion milling step. Finally the entire device is released from the sacrificial AlGaAs. The top layer of the legs has a two-terminal resistance of $R_0=1.2 \text{ k}\Omega$. We piezoelectrically excite the device by driving the right side with an rf signal. For detection we employ the piezoresistive heterodyne frequency downconversion (a.k.a. downmixing) scheme developed by Bargatin, Myers *et al.*³ in Michael Roukes' group. A schematic of the measurement circuit is given in Figure 6.2. The main advantage of this technique is that the signal we want to measure from the resonator is mixed down to low kHz range frequencies, which significantly reduces losses from parasitic capacitances. This is particularly useful in devices such as ours, which have substantial capacitances that short out currents at MHz range frequencies, so that without downmixing we cannot measure any signal. The piezoresistive response around the first resonance mode is plotted in Figure 6.1b. There is a substantial background signal, which could be reduced by modifying the setup into a bridge circuit.

We can estimate how much strain is being detected on resonance using the gauge factor of *n*-GaAs which has been found to be⁴ $GF = \Delta R / (e_x R_0) \approx -4$. The biasing current is $30 \mu\text{A}_{\text{p-p}}$ and from the data we find the unamplified piezoresistive voltage signal to be $\sim 3 \mu\text{V}_{\text{p-p}}$. This gives $\Delta R = \pm 0.1 \Omega$, corresponding to a net longitudinal strain of $\pm 21 \text{ ppm}$ in the legs of the device.

We have also tested a number of other piezoresistive devices that are actuated piezoelectrically. As a proof of concept we further showed that parametric amplification⁵, which was discussed in Chapter 5, is possible in this hybrid piezoresistive/piezoelectric device. Figure 6.3 shows the characteristic gain in amplitude in quality factor that occurs with the onset of parametric amplification. The measurement was carried out by applying an ω drive signal and $2\omega_0$ pump signal to the right arm of the device, and an $\omega+\delta\omega$ bias signal to the left arm.

Piezoresistive detection appears to be a robust way of measuring rf NEMS displacements, but in certain cases, such as when the goal of the experiment is to explore a new actuation scheme, it is beneficial to use nonelectrical sensing techniques, such as optical interferometry. Moreover, the downmixing scheme can cause unwanted ac electromechanical coupling, so it may hamper our understanding of other coupling phenomena such the phenomena discussed in Chapter 2. Finally, piezoresistive measurements are inherently dissipative – this produces heat, which may have an adverse effect on the experiment, *e.g.*, by thermally stressing the device.

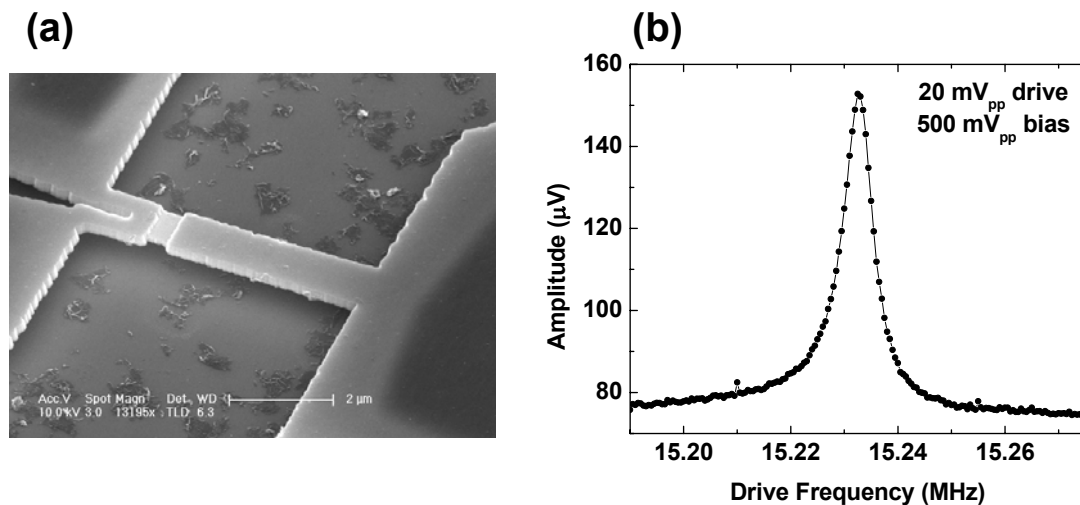


Figure 6.1 (a) SEM image of beam designed for piezoelectric actuation (right side)/ piezoresistive detection (left side; legs). The diode *pin-1* is used. The resistance of the legs is 1.2 k Ω . The top conducting layer of the diode has been removed in the middle of the beam to electrically isolate the actuator from the detector; in practice significant cross-talk is observed. Scale bar is 2 μm . (b) Measured piezoresistive signal of device using the heterodyne downconversion (a.k.a. downmixing) scheme. The signal amplification factor is 100. The sample is in vacuum (10 mTorr).

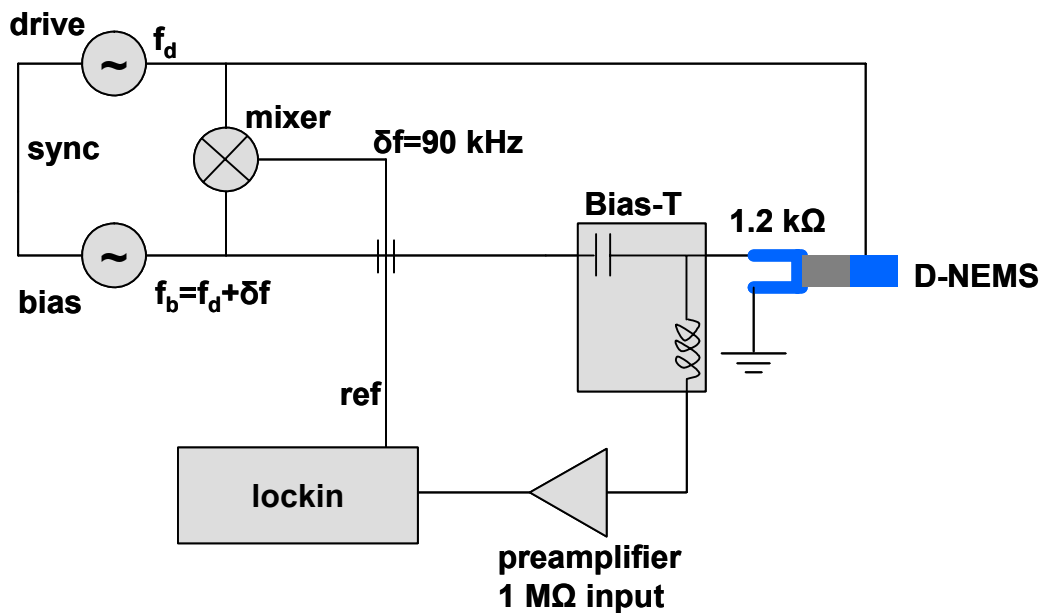


Figure 6.2 Setup for piezoresistive sensing of D-NEMS using the frequency downconversion technique [Bargatin *et al.*, ref. 3].

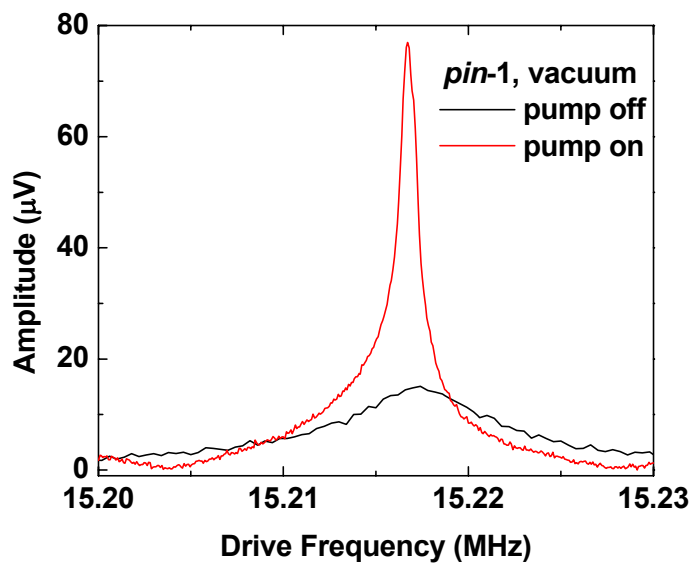


Figure 6.3 Piezoresistive response of the device in Fig. 6.1a in the parametrically amplified mode.

6.3 Piezoelectric detection – theory

The reversible nature of the piezoelectric effect raises the possibility of performing the entire transduction sequence in the piezoelectric domain. This offers a number of advantages over piezoresistive sensing: very low dissipation, fewer electrical feed-throughs, and the prospect for parallel large scale array operation. On the other hand, we will see that the largest impediment to using this effect for sensing is measuring the tiny currents produced by vibrating nanoscale mechanical structures, which are shorted by huge capacitances. Piezoresistive and optical detection suffer less from size effects, because the weak vibrational energy is effectively coupled on-site to an external, amplifying energy source (*e.g.*, current or light).

We now discuss the application of piezoelectricity to displacement sensing. Intuitively, sensing is related to actuation, which was explored in Chapter 2. However, a common misconception is there is a single constitutive equation describing both sensing and actuation, given by Eqn. 2.2:

$$e_j = d_{3j}E_3 = d_{3j}V / t_{piezo} \quad (6.1)$$

Taken at face value, this expression suggests that not only can one calculate strain from applied electric field, but by taking the reciprocal relation one can find the voltage generated by an applied strain. But the above formula is only valid for the former effect (strain due to an E-field). If it also described that latter effect, one would expect 100% electromechanical coupling efficiency, and the bizarre result that the generated voltage increases asymptotically as the piezoelectric constant goes to zero. This picture is clearly wrong, and I only bring it up because one occasionally finds this error in peer-reviewed publications. The missing element that resolves this apparent contradiction is that there are two piezoelectric constitutive equations, which basically state the following: electric field causes strain, and time-varying strain produces current. The polarization current density is given by

$$j_z = c_{11}d_{31}\partial e_x / \partial t \quad (6.2)$$

The amount of voltage produced by the current depends on the circuit's impedance. Figure 6.4 depicts the D-NEMS diode's equivalent circuit in sensing mode. A piezoelectric current source is shorted by the capacitance of the device, electrode and feed-through cables, diode resistance and the motional impedance components. As shown in Chapter 2, R_d and the motional components are much larger than the impedance from C_{tot} and can safely be ignored. Hence the circuit reduces to a low-pass filter with a time constant set by $R_{cont}C_{tot}$. Using a value for C_{tot} of 100 pF (typical) and contact resistance of 50 Ω we find the cutoff frequency to be $f_c \approx 30$ MHz, which is quite low but not prohibitively so for measuring our cantilevers. This result underscores the need for making good Ohmic contacts to piezoelectric semiconductors and minimizing all sources of stray capacitance. Assuming operation well below the cutoff frequency, the voltage referred to an input with impedance R_0 is $V_{PZL} \approx I_{PZL} |R_0 Z_C / (R_0 + Z_C)|$, where Z_C is the impedance of C_{tot} . Here we benefit by using a high input impedance preamplifier. If $R_0 \gg Z_C$ we can further approximate the voltage as

$$V_{PZL} \approx I_{PZL} |Z_C| \quad (6.3)$$

This expression tends to overestimate V_{PZL} , and for a rigorous treatment the full circuit impedance model should be used. The most important barrier to achieving good SNR with piezoelectric detection in NEMS is stray capacitance.

To check the validity of this model let us use it to calculate the voltage produced by a well-known piezoelectric transducer, a commercial $f=10$ MHz quartz crystal, which is known to have excellent SNR. This device operates on the bulk mode of resonance⁶. The electrodes have an area of 0.3 cm² or 10 million times more than our typical D-NEMS, and the quartz thickness is 150 μm or 3,000 times greater than our device. The piezoelectric constant of quartz⁷ is $d_{11} \sim 0.6$ pm/V, and we estimate from the measured Q (10,000) of the crystal that a 1 mV_{p-p} resonant

driving signal generates a strain of $0.04\cos(\omega t)$ ppm, corresponding to a current of $6 \mu\text{A}_{\text{p-p}}$ as calculated from a slightly modified version of Eqn. 6.2. The measured capacitance of the electrodes plus cables is 50 pF, so using Eqn. 6.3 the detected piezoelectric voltage should be $\approx 2 \text{ mV}_{\text{p-p}}$, which is a little higher than the measured value of $0.6 \text{ mV}_{\text{p-p}}$. If the quartz crystal were reduced to the area and thickness of typical D-NEMS, we would expect a much smaller signal of about $200 \text{ nV}_{\text{p-p}}$ for the same driving amplitude.

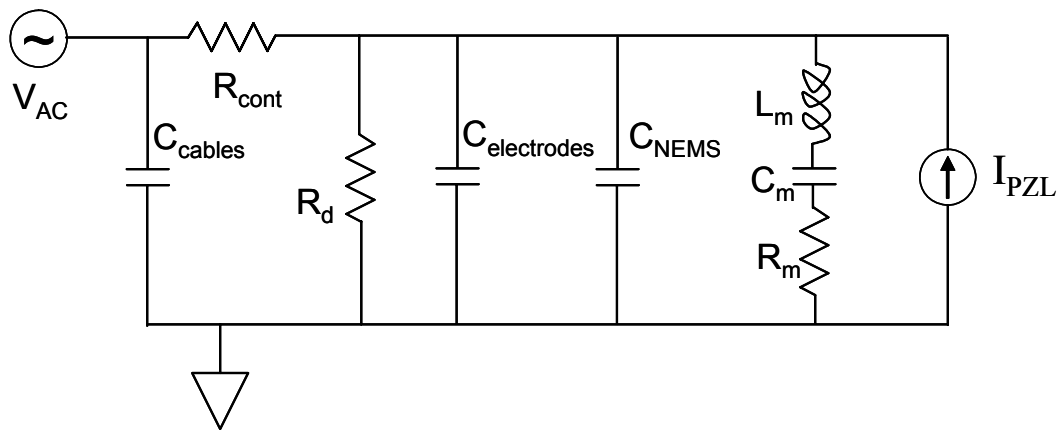


Figure 6.4 Equivalent circuit of D-NEMS with a source of strain-induced current.

6.4 Piezoelectric detection – experiment

To ameliorate the effect of signal cross-talk we employ a balanced bridge circuit for the piezoelectric sensing experiment. Figure 6.5 shows the measurement circuit. Each branch of the bridge is connected to an identically fabricated set of cantilevers and beams from diode *pin-1* as shown in the inset. Note only the $4 \mu\text{m}$ long cantilever (second from the left) is recorded from, and it has the same dimensions as the devices discussed in Chapters 2 and 4. Both sets of devices in the bridge belong to the same chip and hence share a ground, making it convenient to implement a transmission mode measurement. The bridge provides about 30 dB attenuation of the background signal; further reduction could be achieved by replacing one arm of the bridge

with tunable components, but the simple setup used here was adequate. The generated voltage was amplified by a 1 M Ω input impedance preamplifier with a gain of 40 dB before being acquired on a network analyzer with a bandwidth of 10 Hz. Scans were averaged 256 times prior to being recorded. A Matlab algorithm combining amplitude and phase information was used to subtract the remaining background signal. The resulting scans are plotted in Figure 6.6. For convenience we only recorded from one device, but a second peak corresponding to the 4 μ m long cantilever from the other arm was found at 9 MHz. The linear dependence on drive amplitude and onset of nonlinear behavior clearly demonstrates the mechanical origin of the peak, which was confirmed by optical interferometry.

A useful quantity to know is the electromechanical coupling efficiency k_{PZL} , which is the ratio of energy pumped in during actuation to the electrical energy extracted out. The magnitude of in- and out-bound charges is just $Q_{in} = C_{NEMS} V_{AC}$ and $Q_{out} \approx C_{tot} V_{PZL}$, giving

$$k_{PZL} \approx \frac{V_{PZL}^2 C_{tot}}{V_{AC}^2 C_{NEMS}} \quad (6.4)$$

This expression tends to overestimate the efficiency because it ignores some impedance sources depicted in Figure 6.4. Using the data in Figure 6.6 we calculate a coupling efficiency of only about 0.0005 %, taking $C_{tot}=120$ pF and $C_{NEMS}=6$ fF. The small magnitude of this value is due to the large total capacitance relative to the NEMS capacitance (recall that $V_{PZL} \sim 1/C_{tot}$). The ideal optimized electromechanical energy conversion efficiency of this D-NEMS device is obtained by recalculating V_{PZL} assuming $C_{tot}=C_{NEMS}$, giving $k_{PZL} \leq 0.8$ %. This last estimate is about a factor two greater than the theoretical maximum coupling constant⁸, so we have reasonably good agreement. We expect the transduction efficiency to vary strongly from one piezoelectric structure to another, just like we saw with actuation in Chapter 2. A nearly 1% energy conversion efficiency is excellent for virtually any transducer application; it is comparable to the

performance of quartz crystal resonators. A further useful quantity is the charge transduction efficiency Q_{out}/Q_{in} . Under optimal conditions this is 9%.

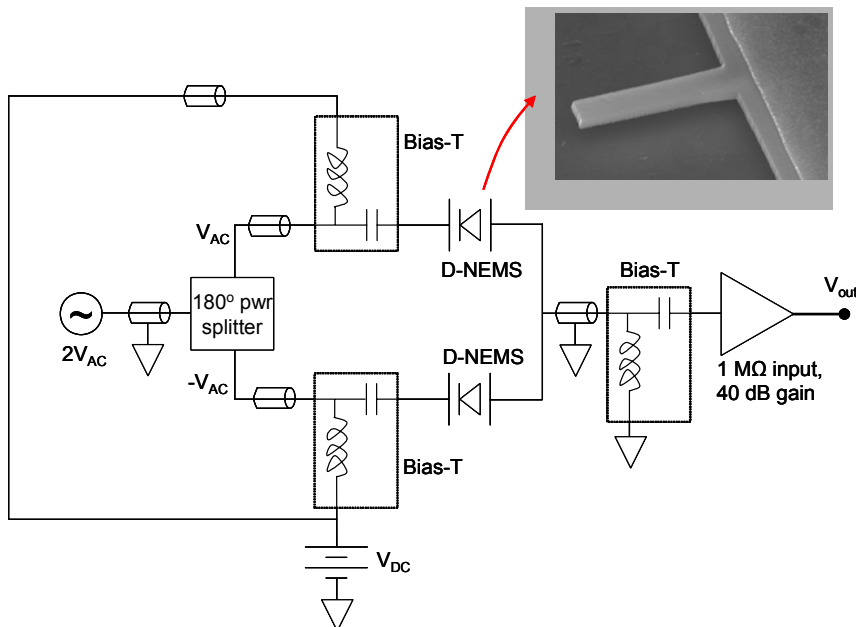


Figure 6.5 Balanced bridge setup for measuring piezoelectric response of D-NEMS. All cables are shielded to ground. The bias-T's are used to combine ac and dc voltages. The inset shows one of the devices fabricated from diode *pin-1* (same device used in Chapter 2). Actual measurements were performed on an identically fabricated cantilever.

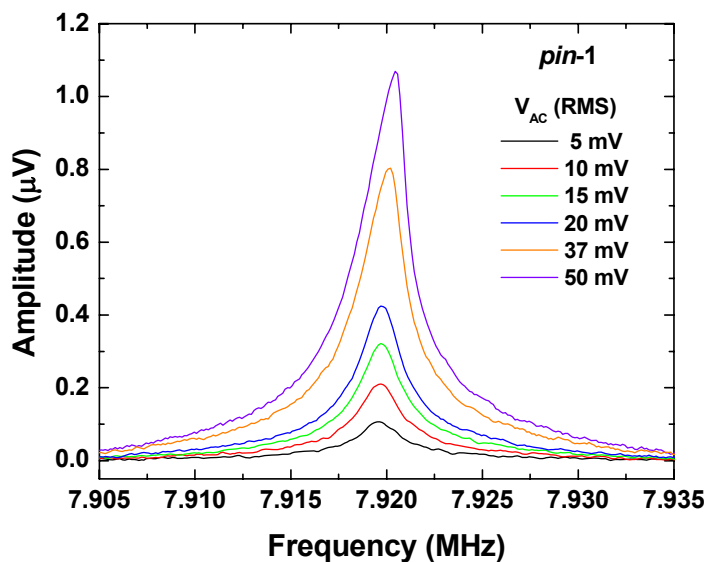


Figure 6.6 Piezoelectric response of the cantilever on one arm of the balanced bridge under different driving amplitudes. The amplitude in μV represents the amount of generated voltage (V_{PZL}) after dividing by the preamplifier gain.

6.5 DC bias-dependent transduction efficiency

In Chapter 2 we demonstrated that the electromechanical actuation efficiency of D-NEMS is tuned by dc bias. The underlying coupling to charge depletion can be tailored to increase, decrease, or not change the resonance amplitude by growing different *pin* diodes doping profiles. One of our motivations in performing those experiments using optical interferometry rather than electrical detection was to isolate the electromechanical coupling to actuation from the sensing part. Here we show that the apparent coupling does indeed dramatically change when measuring piezoelectric response. Figure 6.7 plots the normalized resonance amplitude of a 4 μm cantilever as a function of dc voltage measured by optical and piezoelectric means. The doping profile of diode *pin*-1 was designed such that resonance amplitude increases with higher reverse bias. This is confirmed by both modes of detection; however, the slope of the piezoelectric measurement is higher than the optical measurement. This discrepancy is believed to be due to two salient features of piezoelectric detection: First, both actuation and detection depend on the same strain distribution in the depletion region, and second, the capacitive coupling is reduced by reverse biasing the diode. By taking the square of the optical signal (green line in Fig. 6.7) we arrive at a much closer agreement with the piezoelectric signal. The remaining difference in slope between the green line and blue dots is attributed to variable capacitance (varactor) effects.

To conclude this section, we have confirmed there are many ways of coupling transduction efficiency to applied voltage. By relying on optical detection we were able to isolate out the effect on actuation alone, but practical devices employing piezoelectric detection will invariably exhibit stronger coupling. This could pose a problem for applications that demand low coupling, and likewise it could offer some benefits if tunable transduction is a useful feature.

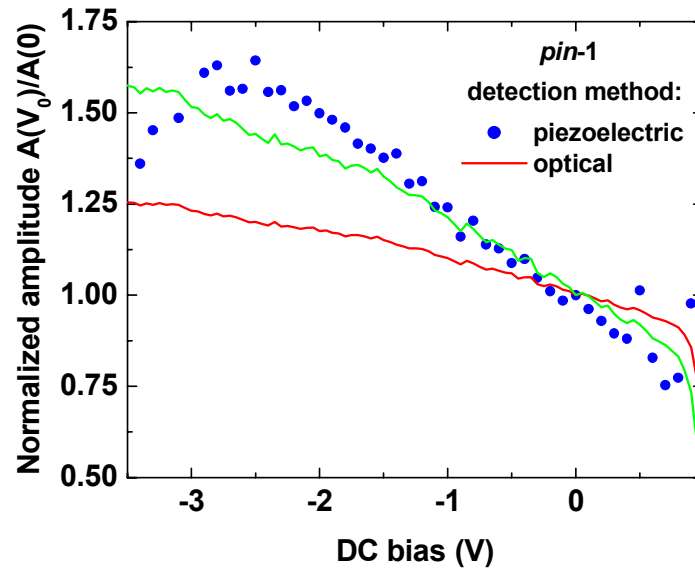


Figure 6.7 Mechanical resonance amplitude vs. dc bias voltage using piezoelectric (dots) and optical (red line) detection. The noisier nature of the dots underscores the lower SNR of piezoelectrically transduced signals. Data are normalized to their respective amplitudes at zero bias. The difference in slope between the different sensing methods is a result of the fact that, like actuation, piezoelectric detection is sensitively coupled to strain distribution in the depletion region and to the capacitance, which can be reduced by reverse biasing the diode. Green line denotes the square of the optically detected signal and corresponds to the ideal dependence of the piezoelectric signal on voltage. The larger slope of the dots signifies the additional influence of capacitive coupling.

6.6 Prospects for improving piezoelectric detection

Although we can now readily measure piezoelectric signals from our D-NEMS, considerable improvements must be made before this mode of detection becomes comparable to optical or piezoresistive means. First, a better designed heterostructure could lead to increased coupling efficiency. The analysis for piezoelectric sensing follows the same principles as actuation discussed in Chapter 2. In order to increase electromechanical coupling the active layer has to be placed far from the neutral axis of strain. In practice, we estimate the coupling cannot be improved by more than a factor of two or three from what is found in diode *pin-1*. Thus other, more substantial changes need to be made. Better bridge balancing is required to remove the

background more completely. Capacitance reduction from cables and electrodes is of paramount importance for improving SNR and increasing the bandwidth of these transducers. Figure 6.8 shows the size of the electrodes relative to the device. Clearly there is ample scope for reducing their size. Cables are another major source of parasitic capacitance, and on-chip preamplification may be necessary to curb their effect. Another approach to improving piezoelectric detection in NEMS might be to implement the analog of piezoresistive downmixing³, exploiting the fact that capacitive impedance can be tuned with voltage. We note however, that depletion width varies nonlinearly with voltage, which could potentially raise problems.

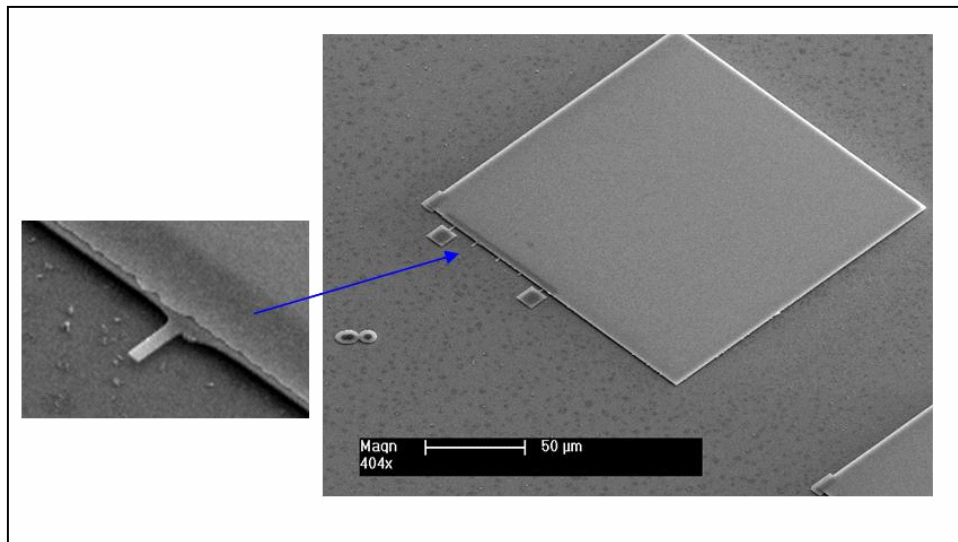


Figure 6.8 SEM image of device footprint with close-up of a 4 μm cantilever used in the measurements. The large, 150x150 μm² gold electrode (smooth gray square) is needed for making wirebond connections. Due to the current epilayer design the entire electrode is capacitively coupled to ground and significantly diminishes the detection efficiency. A reduction of the contact area to 4 μm² and on-chip integration of preamplifiers would boost piezoelectric transduction by about a factor of 5,000.

Finally, it is instructive to make a quantitative estimate about how much one would need to improve the SNR in order to detect the thermal fluctuations. The smallest drive amplitude that can generate a piezoelectrically measurable displacement was found to be $\approx 50 \mu V / \sqrt{Hz}$. That

value is about 60 times higher than the thermomechanical noise limit, which was determined by a comparison to optically measured displacements plotted in Figure 6.9. Thus we would need to improve the SNR by almost 100 times in order to detect the thermomechanical response of an 8 MHz, $4 \times 0.8 \times 0.2 \mu\text{m}^3$ cantilever operating at room temperature and connected to the large electrode depicted in Figure 6.8. If we reduced the electrode area to $4 \mu\text{m}^2$ and minimized interconnect lengths by integrating the amplifying electronics directly adjacent to the device⁹, the transduced piezoelectric voltage would increase by a factor of 5,000, or 50 times higher than the thermomechanical noise limit at room temperature. So in principle one could achieve excellent displacement sensitivity. Schemes incorporating single electron transistors with piezoelectric NEMS have been proposed as a means of attaining displacement sensitivity approaching the quantum limit^{10,11}. Thus the potential is definitely there for improving SNR to impressive levels; the challenge is getting rid of the appreciable parasitic capacitance.

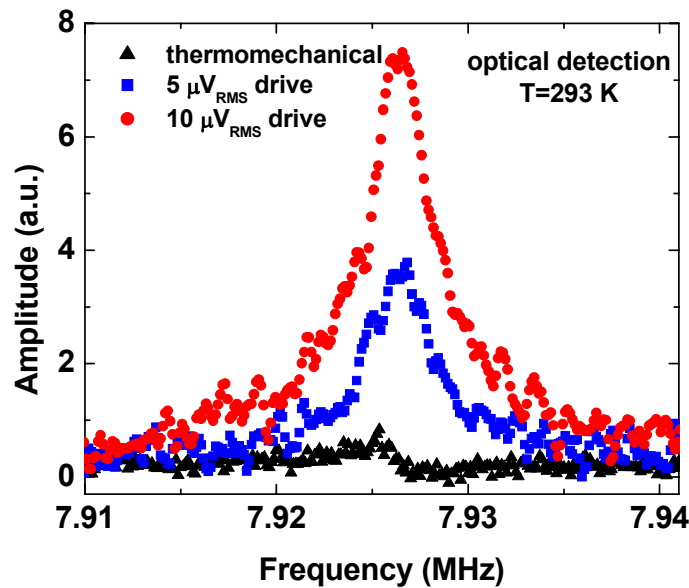


Figure 6.9 Optically measured response of the same cantilever used to record data in Figures 6.6 & 6.7. The thermomechanical noise is 6 times weaker than an rms drive of $5 \mu\text{V}$, or 60 times weaker than a $50 \mu\text{V}$ drive.

References

1. H. Ukita, Y. Uenishi, & H. Tanaka, A photomicrodynamic system with a mechanical resonator monolithically integrated with laser diodes on gallium arsenide, *Science* **260**, 786-789 (1993)
2. G. Piazza, K. Castelino, A. P. Pisano, C. J. Chang-Hasnain, Design of a monolithic piezoelectrically actuated microelectromechanical tunable vertical-cavity surface-emitting laser, *Optics Letters* **30**, 896-898 (2005)
3. I. Bargatin, E. B. Myers, J. Arlett, B. Guglewski, M. L. Roukes, Sensitive detection of nanomechanical motion using piezoresistive signal downmixing, *Appl. Phys. Lett.* **86**, 133109 (2005)
4. A. Sagar, Piezoresistance in *n*-Type GaAs, *Phys. Rev.* **112**, 1533 (1958)
5. D. Rugar & P. Grütter, Mechanical parametric amplification and thermomechanical noise squeezing. *Phys. Rev. Lett.* **67**, 699 (1991)
6. for a review see K. M. Lakin, Thin film resonator technology, *IEEE Trans. Ultra., Ferro. & Freq. Control* **52**, 707 (2005)
7. P. H. Carr, Measurement of the piezoelectric constant of quartz at gigacycle frequencies, *J. Acoust. Soc. Am.* **41**, 75 (1967)
8. S. Adachi, GaAs, AlAs, and $\text{Al}_x\text{Ga}_{1-x}\text{As}$: material parameters for use in research and device applications, *J. Appl. Phys.* **58**, 1 (1985)
9. R. G. Beck, M. A. Eriksson, R. M. Westervelt, K. L. Campman, A. C. Gossard, Strain-sensing cryogenic field-effect transistor for integrated strain detection in GaAs/AlGaAs microelectromechanical systems, *Appl. Phys. Lett.* **68**, 3763-3765 (1996)
10. R. Knobel & A. N. Cleland, Piezoelectric displacement sensing with a single-electron transistor, *Appl. Phys. Lett.* **81**, 2258-2260 (2002)
11. Y. Zhang & M. P. Blencowe, Sensitivity of a piezoelectric micromechanical displacement detector based on the radio-frequency single-electron transistor, *J. Appl. Phys.* **92**, 7550-7555 (2002)

Chapter 7

Nanomechanical measurement of magnetostriction and magnetic anisotropy in GaMnAs

7.1 Background and motivation for GaMnAs experiment

The focus up to this point has been on electromechanical coupling mediated by piezoelectric effects. We now turn to the study of magnetomechanical coupling mediated by magnetoelastic stress. Magnetoelasticity, which is synonymous with magnetostriction, is defined as the lattice dilation of a ferromagnet in an applied magnetic field. By measuring the frequency shift as a function of voltage in Chapter 3 we were able to calculate the piezoelectric constant of GaAs. This means in principle we can obtain information about any elastic coupling parameter by measuring its influence on frequency. Ideally the underlying coupling can be discriminated from other effects if it can be altered under a controlled “stimulus,” such as an electric field in the case of piezoelectricity. This chapter describes the experiment aimed at observing magnetoelastic coupling in a resonant nanoelectromechanical system.

This project spawned out of earlier work in Michael Roukes’ group on a relatively new ferromagnetic compound, GaMnAs, which I became involved with during the first three years of my graduate studies. GaMnAs belongs to the class of materials known as ferromagnetic semiconductors (FMS), and more specifically, because manganese content is low they are referred to as dilute magnetic semiconductors (DMS)^{1,2}. The unique properties of these materials arise from their carrier-mediated spin exchange interactions, which open the path for controlling

ferromagnetism by carrier density modulation, *e.g.*, via illuminating or gating devices^{3,4}. DMS are one of the holy grails in the nascent field of spintronics^{5,6}, because they offer the potential for merging the storage capability of magnets with the signal processing capability of semiconductors, that could give rise to new magnetoelectronic devices. In short, they share all the familiar properties of GaAs, plus they exhibit a unique type of ferromagnetism. However, they currently suffer a major setback: their Curie temperature is too low to be of practical value. The record is still a frigid temperature of about 170 K, and prospects for room temperature DMS operation – in GaMnAs or alternative materials – remain uncertain despite theoretical⁷ and experimental⁸ evidence suggesting the contrary.

Fortunately, there is still a wealth of new physics that can be explored at low temperatures. I already mentioned gating and illumination as means of controlling ferromagnetic properties, but mechanical stress is another possibility that has not been carefully explored. I was motivated by the fact that the magnetoelastic parameters of GaMnAs, or any DMS for that matter, had not been previously experimentally determined. Although most ferromagnets are magnetostrictive, DMS may exhibit carrier-mediated magnetostriction, so obtaining these parameters may provide additional insight into the behavior of these new materials. A quantitative measurement of these parameters is important in gauging the impact of magnetostriction on magnetic⁹ and electrical transport properties^{10,11}, and is therefore essential to a comprehensive understanding of DMS systems. For instance, it is known that strain from substrate-GaMnAs lattice mismatch has an effect on magnetic alignment; a difference of just 1% compressive or tensile strain is known to flip the magnetization from in-plane to out-of-plane². This is consistent with a substantial *inverse magnetoelastic* effect, which cannot be clearly understood without first determining the magnetoelastic constants.

Another motivating factor was that DMS may be the only compounds to possess a combination of magnetoelastic, piezoelectric and piezoresistive phenomena. Although piezoelectricity and piezoresistivity had not been demonstrated in these materials, it follows from

the similarities to their host semiconductor (*i.e.*, GaAs) that they should have these properties. This suggests that DMS might provide the basis for new devices that rely on both electromechanical and magnetomechanical coupling. This does not appear to have been noticed by the spintronics community, but it did not fail to capture the attention of GaMnAs enthusiasts in this group. In particular, Dr. Hong Tang had fabricated suspended DMS structures and attempted to mechanically excite them using a piezoelectric dipolar interaction technique he had devised¹², and he encouraged me to try it with better material. This eventually led me to carry out this project. It is worth pointing out that this work was completed before any research into D-NEMS was begun.



Figure 7.1 The “dipper” used to conduct low-temperature experiments on (Ga,Mn)As. The length is around 2 meters, and everything underneath the flange is immersed in a liquid helium cryostat. The brass sample holder fits inside a 3-axis superconducting solenoid.

This project posed some additional challenges owing to the high vacuum and low temperatures involved. Thus, while we have fabricated and tested several dozen D-NEMS devices, we only made six working GaMnAs-NEMS samples, and results are presented only for the longest-surviving (sixth) beam. The samples were mounted on a cold finger stage that was fixed inside a “dipper” shown in Figure 7.1. After pumping the interior to less than 10^{-6} Torr, the

dipper was precooled in liquid nitrogen before being immersed in a liquid helium cryostat. The process of sample mounting, pumping, and precooling took at least half a day. Moreover, only one device could be tested at any given time. The next stage of the experiment consisted of “hunting” for a resonance peak using piezoresistive sensing techniques; this often led to inadvertent destruction of the device via electrostatic discharge (ESD). If all these steps proved successful, the device was ready for measurement with magnetic fields. Our best sample survived for over a month in this operational state before succumbing to the vagaries of ESD.

Finally, a few words on the properties of $\text{Ga}_{1-x}\text{Mn}_x\text{As}$. It is a heavily doped *p*-type semiconductor with manganese concentrations ranging between 1 % and 8%. The optimal concentration for magnetic and electrical properties is ~5%, which corresponds to a carrier density of $\sim 10^{21} \text{ cm}^{-3}$ and magnetization of $\sim 0.05 \text{ T}$. The ferromagnetic Curie temperature in as-grown GaMnAs is 40 – 70 K and by thermal annealing, it has been shown to increase to as much as 170 K. Ferromagnetic interactions are mediated by delocalized holes, which are anti-ferromagnetically coupled to manganese spins, leading to a net ferromagnetic exchange coupling. The only way to reliably grow GaMnAs is by low-temperature molecular beam epitaxy, in which manganese atoms substitutionally occupy the gallium site on the GaAs lattice. In practice, up to 40% of the manganese occupies interstitial sites, which lead to double (*i.e.*, 80%) loss in ferromagnetism. It is widely believed that thermal annealing helps remove these interstitials. GaMnAs crystallizes in the zinc blende structure with a lattice constant that was found by Ohno¹ to obey the relation $(0.566+0.032x) \text{ nm}$, where x is the fractional manganese level and 0.566 nm is the lattice constant of intrinsic GaAs. Thus a 5.2% Mn concentration gives rise to a -0.3% mismatch or a 0.3% *compressive* strain on GaMnAs.

7.2 Magnetoelastic NEMS resonator

Magnetostriction is divided into two categories: anisotropic and forced effects. The *anisotropic* effect describes how strain varies with the angle of magnetization; in the simplest case this is characterized by the expression¹³

$$e = (3\lambda / 2)(\cos^2 \phi_M - 1/3) \quad (6.1)$$

The magnetostriction constants quoted in the literature, usually denoted by the symbol λ , are dimensionless quantities that refer to the anisotropic strain measured under saturated magnetization. A subscript may be added to λ to distinguish which direction the strain acts in. The most commonly quoted first order parameters are λ_{100} and λ_{111} , but it is possible to have higher order constants too, as we will see later in the chapter. The *forced* magnetostriction describes how strain varies with magnetic field. It usually arises from partially unsaturated magnetization that increases in strength with an applied field¹³, and is typically a weak effect. If forced effects exist it may be necessary to measure λ in a partially unsaturated state. Finally, other variants of magnetostriction exist, such as parastriction, which is the field-dependent strain in a paramagnetic material.

Our experiment is carried out with a doubly clamped beam resonator. The material is grown epitaxially on a GaAs (001) substrate, beginning with a 1 μm $\text{Al}_{0.8}\text{Ga}_{0.2}\text{As}$ sacrificial layer, followed by 50 nm high temperature and 50 nm low temperature GaAs, and finally 80 nm unannealed $\text{Ga}_{0.948}\text{Mn}_{0.052}\text{As}$. We deliberately made the lower part of the structure nonmagnetic, to avoid a possible increase of interstitials at the GaMnAs-AlGaAs boundary¹⁴. A T_C of 57 K is obtained by measuring the temperature at which a local resistance extremum occurs, which coincides with the onset of spin-disorder scattering¹⁴. The resistance across the device is plotted as a function of temperature in Figure 7.2. The spontaneous magnetization is expected to lie in the growth plane due to a compressive strain from the substrate and demagnetization effects.

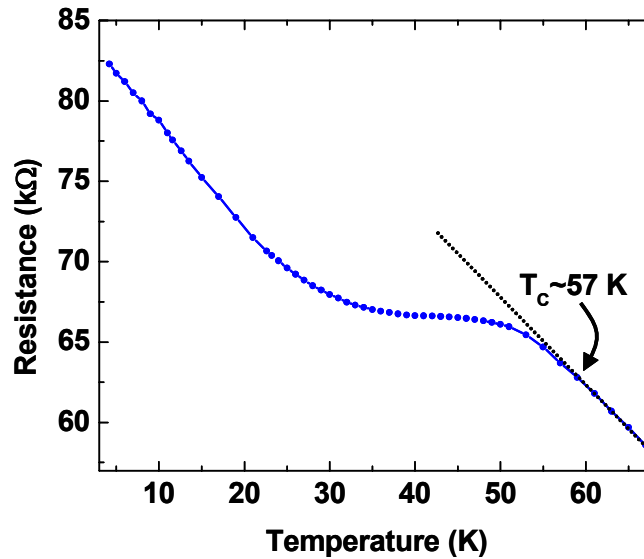


Figure 7.2 Resistance vs. temperature of the suspended $\text{Ga}_{0.948}\text{Mn}_{0.052}\text{As}$ device shown in Fig. 7.3a. The curvature beginning at 57 K marks the onset of ferromagnetic ordering, which is accompanied by spin-spin scattering. The measured Curie temperature is consistent with the reported values of unannealed samples. The room temperature device resistance is 29 kΩ.

Although we have not independently measured the magnetization, we can calculate its saturation value from manganese doping level considerations. A 5.2% Mn concentration corresponds to a number density of $1.1 \times 10^{21} \text{ cm}^{-3}$. The spin per Mn ion is 5/2, and $g=2$. This leads to the result $M_S = \mu_0 N_{\text{Mn}} g S_{\text{Mn}} \mu_B = 0.06 \text{ T}$, where μ_B is the Bohr magneton. Actual values will always be less because some Mn ions form interstitial bonds and do not contribute to ferromagnetic interactions. Thus a more realistic estimate based on reported values¹⁵ would be 0.04 – 0.05 T. Fabrication of the sample begins with deposition of Au/Pd/Ti wirebond electrodes. Electron-beam lithography is used to define the device profile, which is subsequently covered with a titanium etch mask. Next, argon ion milling removes all magnetic material not protected by the mask. A 30 nm thick gold side gate is deposited 0.7 μm away from the beam after another e-beam lithography step. The gate electrode was intentionally deposited after removing all magnetic material from the gate region, to avoid any unwanted magnetomechanical interactions.

Finally, a rectangular resist window is patterned to expose the sacrificial layer, which is selectively removed along with the remaining titanium mask in dilute hydrofluoric acid. The resulting suspended structure, shown in Figure 7.3a, has dimensions of $(L, w, t) = (6, 0.5, 0.18) \mu\text{m}$, with its longitudinal axis oriented along the $[110]$ crystallographic direction. The sample is mounted in a liquid helium cryostat in vacuum, and surrounded by a 3-axis, 10 kOe superconducting magnet. The two-terminal device resistance at 4.2 K is $83 \text{ k}\Omega$. A thermometer coupled to a resistive heater in the dipper allows us to control temperature from the base value of 4.2 K, to as high as 70 K.

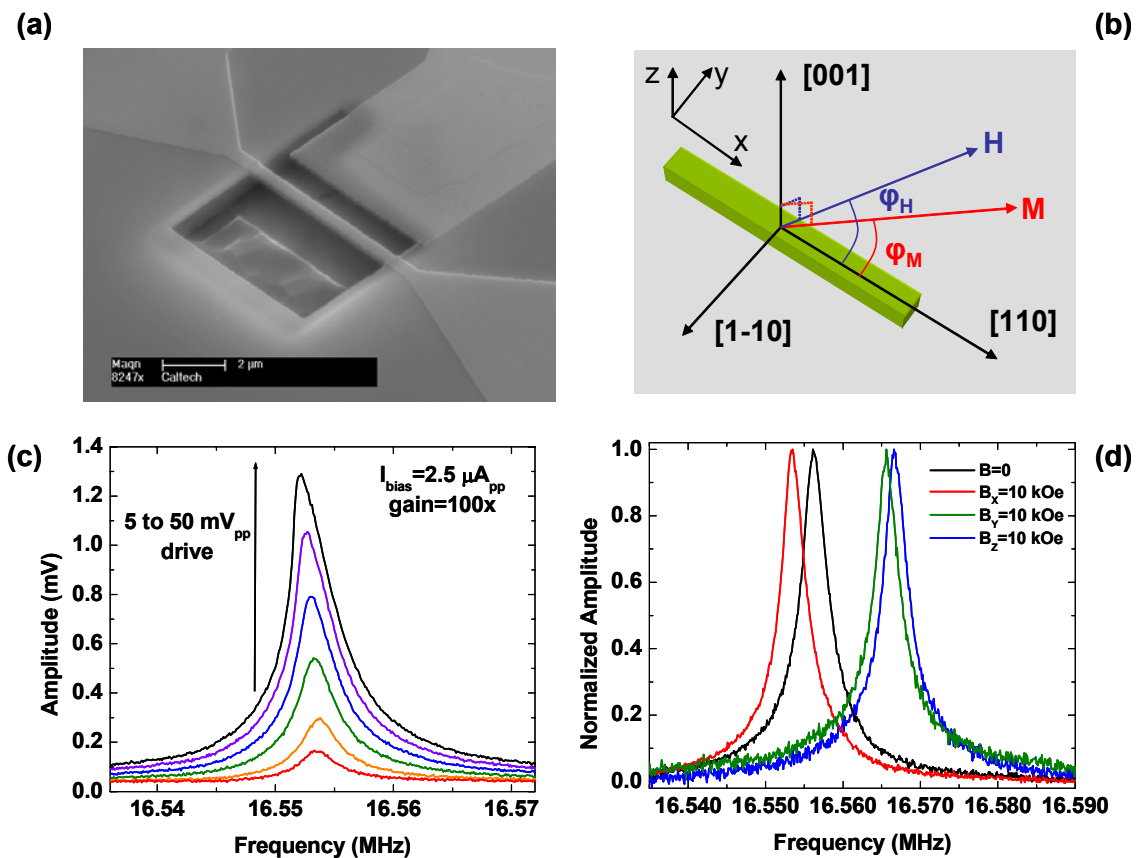


Figure 7.3 (a) Image of the $6 \mu\text{m}$ long doubly clamped beam device. The top 80 nm consists of $\text{Ga}_{0.948}\text{Mn}_{0.052}\text{As}$ and the bottom 100 nm of low temperature nonmagnetic GaAs. The coordinates and relevant magnetization and field angles are shown for reference in (b). (c) plots the piezoresistive downmixed response to different driving voltages, while (d) displays the resonance shifts in the presence of a 10 kOe magnetic field oriented along the three principal directions. The shifts are a result of magnetoelastic stress on the beam.

Actuation is achieved by applying an ac voltage on the side gate, which drives the beam out-of-plane. This actuation scheme was first characterized by Tang *et al.* and I refer the reader to the relevant publication¹² for more information. Briefly, it is a dipolar interaction between the gate and Piezoelectrically induced charges on the beam. The transverse piezoelectric constant d_{31} of zinc blende semiconductors results in an out-of-plane dipole moment. This scheme should not be confused with the electrostatic coupling method, which is much less efficient at driving devices orthogonal to the direction of the applied electric field. This is also unrelated to the multilayer mechanism used to drive D-NEMS. Detection is carried out via the piezoresistive downmixing scheme¹⁶ with the signal recorded on a lock-in amplifier following low noise preamplification. To minimize impedance mismatch problems to the ~ 80 k Ω device, the preamplifier had an input impedance of 1 M Ω . The preamplifier bandwidth was 100 MHz and the gain was set to 40 dB. Care was taken to minimize Joule heating by limiting the sensing current to 2.5 μA_{pp} . The Joule heating profile should be parabolic across the beam with an approximate maximum of $\Delta T_{\text{max}} = LI^2R/(4\kappa_T wt_{\text{mag}})$ at the center, which gives a value of 0.5 K at the base operating temperature. Since the temperature dependence of magnetostriction shall be studied in steps of about 5 K, a heating effect of $\sim 1 - 2$ K will not significantly affect our results. Thus a more rigorous heating analysis is not necessary here. Figure 7.3c shows the frequency response under different driving amplitudes. At 4.2 K and zero external field, the device resonates at 16.56 MHz with a quality factor of 6,300. The piezoresistive gauge factor of GaMnAs can be estimated from the Tilmans formula¹⁷ for critical amplitude at the onset of nonlinearity, $z_{\text{crit}} \approx t_{\text{tot}} \sqrt{4.19/Q} = 4.6$ nm. This deflection corresponds to an axial elongation strain of $\delta e_{xx} \approx 4\delta z^2/L^2 = 3$ ppm. From Figure 7.3c we calculate the change in resistance to be 11.6 Ω . Thus the gauge factor of $\text{Ga}_{0.948}\text{Mn}_{0.052}\text{As}$ at 4.2 K is given by

$$|GF_{\text{GaMnAs}}| = \Delta R/(e_{xx} R) \approx 46 \quad (6.2)$$

The value quoted for p -GaAs in the literature¹⁸ is 17 at room temperature. Since the device increased nearly threefold upon cooling, it is possible that the gauge factor is enhanced by a similar amount. Now the resonance is measured with the magnetic field on. The response to different magnetic field directions is shown in Figure 7.3d. The resonance frequency is tuned up or down, depending on whether the applied field is aligned parallel or orthogonal to the [110] direction. We attribute these shifts to magnetoelastic stress that compresses or stretches the beam. Note that magnetostatic torque effects should be negligible relative to larger, floppier cantilevers used in other studies¹⁹.

The device can be operated as part of a phase-locked loop (PLL), enabling near real-time resonance frequency tracking with a resolution of 4 parts in 10^7 at 4.2 K. Figure 7.4a shows the frequency shifts as a function of field along the three principal beam directions. Experimentally one can identify three distinct tuning regions corresponding to low (<100 Oe), intermediate (100 - 5000 Oe) and high (>5000 Oe) field behavior. In the low field region magnetization reversal appears to proceed via domain wall displacement, characterized by abrupt changes in frequency as shown in Figure 7.4b. The intermediate region apparently coincides with coherent moment rotation described by the Stoner-Wohlfarth model²⁰. Note that hysteresis can be found in the first two regions. The magnetization reversal is complete beyond ~ 5000 Oe, but frequency continues to increase with field. This last observation is consistent with the forced magnetostriction effect.

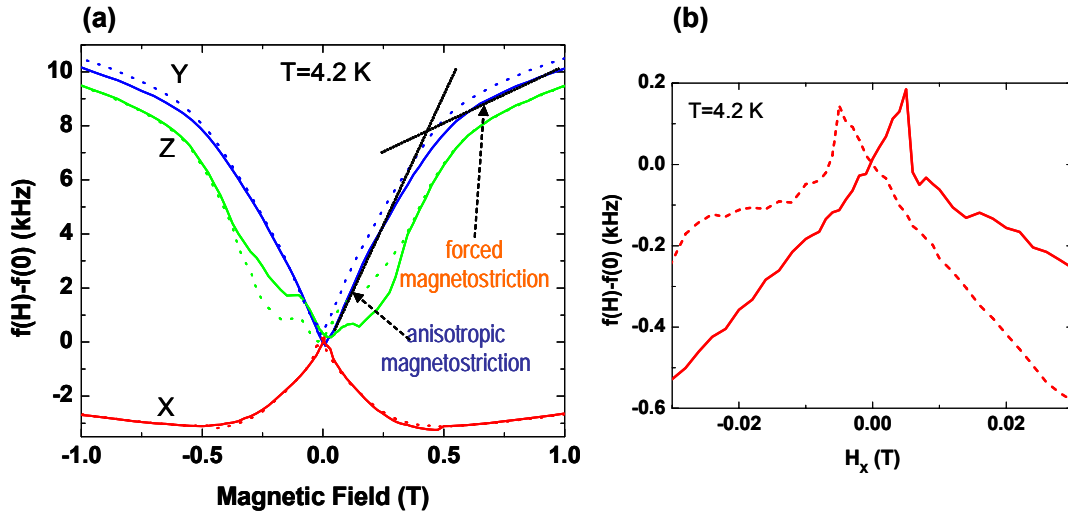


Figure 7.4 (a) Resonance frequency shifts vs. magnetic field along the three principal directions, measured by operating the device in a phase-locked loop. The solid (dashed) lines indicate positive (negative) field sweep directions. Some magnetoelastic hysteresis can be seen, particularly along the z direction. The arrows indicate the regime of anisotropic and forced magnetostriction. (b) Frequency shift for a field along x or [110] in the low field regime. The jumps occur near the coercive field of the material, suggesting they correspond to domain wall transitions.

7.3 Frequency and quality factor at high magnetic field

The 3-axis superconducting solenoid is capable of achieving fields up to 1 Tesla. As a side-project we wanted to investigate the field dependence of frequency shifts at higher fields, which required the use of a 6 Tesla z-axis magnet in a different cryostat. Figure 7.5a plots the field dependence of frequency shifts, and demonstrates that the forced magnetostriction effect persists up to at least 6 Tesla at 4.2 K. Nonetheless the slope of the curve does slowly decrease, suggesting that all magnetoelastic stress converges to a saturated value at some inaccessibly large field, which a rough extrapolation predicts to be around 9 T. It is also found that the quality factor of the resonance changes by about 30% in an applied field, as shown in Figure 7.5b. These observations suggest that the mechanical damping mechanism is quite strongly coupled to ferromagnetic interactions, perhaps via magnetostriction. We presently lack a clearer

understanding of the field-dependent damping, although a magnetoelastically driven ferromagnetic resonance mechanism has been proposed by Myers *et al.*²¹

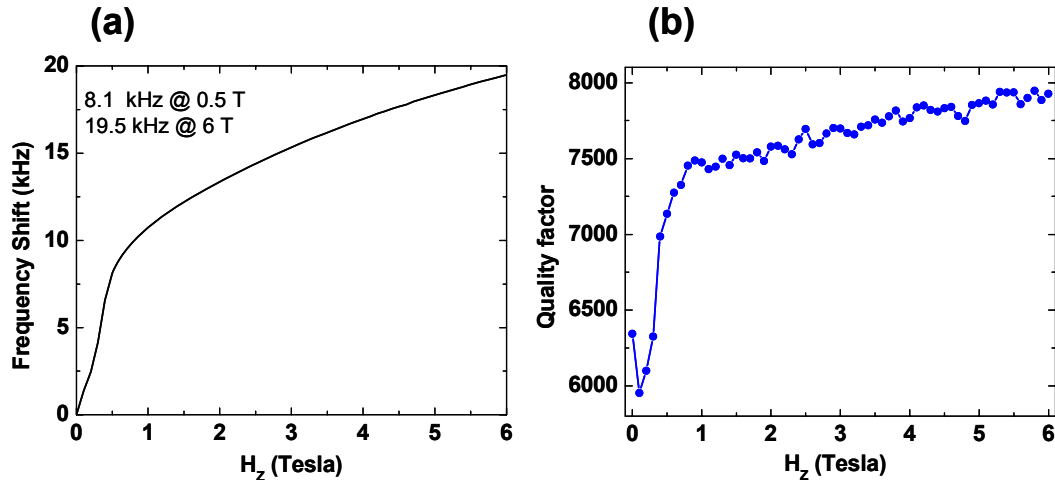


Figure 7.5 (a) Resonance frequency shifts vs. magnetic field along the z axis, measured by operating the device in a phase-locked loop. (b) Quality factor vs. magnetic field, measured every 0.1 T. All measurements are at 4.2 K.

7.4 Temperature dependence of magnetoelastic effects

Returning to the 3-axis solenoid system, the field dependence measurements are extended to higher temperatures in Figure 7.6. For clarity, only the results for a field oriented in-plane and orthogonal to the beam are displayed. The magnitude of the frequency shift decreases with temperature, and a small parastricive effect persists above the Curie point of 57 K up to at least 65 K. Starting at 20 K a downshift in frequency occurs at low and intermediate fields, suggesting qualitative changes occur in magnetostriction as a function of temperature. The slope of the high field, linear part of the curves provides a rough gauge of the forced magnetostriction. We find this effect decreases with temperature and vanishes at around 60 K. The concurrent onset of forced magnetostriction and ferromagnetic ordering in our sample confirms that this phenomenon is intrinsic to GaMnAs, and may be associated with a field-dependent magnetization that remains unsaturated above 1 Tesla^{22,23}.

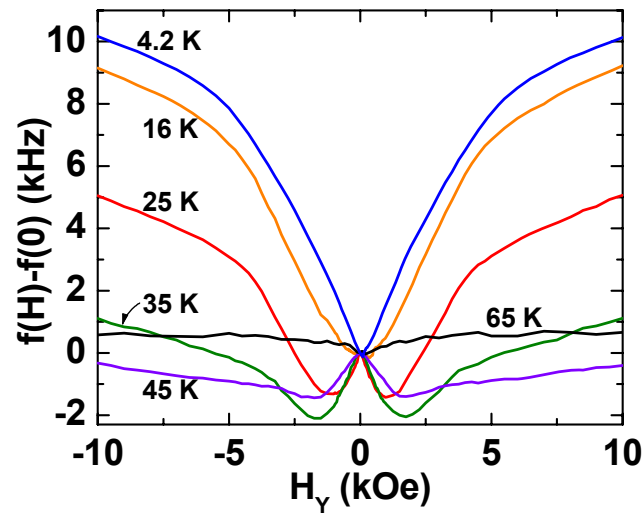


Figure 7.6 Frequency shifts vs. magnetic field along the y direction, *i.e.*, [-110]. The different colors represent different operating temperatures. Upon increasing temperature, the magnitude of frequency shifts decreases, which suggests magnetoelastic effects are reduced with higher T . Starting around 25 K a second effect is observed; the frequency dips down before rising, suggesting qualitative changes in magnetoelastic and magnetic anisotropy parameters are occurring. Finally, there is a small but finite field-dependent frequency shift even above T_c , which could be the result of paramagnetic-magnetoelastic (parastrictive) effects.

7.5 Measurement of magnetostriction and magnetic anisotropy

To gain a better understanding of anisotropic magnetoelastic coupling, the phase-locked loop technique was used to track resonance frequency shifts in a constant-magnitude field that rotated in the plane of the device. The results are plotted in polar coordinates in Figure 7.7, with the field chosen as 5 kOe such that magnetization reversal occurs purely by rotation, *i.e.*, no domain wall displacement. Forced magnetostriction will also be curtailed at this intermediate field value. The field angle ϕ_H is measured with respect to the [110] direction. Between 4.2 K and 20 K we see a twofold symmetry in the angular dependence of the resonance frequency, which is maximized along 90° and 270° , and minimized along 0° and 180° .

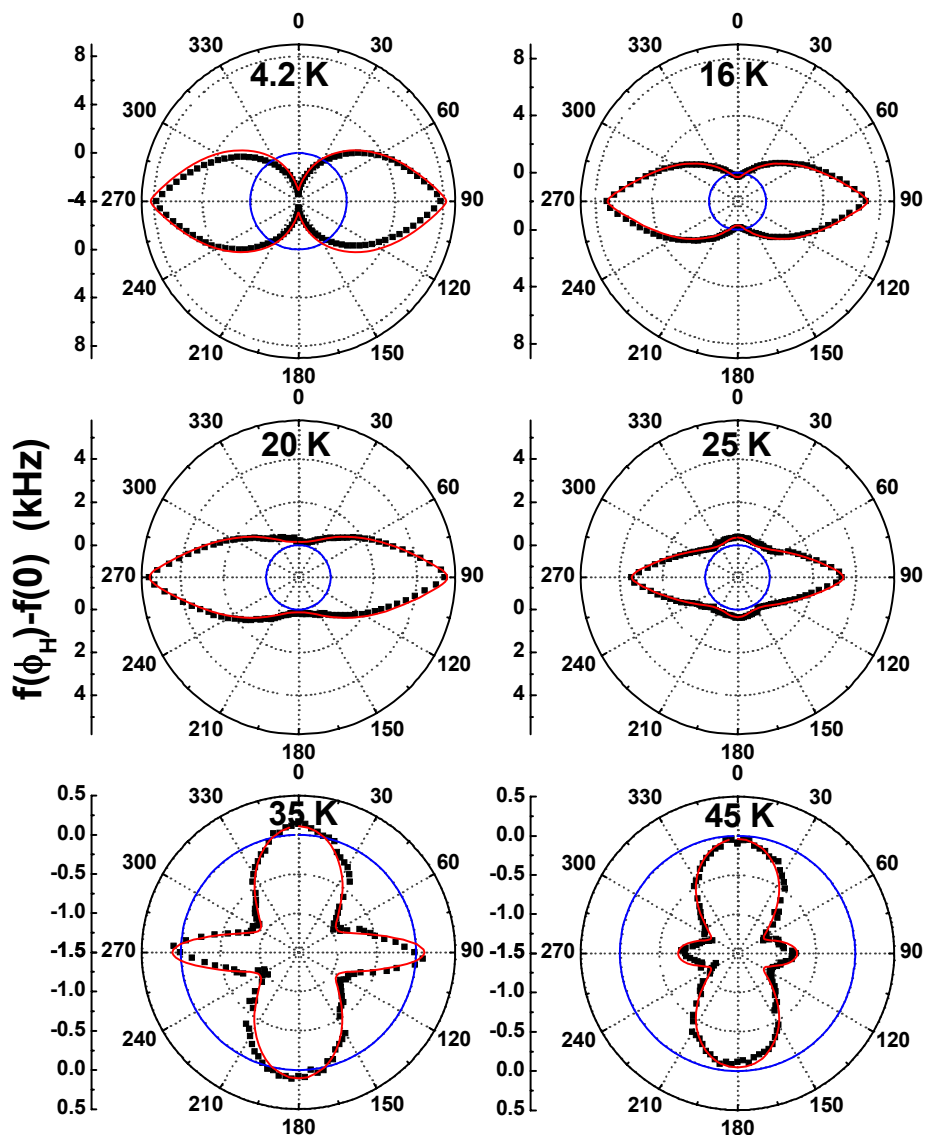


Figure 7.7 Polar plots of frequency shifts vs. in-plane magnetic field angle, at a fixed field magnitude of 5 kOe. The shifts are measured with respect to $f(H=0)$, the frequency at zero magnetic field. The angle $\phi_H=0$ corresponds to the magnetic field aligned parallel to the beam's length, *i.e.* [110]. The experimental data are shown in black; the red lines are obtained from the phenomenological fitting model used to extract the three magnetostriction and two magnetic anisotropy field parameters. The blue circles mark the position of zero frequency shift and are shown for reference. Note the change of scale at different temperature. The onset of fourfold symmetry near 25 K marks the transition from first order to second order dominated magnetoelastic effects. The curvature of the plots can be used to determine the magnetic anisotropy.

However, by 25 K, additional symmetry emerges in the form of two new peaks at 0° and 180° . The new peaks grow with temperature relative to the original pair, and above 35 K they are the dominant feature of angular dependence in Figure 7.7. The onset of this behavior resembles that of the low field frequency shifts seen in Figure 7.6, and suggests qualitative changes in magnetoelastic coupling and magnetic anisotropy occur as a function of temperature.

We now attempt to extract quantitative information from the data in Figure 7.7. The angular dependence of the frequency shifts is modeled after the magnetostriction equation^{13,24} containing the first order terms λ_{100} and λ_{111} corresponding to volume-conserving deformations along [100] and [111] respectively, and a second order term h_3 corresponding to a volume-changing deformation. Note that these parameters can uniquely describe the magnetoelastic strain in any direction. The twofold or fourfold symmetry found in the polar plots can be uniquely and unambiguously described by first and second order magnetostriction. Combining this model with the stress-strain relation gives the following expression for the excess axial magnetoelastic stress on the beam relative to the zero field stress:

$$\begin{aligned} \sigma_{ML} = & (\lambda_{100}/4)(c_{11} - c_{12}) + (3\lambda_{111}/4)(c_{11} - c_{12}) \cos 2\phi_M \\ & + (h_3/4)(c_{11} + 2c_{12}) \cos^2 2\phi_M \end{aligned} \quad (6.3)$$

where ϕ_M is the in-plane magnetization angle. The inclusion of the second order term is necessary to explain the fourfold symmetry seen above 20 K. The elastic constants of $\text{Ga}_{0.948}\text{Mn}_{0.052}\text{As}$ have not been directly measured but are assumed to be very similar to those of GaAs: $c_{11}=121.6$ GPa and $c_{12}=54.5$ GPa as reported elsewhere²⁵. The weakest link in our analysis is accurately determining the amount of stress needed to shift the resonance by a known amount. The crudest estimate is to adopt the Timoshenko formula used to characterize axial force-dependent frequency tuning in Chapter 3. Upon stressing the 80 nm thick magnetoelastic layer we predict a stress-frequency gauge factor of $-\sqrt{3}/\rho Y t_{ML}/(2\pi t_{tot}^2) = -28$ Hz/kPa. For consistency this result is compared to a finite element simulation and find that the simulation

predicts $\Delta f / \Delta \sigma_{ML} = -13.9$ Hz/kPa, or twice as small a gauge factor. The latter result was used in the analysis, because it is believed the simulation more accurately represents the beam's stress at interfaces. We have also assumed that thermal expansion and lattice mismatch do not introduce enough built-in stress to invalidate the linear frequency tuning approximation. Figure 7.8 shows the structure used to simulate magnetoelastic frequency tuning effects by finite element methods.

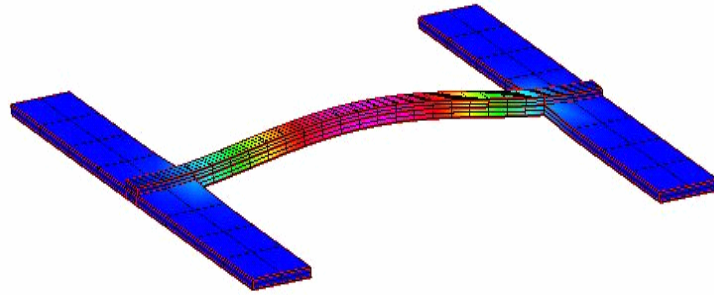


Figure 7.8 Structure used to model the effect of magnetoelastic stress on the resonance frequency. It is a beam with dimensions $(L, w, t) = (6, 0.5, 0.8)$ μm and ledges 1 μm wide. The clamping points are assumed to be at the six outward facing edges. The finite element program CFDRC was employed. The simulation predicts $\Delta f / \Delta \sigma_{ML} = -13.9$ Hz/kPa, which is a factor of two lower than the analytical expression. It is possible that the beam supports and GaMnAs-GaAs interfaces are responsible for the discrepancy.

The axial magnetoelastic stress equation (Eqn. 6.3) is expressed in terms of the in-plane magnetization angle, but our control parameter is magnetic field angle ϕ_H , which because of magnetic anisotropy, is not necessarily equal to ϕ_M . Previous studies²⁶ on compressively strained GaMnAs have determined that its in-plane magnetization is characterized by a uniaxial anisotropy K_U and a cubic anisotropy K_1 . K_1 is consistent with the crystalline symmetry of the material and is therefore also referred to as the cubic magnetocrystalline anisotropy. On the other hand, the origin of K_U is debated but is believed to be related to GaAs surface reconstruction²⁷. It is necessary to include these parameters in our model in order to quantitatively describe the

curvature of the angular dependence of frequency in Figure 7.7. The Stoner-Wohlfarth model is used to couple the magnetoelastic stress equation to the measured frequency shifts, which are measured with respect to the field angle. The corresponding minimum free energy condition is²⁶

$$H_{KU} \sin 2\phi_M - (H_{K1}/2) \sin 4\phi_M + 2H \sin(\phi_M - \phi_H) = 0 \quad (6.4)$$

The first order in-plane uniaxial and cubic anisotropy fields are given by $H_{KU} = 2K_U / M$ and $H_{K1} = 2K_1 / M$. We ignore the magnetoelastic second order anisotropy contribution to free energy, because this varies as $\sim E\lambda^2 \cos^4 \phi_M$ and can be disregarded for small λ .

With this assumption, Eqns. 6.3 and 6.4 are effectively coupled via a single parameter ϕ_M , enabling extraction of the magnetostriction and anisotropy parameters by a straightforward best fit analysis. The fitting analysis is carried out as follows. First, the three magnetostriction constants are obtained by applying the stress-frequency gauge factor on Eqn. 6.3 and fitting to the frequency shift maxima and minima that occur in the data of Figure 7.7 at multiples of $\phi_M = 90^\circ$. The magnetization is independent of anisotropy along these field directions. To obtain H_{KU} and H_{K1} , Eqn. 6.4 is fed into Eqn. 6.3 after being solved with trial anisotropy constants, and the procedure is iterated to produce the best fit to the data. We underscore the necessity of including magnetic anisotropy in our model in an example in Figure 7.9, which displays the fit with and without anisotropy. The fits are included in Figure 7.7. We find this model quantitatively explains the angular dependence of the frequency shifts over the entire ferromagnetic regime, up to the Curie temperature of ~ 57 K.

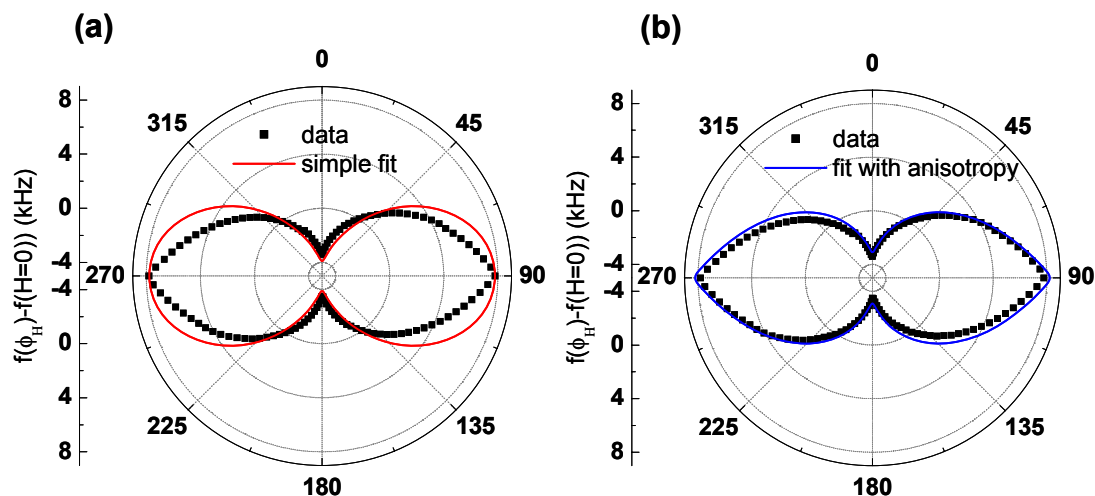


Figure 7.9 Role of magnetic anisotropy. (a) The magnetoelastic stress equation is fit to the polar data from Figure 6.7 at $T=4.2$ K, without any anisotropy. The fit correctly accounts for the frequency shifts at $\phi_H=0, 90, 180$ and 270° but incorrectly describes the curvature. (b) Adding a cubic and uniaxial anisotropy term to the model correctly describes the curvature.

7.6 Discussion of results

The experimentally derived magnetostriction and magnetic anisotropy field parameters are plotted in Figures 7.10(a,b). At 4.2 K, the first order magnetostriction constants of $\text{Ga}_{0.948}\text{Mn}_{0.052}\text{As}$ along [100] and [111] are $\lambda_{100}=-11.3$ ppm and $\lambda_{111}=8.1$ ppm, respectively. To put these values into perspective, Table 6.1 lists the constants of some common materials. We find that GaMnAs is weakly magnetoelastic relative to most ferromagnets, probably because of its dilute manganese content. On the other hand, the magnetic anisotropy fields are quite large for the same reason. The measured anisotropy fields are in agreement with values from studies on bulk GaMnAs films^{27,28}. Based upon the range of parameters that fit the model, our results are accurate to within ± 0.1 ppm and ± 0.3 kOe in magnetostriction and anisotropy, respectively. The larger relative error in anisotropy reflects the more indirect coupling between that quantity and mechanical resonance frequency. We have also ignored the uncertainty of our stress-frequency

gauge factor, which could be as much as a factor of two. In that case our magnetoelastic parameters would decrease by a factor of two, but the anisotropy fields would remain unchanged.

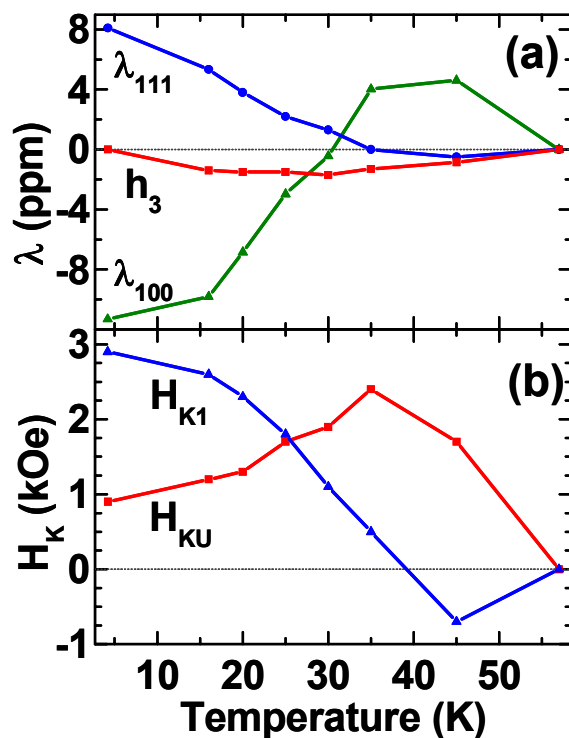


Figure 7.10 Magnetostriction (a) and magnetic anisotropy field (b) parameters of $\text{Ga}_{0.948}\text{Mn}_{0.052}\text{As}$ vs. temperature. Note that all parameters undergo either a sign change, maximum or minimum in the vicinity of $T=35$ K, suggesting that a common hole-mediated phenomenon governs both magnetostriction and magnetic anisotropy. The results in (a) represent the first measurement of magnetostriction in any dilute magnetic semiconductor, and thus could be the first observation of hole-mediated magnetoelastic effects.

Material	λ_{100} (ppm)	λ_{111} (ppm)
Fe	21	-21
Co	-140	50
Ni	-46	-24
Terfenol	-	1600
YIG	-1.4	-1.6

Table 7.1 Room-temperature magnetostriction constants of some common ferromagnetic materials. From Ref. 29.

The temperature dependence displayed in Figure 7.10 reveals an intricate coupling between magnetostriction and magnetic anisotropy. At 4.2 K both H_{KU} and H_{K1} are positive and $H_{K1} > H_{KU}$, indicating the magnetization lies in the (001) plane with cubic easy axis symmetry close to [100] and [010]. The uniaxial anisotropy H_{KU} tips the moments in the direction of [110] by an angle of $0.5 \sin^{-1}(H_{KU}/H_{K1}) = 9^\circ$. The magnitude of the tilting angle gradually increases and by 25 K, complete realignment along [110] has occurred accompanied by a changeover to uniaxial easy axis symmetry. It is notable that the same transition is observed elsewhere²⁷. The span between 30 and 40 K is marked by significant qualitative changes in all measured parameters. Specifically, λ_{100} and λ_{111} change sign while H_{KU} and h_3 attain their respective local maximum and minimum values. The trend of H_{K1} suggests it changes sign at around 40 K. In spite of this, the device retains its uniaxial easy axis symmetry along [110], since $|H_{KU}| > |H_{K1}|$. The sign change of cubic anisotropy with increasing temperature appears to be consistent with models of carrier-mediated ferromagnetism in DMS^{30,31}. An apparently related phenomenon is the sign change in magnetic anisotropy observed upon raising temperature^{32,33}. These observations may be the result of a thermally driven increase in hole density; however, due to the huge concentration of dopants the origin of this temperature dependence is not clear. Magnetostriction, like anisotropy, arises from interactions between neighboring magnetic moments and, consequently, it is also expected to be coupled to the carrier density. This is supported by the similar temperature dependence observed between magnetostriction and anisotropy in Figure 7.10. Moreover, the dependence of valence band energy on strain leads us to expect a sensitive interplay between hole density, magnetic anisotropy, magnetostriction and other sources of strain in dilute magnetic semiconductors. Lattice thermal expansion, in particular, may play a role in this process, as it changes sign³⁴ in the temperature regime relevant to DMS, and is known to vary with carrier density³⁵. We can attempt to estimate the

concentration of strain-induced carriers n_σ using the pressure derivative of the band gap of GaAs³⁶, which is $dE_g/dP = 2 \times 10^{-23} \text{ cm}^{-3}$. The volumetric strain due to excess carriers is approximately given by³⁷ $e_{tot} = n_\sigma dE_g/dP$. If the nominal concentration is 10^{21} cm^{-3} then the overall change in density is $dn_\sigma/de \approx 0.005\%$ per ppm strain. To check the accuracy of this result let us recalculate it with another method, assuming the piezoresistive gauge factor of GaMnAs is primarily from carrier concentration-dependent conductivity. We then predict from Eqn. 6.2 that $dn_\sigma/de = GF_{GaMnAs} \approx 0.005\%$ per ppm strain. The two results are found to agree with each other. This may seem like a negligible effect but consider that just 1000 ppm strain from lattice mismatch can completely alter the magnetic free energy landscape of GaMnAs³⁰. Therefore it is reasonable that an ~ 10 ppm strain from thermal expansion and magnetoelastic effects can partially change free energy (hence magnetostriction and magnetic anisotropy) to the extent observed in our experiment and plotted in Figure 7.10b. However, we do not claim to have more than a crude qualitative understanding of the intricacies of magnetoelastic interactions in carrier-mediated DMS. The important point we wish to convey is that even small strains should not be overlooked, because they may lead to substantially altered behavior.

7.7 Inverse magnetoelastic contribution to magnetic anisotropy

Applying a stress to GaMnAs can produce inverse magnetoelastic anisotropy fields. It has been suggested that the uniaxial anisotropy K_U is a result of such a magnetoelastic coupling³⁰. The inverse magnetoelastic contribution to anisotropy can be approximated as a field of the form¹³ $H_{KU}^\sigma \sim -3\lambda_i e_i E/M$, where e_i is the strain along a specified direction. A tetragonal distortion of $\text{Ga}_{0.948}\text{Mn}_{0.052}\text{As}$ grown on GaAs would lead us to expect an in-plane biaxial anisotropy along the [110] and equivalent axes. However, asymmetric strain from surface reconstruction³⁸, as well as

from device bending would tend to favor uniaxial anisotropy. Using the above estimate, with the experimental value for λ_{110} given by¹³ $\lambda_{100}/4+3\lambda_{111}/4=3.2$ ppm, and $M_s \approx 0.05$ T, we find that a strain of $-0.3\pm 0.1\%$ along [110] reproduces the measured value of H_{KU} at 4.2 K. This closely coincides with the -0.3% strain reported for $\text{Ga}_{0.948}\text{Mn}_{0.052}\text{As}$ grown on top of GaAs¹, suggesting that inverse magnetoelastic coupling is indeed responsible for a large part of the uniaxial magnetic anisotropy measured in this system. This observation also agrees with theoretical calculations carried out by Abolfath *et al.*³⁰ predicting that a strain of just 1% will overwhelm the unstrained cubic magnetocrystalline anisotropy.

7.8 Outlook on the role of magnetostriction in GaMnAs

The main results of this chapter were published in an October 2005 issue of *Physical Review Letters*³⁹. Strain engineering may ultimately play an important role in dilute magnetic semiconductor devices. Though it is possible to tune magnetic and electronic properties by electrically depleting carriers with a gate or illumination, the prodigious carrier densities in these materials suggests that this approach may not be able to provide much control. Moreover, current trends indicate that even higher doping levels are required to achieve room temperature operation, so the ability to deplete carriers will be additionally hampered. A lot of effort is now being directed toward current induced magnetization reversal⁴⁰, and using this effect to make a solid state magnetic random access memory (MRAM) device. Magnetostriction offers an alternative way of altering magnetic anisotropy energy, and piezoelectricity provides an excellent means of delivering the required stress, quickly, locally and with low power consumption. Future spintronics applications may benefit from the additional functionality provided by hybrid magnetoelastic/piezoelectric dilute magnetic semiconductors.

References

1. H. Ohno, A. Shen, F. Matsukura, A. Oiwa, A. Endo, S. Katsumoto, Y. Iye, (Ga,Mn)As: a new diluted magnetic semiconductor based on GaAs, *Appl. Phys. Lett.* **69**, 363 (1996)
2. H. Ohno, Making nonmagnetic semiconductors ferromagnetic, *Science* **281**, 951 (1998)
3. S. Koshihara *et al.*, Ferromagnetic order induced by photogenerated carriers in magnetic III-V semiconductor heterostructures of InMnAs / GaSb, *Phys. Rev. Lett.* **78**, 4617 (1997)
4. H. Ohno *et al.*, Electric-field control of ferromagnetism, *Nature* **408**, 944 (2000)
5. S. A. Wolf *et al.*, Spintronics: a spin-based electronics vision for the future, *Science* **294**, 1488 (2001)
6. D. D. Awschalom, D. Loss, N. Samarth, *Semiconductor Spintronics and Quantum Computation* (Springer, 2002)
7. T. Dietl, H. Ohno, F. Matsukura, J. Cibert, D. Ferrand, Ferromagnetism in zinc-blende magnetic semiconductors, *Science* **287**, 1019 (2000)
8. S. J. Pearton *et al.*, Wide band gap ferromagnetic semiconductors and oxides, *J. Appl. Phys.* **93**, 1 (2003)
9. O. Ozatay, P. Chalsani, N. C. Emley, I. N. Krivorotov, R. A. Buhrman, Magnetoresistance and magnetostriction effects in ballistic ferromagnetic nanoconstrictions, *J. Appl. Phys.* **95**, 7315 (2004)
10. C. Ruester *et al.*, Very large magnetoresistance in lateral ferromagnetic (Ga,Mn)As wires with nanoconstrictions, *Phys. Rev. Lett.* **91**, 216602 (2003)
11. J. A. Schuler, E. Johnston-Halperin, C. S. Gallinat, H. Knotz, A. C. Gossard, D. D. Awschalom, Structural engineering of ferromagnetism in III-V digital ferromagnetic heterostructures, *J. Appl. Phys.* **95**, 4922 (2004)
12. H. X. Tang, X. M. H. Huang, M. L. Roukes, M. Bichler, W. Wegscheider, Two-dimensional electron-gas actuation and transduction for GaAs nanoelectromechanical systems, *Appl. Phys. Lett.* **81**, 3879 (2002)
13. S. Chikazumi, *Physics of Magnetism* (Wiley, 1964)
14. T. Wojtowicz *et al.*, Enhancement of Curie temperature in GaMnAs/AlGaAs ferromagnetic heterostructures by Be modulation doping, *Appl. Phys. Lett.* **83**, 4220 (2003)
15. S. J. Potashnik *et al.*, Saturated ferromagnetism and magnetization deficit in optimally annealed GaMnAs epilayers, *Phys. Rev. B.* **66**, 012408 (2002)

16. I. Bargatin, E. B. Myers, J. Arlett, B. Guglewski, M. L. Roukes, Sensitive detection of nanomechanical motion using piezoresistive signal downmixing, *Appl. Phys. Lett.* **86**, 133109 (2005)
17. H. A. Tilmans, M. Elwenspoek, & J. H. J. Fluitman, Micro resonant force gauges, *Sens. Actuat. A* **30**, 35 (1992)
18. A. Dehé, K. Fricke, K. Mutamba, H. L. Hartnagel, A piezoresistive GaAs pressure sensor with GaAs/AlGaAs membrane technology, *J. Micromech. Microeng.* **5**, 139 (1995)
19. J. G. E. Harris *et al.*, Integrated micromechanical cantilever magnetometry of GaMnAs, *Appl. Phys. Lett.* **75**, 1140 (1999)
20. E. C. Stoner and E. P. Wohlfarth, A mechanism of magnetic hysteresis in heterogeneous alloys, *Philos. Trans. R. Soc. London A* **240**, 74 (1948)
21. E. B. Myers, private communication, & presentation at 2005 APS March meeting “Magnetomechanical dissipation in (Ga,Mn)As nanoelectromechanical resonators.”
22. A. Oiwa *et al.*, Nonmetal-metal-nonmetal transition and large negative magnetoresistance in (Ga,Mn)As/GaAs, *Solid State Comm.* **103**, 209 (1997)
23. V. F. Sapega, M. Moreno, M. Ramsteiner, L. Daeweritz, K. H. Ploog, Polarization of valence band holes in the (Ga,Mn)As diluted magnetic semiconductor, *Phys. Rev. Lett.* **94**, 137401 (2005)
24. R. Becker and W. Döring, *Ferromagnetismus* (Springer Verlag, Berlin 1939), p. 136
25. R. I. Cottam & G. A. Saunders, The elastic constants of GaAs from 2 K to 320 K. *J. Phys. C: Solid State Phys.* **6**, 2105 (1973)
26. H. X. Tang, R. K. Kawakami, D. D. Awschalom, M. L. Roukes, Giant planar hall effect in epitaxial (Ga,Mn)As devices, *Phys. Rev. Lett.* **90**, 107201 (2003)
27. U. Welp, V. K. Vlasko-Vlasov, X. Liu, J. K. Furdyna, T. Wojtowicz, Magnetic domain structure and magnetic anisotropy in GaMnAs, *Phys. Rev. Lett.* **90**, 167206 (2003)
28. X. Liu, Y. Sasaki, J. K. Furdyna, Ferromagnetic resonance in GaMnAs: effects of magnetic anisotropy, *Phys. Rev. B* **67**, 205204 (2003)
29. R. C. O’Handley, *Modern Magnetic Materials* (John Wiley, 2000)
30. M. Abolfath, T. Jungwirth, J. Brum, A. H. MacDonald, Theory of magnetic anisotropy in III-Mn-V ferromagnets, *Phys. Rev. B* **63**, 054418 (2001)
31. T. Dietl, H. Ohno, F. Matsukura, Hole-mediated ferromagnetism in tetrahedrally coordinated semiconductors, *Phys. Rev. B* **63**, 195205 (2001)

32. M. Sawicki *et al.*, Temperature peculiarities of magnetic anisotropy in (Ga,Mn)As: the role of hole concentration, *J. Supercond.* **16**, 7 (2003)
33. M. Sawicki *et al.*, In-plane uniaxial anisotropy rotations in (Ga,Mn)As thin films, *Phys. Rev. B* **71**, 121302 (2005)
34. P. W. Sparks & C. A. Swenson, Thermal expansions from 2 to 40 K of Ge, Si and four III-V compounds, *Phys. Rev.* **163**, 779 (1967)
35. M. Cardona & N. E. Christensen, Acoustic deformation potentials and heterostructure band offsets in semiconductors, *Phys. Rev. B* **35**, 6182 (1987)
36. S. Adachi, GaAs, AlAs, and Al_xGa_{1-x}As: material parameters for use in research and device applications, *J. Appl. Phys.* **58**, 1 (1985)
37. R. G. Stearns and G. S. Kino, Effect of electronic strain on photoacoustic generation in silicon, *Appl. Phys. Lett.* **47**, 1048 (1985)
38. Y. B. Xu, D. J. Freeland, M. Tselepi, J. A. C. Bland, Anisotropic lattice relaxation and uniaxial magnetic anisotropy in Fe/InAs(100) 4x2, *Phys Rev. B.* **62**, 1167 (2000)
39. S. C. Masmanidis, H. X. Tang, E. B. Myers, Mo Li, M. L. Roukes, G. Vermeulen, K. De Greve, W. Van Roy, Nanomechanical measurement of magnetostriction and magnetic anisotropy in (Ga,Mn)As, *Phys. Rev. Lett.*, **95** 187206 (2005)
40. M. Yamanouchi *et al.*, Current-induced domain-wall switching in a ferromagnetic semiconductor structure, *Nature* **428**, 539 (2004)

Chapter 8

The Big Picture

8.1 Summary and experimental conclusions

Based on the huge number of macroscopic devices that demand *piezoelectric* transduction – timers, sonar, film deposition monitors – it is not surprising that this effect holds promise for nanoscale mechanical devices. This mode of transduction has been largely neglected in NEMS because quartz and ferroelectric ceramics are not easily amenable to nanofabrication, and because silicon is not piezoelectric. We therefore relied on epitaxially grown GaAs/AlGaAs heterostructures. Given the semiconducting nature of these crystals, we have begun to explore ways of exploiting *bandstructure engineering* in the design of piezoelectric actuators. Experiments have demonstrated that these depletion-based nanoelectromechanical systems, or *D-NEMS* exhibit a predictable, *voltage-tunable electromechanical coupling* that can be tailored with doping profile. Energy band bending blurs the distinction between the layers serving as electrodes, and the layer serving as the piezoelectric insulator. The electromechanical coupling mediating this behavior operates on the same basic principle as a varactor diode – the application of a voltage induces band bending, which depletes charge carriers to a variable extent depending on doping. Whereas the primary result in varactors is tunable capacitance, in D-NEMS it alters the distribution of piezoelectrically induced strain and results in tunable mechanical actuation efficiency. The bandstructure dependence of the emergent electromechanical coupling was plainly shown by actuating radio frequency D-NEMS resonators fabricated from three suspended GaAs *pin* diodes with different doping profiles. The electromechanical actuation efficiency could

be tuned up, down or almost not at all by reverse biasing the diodes, in very good agreement with their predicted behavior.

D-NEMS not only exhibit a new form of electromechanical coupling, but they are highly *efficient* actuators. The piezoelectric strain generated by a single electronic charge modulated at the correct frequency on our devices is sufficient to resonantly drive them above their thermomechanical noise limit. Moreover, since piezoelectric strain relies on electric fields rather than current, this mode of actuation can be *nondissipative*. Of course, the finite resistivity of the semiconductor produces some dissipation, but this can be minimized by carefully designing the bandstructure. GaAs *pin* diodes and even highly doped *npn* junctions exhibited good electrical isolation, whereas *nin* junctions performed poorly in this respect*. On the other hand reduced isolation does not preclude piezoelectric actuation. For instance it was shown that diode-based D-NEMS could be actuated – albeit at reduced efficiency – in the forward biased regime.

D-NEMS have an additional level of functionality. In doubly clamped beams the resonance frequency can be tuned linearly with voltage by compressive or tensile piezoelectric stress. In contrast to electrostatic devices, the actuation and *frequency tuning* elements are completely integrated with the resonant nanomechanical structure, precluding the need for gate electrodes and therefore offering a much smaller device footprint. A further modality is based on the crystalline anisotropy of the piezoelectric constant; it can be tuned positive or negative or zero by properly orienting the device. The implications of this property have begun to be explored with cross-shaped and pairs of orthogonal resonators.

* The “intrinsic” GaAs layers are only 50 nm thick and have a background impurity doping of 10^{15} cm^{-3} , so they cannot be considered insulating.

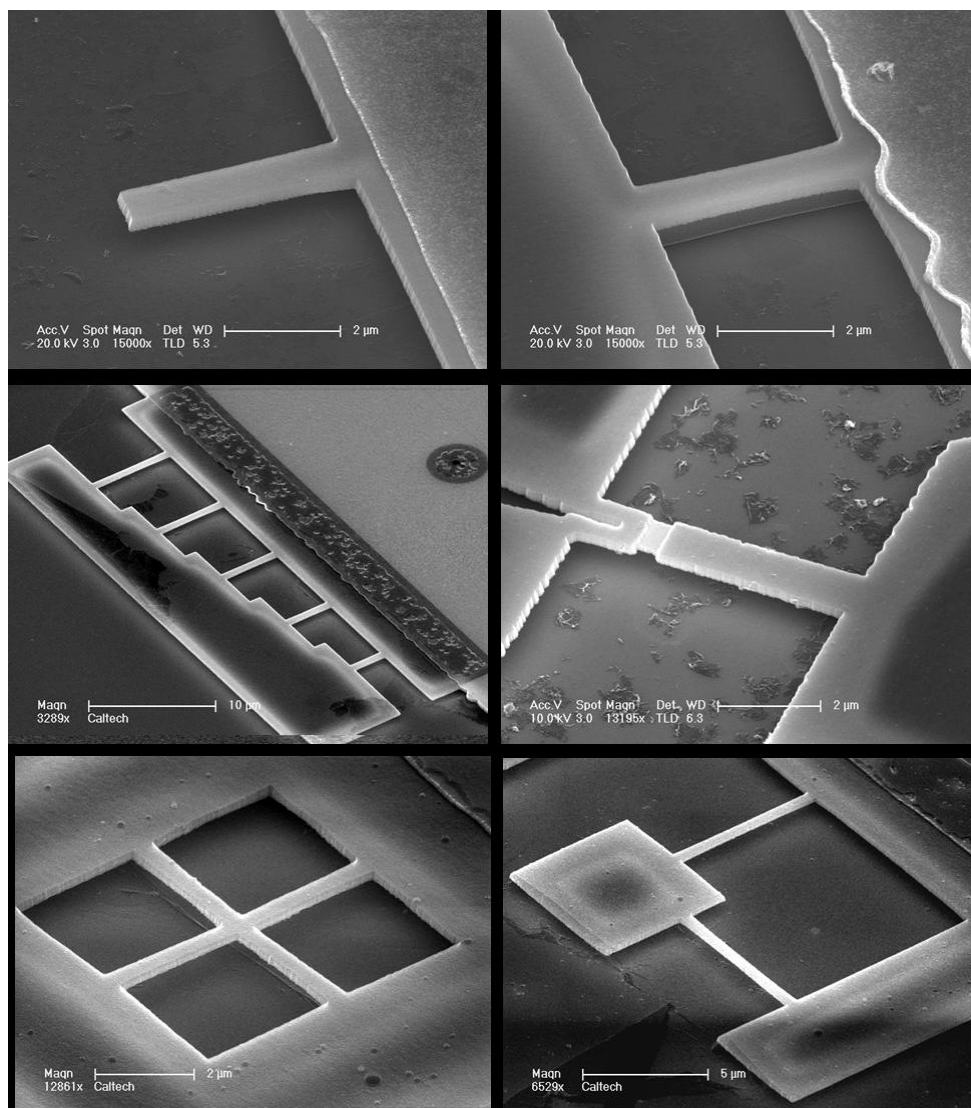


Figure 8.1 Some of the suspended nanomechanical GaAs structures used in the depletion-mediated NEMS (D-NEMS) experiments. Scale bars are (from top left going clockwise): 2, 2, 2, 2, 5, 2, 10 μm respectively.

In another project, the *dilute magnetic semiconductor* GaMnAs was employed. It has the interesting properties that its ferromagnetic interactions are mediated by holes, and it exhibits both piezoelectric and magnetoelastic effects, *i.e.*, its strain can be modulated by an electric and magnetic field. This combined electro- and magnetomechanical coupling has provided a foothold for actuating and manipulating a GaMnAs NEMS resonator; piezoelectricity and piezoresistivity were used for transduction, while magnetostriction was used to tune the resonance frequency. By

mapping out the evolution of frequency in a rotating magnetic field and comparing it to a model of magnetic free energy and magnetoelastic stress, the *magnetostriction constants* of a dilute magnetic semiconductor were obtained for the first time. The similarity between the temperature dependence of those values and the *magnetic anisotropy* fields, which were obtained concomitantly, underscore a complex interplay between strain, carrier density and ferromagnetism. Further theoretical and experimental work lies ahead to elucidate this unique coupling.

Since the frequency sensitivity to stress increases in inverse proportion to thickness, we anticipate that nanotube and nanowire NEMS will exhibit extraordinarily high resonance frequency tunability, while MEMS will not. Thus one of the main heuristic lessons is that any source of strain, no matter how small, can couple into nanomechanical structures in a discernable way. Ultimately this is a double-edged sword, for as their sensitivity increases, so does their susceptibility to unwanted fluctuations.

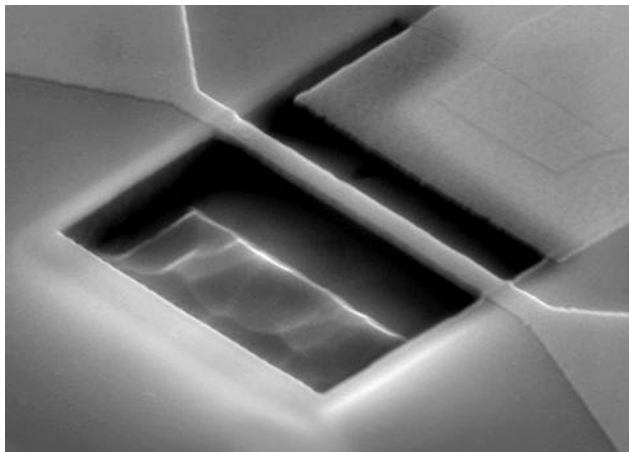


Figure 8.2 SEM image of the GaMnAs suspended beam used to obtain the first measurements of magnetostriction in a dilute magnetic semiconductor.

8.2 Outlook and challenges

An efficient integrated actuation scheme is but half the battle for NEMS. In spite of being excellent actuators with built-in frequency tunability, our devices currently lack the same efficacy in *detection*. I therefore anticipate that, if they are to move forward, D-NEMS must become fully monolithic transducers. Optical interferometry, while reliable, is difficult to implement on a chip-scale device. Piezoresistive measurements have already been demonstrated and represent one of the favorite detection techniques. On the other hand they require additional electrical contacts that are dissipative. The ideal situation would be to use piezoelectric read-out, but this has proven a challenge owing to the small device area and large parasitic capacitances involved. Nonetheless our preliminary measurements (Ch. 6) suggest that piezoelectric transduction can be a highly efficient process, and deserves further investigation. One of the main sources of capacitance is the large area of the electrodes used in making wirebond contacts; if the interconnects could be reduced to the dimensions of our devices we would expect over a thousandfold improvement in signal. On-chip amplifiers would also help minimize cable capacitance, and fortunately D-NEMS are highly amenable to such integration.

I close with some salient questions about where this work might be heading. Can bandstructure engineering be used to create useful nanomechanical devices? What is the practical application of piezoelectric resonance frequency tuning and its offshoot, parametric amplification? Will gallium arsenide occupy a prominent place in these systems or will it be replaced with alternative piezoelectric semiconductors? Should practical applications contain stand-alone devices or networks of arrays? What are the prospects for wireless NEMS technology? These issues have largely been overlooked in this work but some will become increasingly relevant to research if these systems are to be commercialized.

Bandstructure engineering is used in electronics—could it also add value to electromechanical devices? On the most basic and practical level, one could directly integrate

electronic components with the mechanical actuators. In this way one could improve signal detection, and create oscillators, tunable lasers and other hybrid systems. Indeed, these kinds of ideas are already being pursued on a number of fronts¹⁻⁷, using schemes that do not always involve piezoelectricity. In the longer term one could conceivably use the voltage-dependent electromechanical coupling efficiency, discussed in Chapter 2, to create arrays⁸ of individually actuated resonators, each one honed to pick up a distinct resonance frequency or biochemical substance. This could enable tunable bandpass filters or massively parallel NEMS-based biomedical diagnostic tools. A modified design could produce nonvolatile frequency tunable devices – a high bandwidth mechanical analog of charge coupled device (CCD) memory. NEMS-based computing⁹ may be possible with a similar approach. Piezoelectric and magnetoelastic resonance frequency tuning could also be applied to charge or magnetic field sensing, respectively.

Parametric amplification holds promise in improving the selectivity of bandpass filters. This would have obvious benefits for telecommunications, but we acknowledge that a wide gap exists between what our current devices can demonstrate and what industry demands. The D-NEMS *paramps* discussed in Chapter 5 work up about 50 MHz; with some effort it should be possible to extend the operational frequency to 100 MHz. But this is still an order of magnitude below the frequency range that is useful. It will take more than a little clever engineering to realize a transition to the gigahertz domain. Nevertheless, I remain cautiously optimistic that NEMS *paramps* could be made to reliably work in that regime. Parametric amplifiers are also touted as a means of boosting the performance of NEMS-based mass detectors, particularly in ambient environments where damping would otherwise inundate the signal. This is the subject of ongoing investigation.

Finding better materials remains a crucial challenge to the advancement of NEMS technology. Gallium arsenide, though amenable to epitaxial growth and nanofabrication, is not widely used on the grounds of low stiffness, high density, cost and bio-incompatibility. In spite of such

difficulties, GaAs has proven an excellent test platform for demonstrating the efficacies of D-NEMS architectures. Eventually a transition to piezoelectric SiC/AlN heterostructures or some variation thereof may be possible. Until then GaAs seems like the logical choice for pursuing D-NEMS research. Piezoelectric nanowires¹⁰ made of ZnO or AlN also seem like promising materials systems for NEMS. There is also an abundance of magnetoelastic materials to choose from, including the exotic giant magnetostrictive (GMS)¹¹ and ferromagnetic shape memory (FSM) alloys¹².

With the exception of a few experiments, most nanomechanical devices are comprised of a single resonant element such as a cantilever or bridge. A whole new class of devices can be created with arrays, which offer some significant advantages over stand-alone systems; namely, greater transduction signal and built-in fault tolerance. If properly synchronized¹³, arrays could improve the concentration sensitivity of a mass detector by boosting its signal. Intrinsic noise would also increase, but since this is rarely the limiting factor in performance it should not preclude a substantial improvement in sensitivity. Furthermore, if a few resonators in a large array failed, the device's overall performance would only slightly deteriorate but it could continue working. The implementation of array architectures hinges on two broad challenges: controlling the coupling between resonators and transducing them. The most readily available means of coupling resonators is fabricating them in close proximity to each other, and exploiting the flexible interconnections at their ends¹⁴. Other approaches include using magnetic or electrostatic¹⁵ interactions. Transduction will be a challenge if some means for individually addressing each resonator is required, but should be possible using on-chip multiplexing circuits. A simpler approach is to actuate and detect all devices in parallel, relying on the increased signal for improved measurement sensitivity. Piezoelectricity is particularly amenable to this approach because parallel signals are additive and devices require no side gates. Our nanomechanical array experiments being carried out at the time of writing are yielding promising results, but we are still hacking out an understanding and so do not include them in this thesis.

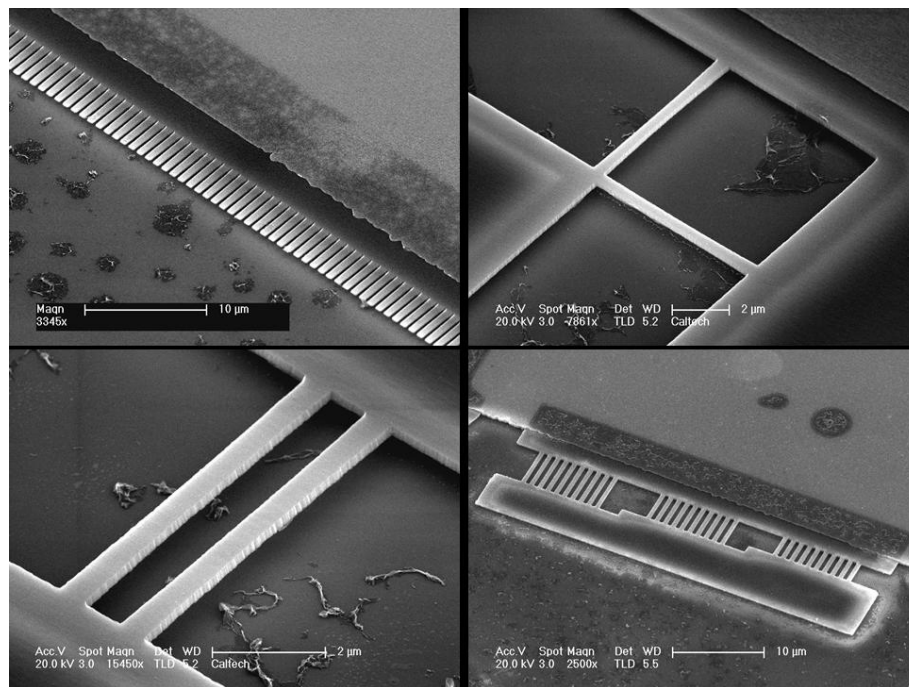


Figure 8.3 Nanomechanical arrays fabricated from piezoelectric D-NEMS material. Top left: section of 256 element cantilever array. Top right: orthogonal beams with one common clamping support. Bottom right: harp-like arrangement. Bottom left: doubly clamped beams with two common clamping supports. Scale bars are 10, 2, 10, 2 μm , respectively. Such device architectures could form the basis for future research on array synchronization.

What about wireless probes? Perhaps it makes sense to release NEMS from their substrate altogether. The small size of these devices would make remote read-out a daunting challenge, but by the same virtue they should be quite easy to excite. Therefore the idea might work with the proper instrumentation. One could choose from a host of techniques for transduction, but the most promising appear to be the familiar magnetostrictive¹⁶ and piezoelectric effects because they exhibit direct and inverse coupling, making them excellent candidates for both actuation and detection. Centimeter-scale magnetostrictive strips are widely used as theft prevention tags in retail stores; these devices are completely passive and reveal their presence by absorbing a tiny amount of electromagnetic radiation that is tuned to their mechanical resonance frequency. It

may only be a matter of time before chemical or biological¹⁷ sensors are developed that rely on this concept. The antitheft technology could serve as a beachhead onto such efforts, with nanotechnology providing new materials like magnetic or piezoelectric nanowires for making the resonators and possibly encapsulating them to allow operation in fluidic environments.

The mantra goes that nanotechnology is not only smaller, but different. Heeding that statement, NEMS may have the greatest clout in areas where they do not try to outperform other sensor systems based merely on size, but where they present entirely new, nano-enabled ways of using electromechanical transducers. Perhaps some of the ideas reported here represent such an opportunity.

References

1. H. Ukita, Y. Uenishi, & H. Tanaka, A photomicrodynamic system with a mechanical resonator monolithically integrated with laser diodes on gallium arsenide, *Science* **260**, 786-789 (1993)
2. R. G. Beck, M. A. Eriksson, R. M. Westervelt, K. L. Campman, A. C. Gossard, Strain-sensing cryogenic field-effect transistor for integrated strain detection in GaAs/AlGaAs microelectromechanical systems, *Appl. Phys. Lett.* **68**, 3763-3765 (1996)
3. R. H. Blick, M. L. Roukes, W. Wegscheider, M. Bichler, Freely suspended two-dimensional electron gases, *Physica B* **249-251**, 784 (1998)
4. P. Kumar, L. Li, L. Calhoun, P. Boudreaux, D. Devoe, Fabrication of piezoelectric Al_{0.3}Ga_{0.7}As microstructures, *Sens. Actuat. A* **115**, 96-103 (2004)
5. Q. Chen *et al.*, First demonstration of a MEMS tunable vertical-cavity SOA, *IEEE Phot. Tech. Lett.* **16**, 1438 (2004)
6. G. Piazza, K. Castelino, A. P. Pisano, C. J. Chang-Hasnain, Design of a monolithic piezoelectrically actuated microelectromechanical tunable vertical-cavity surface-emitting laser, *Optics Letters* **30**, 896-898 (2005)
7. G. Shekhawat, S. H. Tark, V. P. Dravid, MOSFET-embedded microcantilevers for measuring deflection in biomolecular sensors, *Science* **311**, 5192 (2006)
8. P. Vettiger *et al.*, The millipede—more than one thousand tips for future AFM storage, *IBM J. Res. Develop.* **44**, 323 (2000)
9. M. L. Roukes, Mechanical computation, redux? *Electron Devices Meeting, 2004. IEDM Technical digest 13-15 Dec. 2004.* pgs. 539-542.
10. Z. L. Wang & J. Song, Piezoelectric nanogenerators based on zinc oxide nanowire arrays, *Science* **312**, 242 (2006)
11. A. Ludwig & E. Quandt, Giant magnetostrictive thin films for applications in microelectromechanical systems, *J. Appl. Phys.* **87**, 4691 (2000)
12. J. W. Dong *et al.*, Shape memory and ferromagnetic shape memory effects in single-crystal Ni₂MnGa thin films, *J. Appl. Phys.* **95**, 2593 (2004)
13. M. C. Cross, A. Zumdieck, R. Lifshitz & J. L. Rogers, Synchronization by nonlinear frequency pulling, *Phys. Rev. Lett.* **93**, 224101 (2004)
14. M. K. Zalalutdinov *et al.*, Two-dimensional array of coupled micromechanical resonators, *Appl. Phys. Lett.* **88**, 143504 (2006)
15. E. Buks & M. L. Roukes, Electrically tunable collective response in a coupled micromechanical array, *J. MEMS* **11**, 802 (2002)

16. C. A. Grimes *et al.*, Wireless magnetoelastic resonance sensors: a critical review, *Sensors* **2**, 249 (2002)
17. J. C. Ball, L. G. Puckett, & L. G. Bachas, Toward a magnetoelastic biosensor, *Anal. Chem.* **75**, 6932 (2003)

Appendix

List of major measurement equipment

Hewlett Packard 3577A network analyzer

Hewlett Packard 5334A universal counter

Agilent 33250A function generator

EG&G (now Signal Recovery) 5210 lockin amplifier

Signal Recovery 5185 wideband high input impedance preamplifier

Keithley 236 DC power source

New Focus Instruments 1801 low noise photodetector

Newport 505 laser diode driver

Thor Labs L904P010 IR laser diode; 904 nm, 10 mW CW (max)